NASA CR-50,171

183p.

FINAL REPORT ON A STUDY OF METEOROID IMPACT PHENOMENA

Prepared for:

NATIONAL AERONAUTICS AND SPACE
ADMINISTRATION

FINAL REPORT

W. J. Rae and H. P. Kirchner

Contract No. NAS 3-2121

CAL Report No. RM-1655-M-4

February 1963

CORNELL AERONAUTICAL LABORATORY, INC.

OF CORNELL UNIVERSITY, BUFFALO 21, N. Y.

RQT
2145

code-1

CORNELL AERONAUTICAL LABORATORY, INC.
BUFFALO 21, NEW YORK

REPORT NO. RM-1655-M-4

FINAL REPORT ON A STUDY OF METEOROID IMPACT PHENOMENA

FEBRUARY 1963

CONTRACT NO. NAS 3-2121

PREPARED FOR
NATIONAL AERONAUTICS AND SPACE ADMINISTRATION

PREPARED BY: William J. Rae
William J. Rae

Henry P. Kirchner
Henry P. Kirchner

APPROVED BY: A. Hertz
A. Hertzberg, Head,
Aerodynamic Research Dept.

FOREWORD

This report presents the results of a theoretical study of hypervelocity impact into semi-infinite targets. The work has been sponsored by the Lewis Research Center of the National Aeronautics and Space Administration under Contract No. NAS 3-2121, in support of their Research Program to develop a structurally adequate radiator for use on space vehicles. In order to provide the desired support, diverse aspects of the meteoroid impact problem have been examined. This report collects all pertinent data obtained under the contract into one reference work which will be useful, as such, for NASA's program and also for background for further research on hypervelocity impact phenomena.

Technical monitoring was provided by Mr. Robert J. Denington and Mr. James J. Kramer, to whom the authors are very grateful for numerous helpful suggestions.

The approach on which this study is based was suggested originally by Dr. Franklin K. Moore of this Laboratory, and was later elaborated by Dr. Walter E. Gibson. The authors have continued to benefit from frequent discussions with Drs. Moore and Gibson, and in addition, valuable contributions have been made by Mr. Howard A. Scheetz and Dr. Norman S. Eiss.

Special thanks are due to Mr. Harold M. Rosenbaum, who very ably handled the programming of various calculations for an IBM 704, and to Miss Marcia J. Williams, Miss Sarah J. Geraci, Mr. Girard A. Simons, and Mr. John R. Moselle, who prepared the figures and carried out the associated calculations.

The analyses presented below embrace both fluid-mechanical and solid-mechanical considerations. The former are the work of the first author, while the latter are due to the second.

16837

ABSTRACT

This report presents an analytical treatment of the process of crater formation in semi-infinite targets as a result of impact by hypervelocity projectiles. The results are achieved by using blast-wave theory to treat the fluid-mechanical phase of the target response, together with a simple means of accounting for the target strength in the later stages of the cratering process. The crater-size formula finally deduced is quite simple. To enable the interested reader to apply it without following a lengthy derivation, the formula and its application are presented in a separate section.

The theory in its present form is found to agree reasonably well with relatively low-speed experiments, and the agreement can be expected to improve at higher impact speeds. The simple crater-size formula reveals that the kinetic energy of the impacting particle is a controlling parameter and that the dynamic strength of the target is the factor most effective in limiting penetration.

Careful attention is paid to energy and momentum conservation, and the momentum of the incident particle is found to play a relatively minor role. The attendant physical and mathematical reasons are discussed, including their implications on experiment.

Requests for copies of this report should be referred to:

National Aeronautics and Space Administration
Office of Scientific and Technical Information
Washington 25, D. C.
Attn: AFSS-A

TABLE OF CONTENTS

LIST OF FIGURES

LIST OF TABLES

LIST OF SYMBOLS

a, K	parameters in assumed pressure distribution
c	limiting speed of a weak shock
d	projectile diameter
e	internal energy per unit mass
E	total energy
$\mathcal{E}$	total energy per unit area
f	dimensionless pressure
g	dimensionless internal energy
G	shear modulus
$H(\eta)$	function defined by Eq. (96)
$I_1(\gamma)$	function defined by Eq. (66)
m_0	neglected mass per unit area
N	exponent describing shock speed $R_s \sim t^N$
p	pressure
P	total momentum
$\mathcal{P}$	total momentum per unit area
$\mathbb{P}$	pressure level at which solution is terminated
$\vec{q}$	velocity vector
r, θ	spherical coordinates
R_s	shock radius
s	entropy; also dimensionless parameter in $u_s = c + s u_1$
t	time after impact
T	temperature
u, w	velocity components in r and θ directions

V	impact speed
Y	Young's modulus
$\Delta(\rho)$	function appearing in Mie-Grüneisen state equation
η	similarity coordinate, r/R_s
ϕ	dimensionless r -component of velocity
$\Gamma(\rho)$	Grüneisen factor
γ	constant used to approximate $1+\Gamma(\rho)$
ν	Poisson's ratio
ψ	dimensionless density
ρ	mass density
σ	shear stress
$\Upsilon(\eta)$	centerline value of tangential velocity gradient, $2\frac{\partial\omega}{\partial\theta}(\eta,0)$
ω	dimensionless tangential velocity component
$(\ )_0$	undisturbed value, before impact
$(\ )_1$	value behind the shock
$(\ )_s$	value at the shock
$(\ )_c$	cohesive part
$(\ )_H$	evaluated on the Hugoniot
$(\ )_p$	pertains to the projectile
$(\ )^*$	indicates sonic-point value

INTRODUCTION

The purpose of this research has been to achieve an analytical description of the phenomena brought into play when a high-speed projectile strikes a semi-infinite target. The extremely high pressures generated under the conditions of high-speed impact suggest a fluid-mechanical model for describing the motion of the impacted medium. Numerical solutions of the resulting equations have been published for specific cases. This report describes analytic results obtained by applying blast-wave theory to solve these fluid-mechanical equations. The spirit of the approach is to simplify the analysis wherever possible by making certain approximations to the true physical situation. The aim in doing so is to achieve generality and simplicity of the results, at the expense of some exactness in describing the details of the solution.

The report is divided, essentially, into two parts. The first of these, Part I, describes the blast-wave solution for the early, high-pressure phase of the motion. The second, Part II, discusses the solid-mechanical aspects of the problem, particularly from the point of view of the target strength. Part III summarizes the theory, and illustrates the use of the crater-size formula by working out several examples. To facilitate quick application, this section is so written that it may be read independently of the remainder of the report.

In Part I, two types of solution are described. In one, which permits spatial variations in two directions, it is possible to conserve both the energy and momentum of the system. The other solution, which allows only for variations in the radial direction, and conserves only the total energy, is a modification of the classical Taylor solution for an instantaneous point release of energy. Approximate solutions of the former type are found to be very close to the vastly-simpler Taylor solution in all important respects. The analytical results that lead to this conclusion are described, and the physical reasons that underlie this phenomenon are discussed. The significance of this finding is to indicate why the simpler Taylor solution may be used.

Part II is devoted generally to a study of the limits of the blast-wave analysis, and describes some of the detailed phenomena that may be expected during the early stages of the impact process. In addition, particular attention is paid to the later stages of crater formation, during which the plastic and elastic response of the target must be considered. An important part of this work is to identify the material-strength level at which the blast-wave solution is to be terminated. The meaning of this as a crater-formation criterion is discussed.

The concluding remarks summarize the advances that have been made, and indicate the areas where improvements in the theory can be expected.

I. BLAST-WAVE SOLUTION

This portion of the report presents the solutions obtained for the target response in the fluid regime. Section A, below, describes the fluid-mechanical model, listing the several approximations that are fundamental to a blast-wave solution. The second and third sections then present two different types of solution of the fluid-dynamical equations.

A. Fluid-Mechanical Model

To derive an analytic description of hypervelocity impact, two steps are taken. The first is to treat the target material as a compressible fluid, while the second is to simplify the resulting equations in such a manner that a simple solution is possible. Similarly, below, the basic equations appropriate to the compressible-fluid approximation are first discussed. Then described are the key mathematical simplifications used, and the restrictions which they imply. The last two sub-sections summarize the formulation of the problem.

1. Basic Equations. When a particle strikes a target surface at high speed, large amounts of energy and momentum are quickly deposited over a very small portion of the surface. This release drives a strong shock wave into the target, generating extremely large pressures, typically measured in megabars. Because these pressures are so large compared with the material strength, even at high strain rates, one is led to the approximation that the impacted medium behaves like an inviscid, compressible fluid. In actual fact, the justification for such an approximation is not provided by the magnitude of the pressures themselves, but must come from a consideration of their gradients. Consider a small mass element

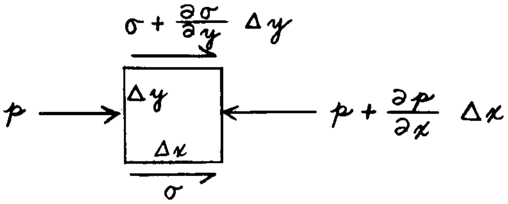

The net force acting in the x-direction is proportional to $\frac{\partial\sigma}{\partial y} - \frac{\partial p}{\partial x}$. Thus the neglect of resistance to shear deformation requires $\frac{\partial p}{\partial x}\Big/\frac{\partial\sigma}{\partial y} \gg 1$. To replace this by the simpler statement above is to assume that rates of change in the two perpendicular directions are of the same order, and that the proper orders of magnitude to use for p and σ are the impact pressure and material strength. There appears to be no reason for doubting either of these assumptions in the early stages of the impact process.

Thus the problem of determining the response of the target material becomes essentially that of solving the fluid-mechanical equations expressing the conservation of mass, momentum, and energy, together with the equation of state of the medium

Conservation of mass

$$\frac{D\rho}{Dt} + p \operatorname{div} \vec{q} = 0 \tag{1}$$

Conservation of momentum

$$\frac{D\vec{q}}{Dt} + \frac{1}{\rho} \operatorname{grad} p = 0 \tag{2}$$

Conservation of Energy

$$\frac{De}{Dt} + p\,\frac{D(1/\rho)}{Dt} = 0 \qquad \text{or} \qquad \frac{Ds}{Dt} = 0 \tag{3}$$

Equation of State

$$e = F(p, \rho) \tag{4}$$

Here ρ denotes the density, p the pressure, e the internal energy per unit mass, s the entropy, and $\vec{q}$ the velocity vector. The symbol D/Dt is the convective derivative

$$\frac{D}{Dt} = \frac{\partial}{\partial t} + \vec{q} \cdot \nabla \tag{5}$$

in which t is the time and ∇ the gradient operator. It should be noted that the assumption of an inviscid fluid has been made by setting the right-hand side of Eq. (2) equal to zero. If shearing forces were to affect the motion, they would have to be added to this equation. Consistent with this approximation, energy changes arising from viscous dissipation and heat conduction are omitted from the energy equation. In addition, energy changes due to radiation and chemical change are also neglected. Thus, the conservation of energy simply states that, for each element of mass, changes of internal energy, de, are balanced by changes in the flow-work term, $p\,d(1/\rho)$. Alternatively, this may be expressed by stating that the entropy of a given mass element does not change, after it has been processed by the shock.

Finally, it should be noted that the use of an equation of state implies an assumption of thermodynamic equilibrium.

2. Symmetry Assumptions. All of the analyses of this report assume that the impact occurs at normal incidence, and the ensuing motion is taken to be symmetric about an axis which is normal to the original target surface, and passes through the impact point. For such an axisymmetric flow, the scalar forms of the equations of motion, in spherical coordinates, are

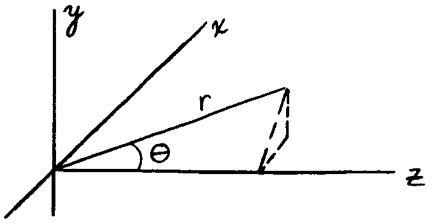

x, y plane is
target surface

Continuity

$$\frac{\partial \rho}{\partial t} + u\frac{\partial \rho}{\partial r} + \frac{w}{r}\frac{\partial \rho}{\partial \theta} + \rho\left(\frac{\partial u}{\partial r} + \frac{1}{r}\frac{\partial w}{\partial \theta} + \frac{2u}{r} + \frac{w}{r}\cot\theta\right) = 0 \tag{6}$$

Radial component of the momentum equation

$$\frac{\partial u}{\partial t} + u\frac{\partial u}{\partial r} + \frac{w}{r}\frac{\partial u}{\partial \theta} - \frac{w^2}{r} + \frac{1}{\rho}\frac{\partial p}{\partial r} = 0 \tag{7}$$

Angular component of the momentum equation

$$\frac{\partial w}{\partial t} + u\frac{\partial w}{\partial r} + \frac{w}{r}\frac{\partial w}{\partial \theta} + \frac{uw}{r} + \frac{1}{\rho r}\frac{\partial p}{\partial \theta} = 0 \tag{8}$$

Conservation of Energy

$$\frac{\partial e}{\partial t} + u\frac{\partial e}{\partial r} + \frac{w}{r}\frac{\partial e}{\partial \theta} - \frac{p}{\rho^2}\left(\frac{\partial \rho}{\partial t} + u\frac{\partial \rho}{\partial r} + \frac{w}{r}\frac{\partial \rho}{\partial \theta}\right) = 0 \tag{9}$$

Equation of State

$$e = F(p, \rho) \tag{10}$$

Here u and w denote the velocity components in the r- and θ-directions, respectively. Equations (6) - (10) are five relations for the quantities p, ρ, u, w, and e. One can also work with the entropy, rather than the internal energy, in which case the last two equations are replaced by

$$\frac{\partial s}{\partial t} + u\frac{\partial s}{\partial r} + \frac{w}{r}\frac{\partial s}{\partial \theta} = 0 \tag{11}$$

$$s = s(p, \rho) \tag{12}$$

3. Boundary Conditions. The boundary conditions that apply at the shock wave, i.e., at $r = R_s(\theta, t)$, state that the discontinuities in velocity, pressure, density, etc. across the wave are given by the Rankine-Hugoniot relations. For a shock advancing into a medium at rest, these are

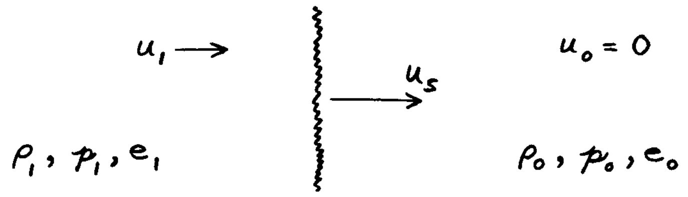

Conservation of mass

$$\rho_0 u_s = \rho_1 (u_s - u_1) \tag{13}$$

Conservation of momentum

$$p_0 + \rho_0 u_s^2 = p_1 + \rho_1 (u_s - u_1)^2 \tag{14}$$

or, using (13)

$$p_1 - p_0 = \rho_0 u_s u_1 \tag{14a}$$

Conservation of Energy

$$e_1 - e_0 = \frac{1}{2} (p_0 + p_1) \left(\frac{1}{\rho_0} - \frac{1}{\rho_1} \right) \tag{15}$$

These three equations, together with the equation of State, are sufficient to define the four quantities u_1, ρ_1, p_1, and e_1 as functions of u_s, for given initial values p_0, ρ_0, and e_0. This locus of states which may be reached across a normal shock wave is called the Hugoniot of the medium.

The analysis of this report assumes that the shock wave is always hemispherical in shape as it advances into the target. This assumption is based on observations of shock shape in Lucite, (1, 2) in metals, (1) and in wax, (3, 4) all under hypervelocity impact conditions. Further evidence for the assumption comes from fact that the craters formed are very nearly hemispherical in shape at high impact speed.

At this point, then, the fluid-mechanical problem that is posed is the solution of Eqs. (6) - (10), describing the motion of an inviscid, compressible fluid behind a hemispherical shock wave that advances into a semi-infinite target

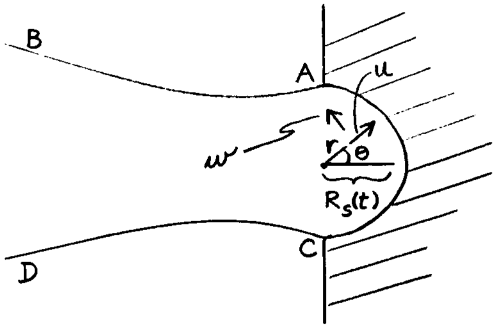

The motion must be such that the boundary conditions (13) - (15) are satisfied at the shock, while along the surfaces AB and CD (whose location is unknown) the pressure and material density must vanish.

The solution of such a boundary-value problem is an exceedingly formidable task; the coupled, nonlinear partial differential equations involve three independent variables. Approximate numerical solutions of these equations have been presented by Bjork,$^{(5)}$ for some specific cases. The objective of the present work is to achieve approximate analytic solutions which display, in a simple but realistic way, the influences of the various physical parameters.

4. Similarity Assumption. The most important approximation made, in order to achieve the goal of an analytic solution, is that the flow is self-similar; i. e. , the distributions of the various physical quantities (such as pressure, density, etc.) at each instant, are taken to be the same when viewed on a scale defined by the shock radius at that instant. Thus each quantity, instead of depending separately on the time and on the distance r from the impact point, is assumed to be a function of the combination $r / R_s(t)$. This reduction of the number of independent variables

constitutes a significant simplification in the differential equations that must be solved.

The mathematical expression of this assumption is to introduce the similarity variable

$$\eta = \frac{r}{R_s(t)} \tag{16}$$

and to redefine the velocity components, pressure, density, and internal energy by the dimensionless functions

$$\begin{aligned} u(r,\theta,t) &= \dot{R}_s\, \phi(\eta,\theta) & p(r,\theta,t) &= \rho_0 \dot{R}_s^2 f(\eta,\theta) \\ w(r,\theta,t) &= \dot{R}_s\, \omega(\eta,\theta) & \rho(r,\theta,t) &= \rho_0\, \psi(\eta,\theta) \\ & & e(r,\theta,t) &= \dot{R}_s^2\, g(\eta,\theta) \end{aligned} \tag{17}$$

When these relations are substituted into Eqs. (6) - (9), and derivatives with respect to r and t replaced in terms of derivatives with respect to η, one finds that all explicit time dependence disappears from the differential equations if one chooses

$$R_s = At^N$$

When this is done, the basic equations become

$$(\phi-\eta)\frac{\partial\psi}{\partial\eta} + \frac{\omega}{\eta}\frac{\partial\psi}{\partial\theta} + \psi\left(\frac{\partial\phi}{\partial\eta} + \frac{1}{\eta}\frac{\partial\omega}{\partial\theta} + 2\,\frac{\phi}{\eta} + \frac{\omega}{\eta}\cot\theta\right) = 0 \tag{18}$$

$$-\frac{1-N}{N}\phi + (\phi-\eta)\frac{\partial\phi}{\partial\eta} + \frac{\omega}{\eta}\frac{\partial\phi}{\partial\theta} - \frac{\omega^2}{\eta} + \frac{1}{\psi}\frac{\partial f}{\partial\eta} = 0 \tag{19}$$

$$-\frac{1-N}{N}\omega + (\phi-\eta)\frac{\partial\omega}{\partial\eta} + \frac{\omega}{\eta}\frac{\partial\omega}{\partial\theta} + \frac{\phi\,\omega}{\eta} + \frac{1}{\eta\psi}\frac{\partial f}{\partial\theta} = 0 \tag{20}$$

$$-2\,\frac{1-N}{N}g + (\phi-\eta)\frac{\partial g}{\partial\eta} + \frac{\omega}{\eta}\frac{\partial g}{\partial\theta} - \frac{f}{\psi^2}\left([\phi-\eta]\frac{\partial\psi}{\partial\eta} + \frac{\omega}{\eta}\frac{\partial\psi}{\partial\theta}\right) = 0 \tag{21}$$

The parameter N which appears here is, for the moment, unspecified.

Next, the boundary conditions must be examined, to see if they are compatible with the similarity assumption. At the shock $\left(\eta = 1, -\frac{\pi}{2} \leq \theta \leq +\frac{\pi}{2}\right)$ defining $e_o = 0$, Eqs. (13), (14a), (15), and (14) become

$$\psi(1,\theta)\left[1 - \phi(1,\theta)\right] = 1 \tag{22}$$

$$f(1,\theta) = \phi(1,\theta) + \frac{p_o}{\rho_o \dot{R}_s^2} \tag{23}$$

$$g(1,\theta) = \frac{1}{2}\left(\frac{p_o}{\rho_o \dot{R}_s^2} + f(1,\theta)\right)\left(1 - \frac{1}{\psi(1,\theta)}\right) \tag{24}$$

$$\dot{R}_s^2 \; g(1,\theta) = F\left[\rho_o \dot{R}_s^2 f(1,\theta), \rho_o \psi(1,\theta)\right] \tag{25}$$

The first three of these are independent of the time if the initial pressure in the undisturbed medium, p_o, is small compared with $\rho_o \dot{R}_s^2$, which is of the order of the pressure being generated at the shock. This condition will certainly be met whenever the fluid-mechanical model is appropriate. Thus the question of whether a similarity solution is compatible with the boundary conditions depends solely on whether the form of the internal energy function F is such as to permit the time dependence to be eliminated from Eq. (25). Sedov$^{(6)}$ has pointed out that this can be done wherever the internal energy is of the form

$$e = p\,\varphi(\rho) \tag{26}$$

where φ is any function of the density. For such a case, Eq. (25) becomes

$$g(1,\theta) = \rho_0 f(1,\theta)\, \varphi \left[\rho_0 \psi(1,\theta)\right] \tag{27}$$

and all explicit time dependence is eliminated. Thus, a self-similar solution is possible whenever the medium obeys the equation of State (26). In this case, the boundary values at the shock can be conveniently found by solving Eqs. (22) - (24) for $\phi(1,\theta)$, $f(1,\theta)$, and $g(1,\theta)$ in terms of $\psi(1,\theta)$

$$\phi(1,\theta) = f(1,\theta) = 1 - \frac{1}{\psi(1,\theta)} \tag{28}$$

$$g(1,\theta) = \frac{1}{2}\left(1 - \frac{1}{\psi(1,\theta)}\right)^2 \tag{29}$$

When these relations are substituted into Eq. (27), the result is a single expression for the density ratio at the shock

$$\frac{1}{2}\left(1 - \frac{1}{\psi(1,\theta)}\right) = \rho_0 \varphi \left[\rho_0 \psi(1,\theta)\right] \tag{30}$$

Having found $\psi(1,\theta)$ the other quantities at the shock are found from Eqs. (28) and (29).

5. Perfect-gas Approximation. The target materials of greatest interest in the present investigation are metals, for which the equation of State in the range of pressures appropriate here is the Mie-Grüneisen relation(7)

$$e(p,\rho) - e_c(\rho) = \frac{p - p_c(\rho)}{\rho\,\Gamma(\rho)} \tag{31}$$

where the subscript c denotes the cohesive contribution, and where Γ is the Grüneisen constant, which depends weakly on ρ. The cohesive contributions can be found from measured shock-wave data: along the Hugoniot, Eq. (31) takes the form

$$e_H(\rho) - e_c(\rho) = \frac{p_H(\rho) - p_c(\rho)}{\rho\Gamma(\rho)}$$

Subtracting this from Eq. (31) then gives

$$e - e_H(\rho) = \frac{p - p_H(\rho)}{\rho\Gamma(\rho)}$$

The Mie-Grüneisen equation can be rearranged as

$$e = \frac{p}{\rho\Gamma(\rho)} - \Delta(\rho) \tag{32}$$

where

$$\Delta(\rho) = \frac{p_c(\rho)}{\rho\Gamma(\rho)} - e_c(\rho) = \frac{p_H(\rho)}{\rho\Gamma(\rho)} - e_H(\rho) \tag{33}$$

All of the analyses of this report use only the leading term of Eq. (32), which can be accommodated in a self-similar solution. The present solution will therefore be valid only when the pressure is sufficiently high that $\Delta(\rho)$ can be neglected in comparison with the leading term. In actual fact, most impacts will span a time interval during which this approximation fails. It is important to realize that the pressures at which $\Delta(\rho)$ is too large to be neglected are nevertheless sufficiently high that the compressible-fluid approximation is well justified.

The analyses presented here have made the further approximation of neglecting the variation of the Grüneisen factor $\Gamma(\rho)$, replacing it by a constant, denoted by $\gamma - 1$. Under this approximation, the equation of State becomes that of a perfect gas of constant specific-heat ratio γ, namely

$$e = \frac{p}{(\gamma-1)\rho} \tag{34}$$

The use of this state equation amounts to a high-pressure approximation of the Mie-Grüneisen relation, with $\Gamma(\rho)$ taken as a constant, equal to $\gamma - 1$, and it makes available all the results of the extensive literature dealing with blast waves in a perfect gas. Because $\Gamma(\rho)$ is typically about 2.0 to 3.0, γ will be on the order of 3.0 or greater. It should be borne in mind, however, that the similarity solution is not limited to the predictions made with the perfect-gas model; the variation of Γ could be accounted for, but is neglected here as a matter of convenience.

When the perfect-gas approximation is made, the energy equation ((19) or (11)) becomes

$$\frac{\partial p}{\partial t} + u\frac{\partial p}{\partial r} + \frac{w}{r}\frac{\partial p}{\partial \theta} + \frac{\gamma p}{\rho}\left(\frac{\partial \rho}{\partial t} + u\frac{\partial \rho}{\partial r} + \frac{w}{r}\frac{\partial \rho}{\partial \theta}\right) = 0 \qquad (35)$$

In terms of the similar functions, this is

$$-2\,\frac{1-N}{N} f + (\phi - \eta)\left(\frac{\partial f}{\partial \eta} - \frac{\gamma f}{\psi}\frac{\partial \psi}{\partial \eta}\right) + \frac{\omega}{\eta}\left(\frac{\partial f}{\partial \theta} - \frac{\gamma f}{\psi}\frac{\partial \psi}{\partial \theta}\right) = 0 \qquad (36)$$

It is interesting to examine the accuracy of the perfect-gas model for a particular material. The equation of State enters the analysis by way of Eq. (11), which states that the entropy of a given particle does not change, after being processed by the shock. In general, the entropy of a medium is a function of any two thermodynamic variables, for example the pressure and density. In making the ideal-gas approximation, the entropy is assumed to depend on these only in the special combination

$$s = \mathrm{fcn}\,(p/\rho^{\gamma})$$

To assess the quantitative validity of this assumption, then, it is necessary to determine how accurately the isentropic states of a given material are approximated by the relation

$$\ln p - \gamma \ln \rho = \text{constant} \tag{37}$$

An explicit equation of state for iron, developed by a group at the Los Alamos Scientific Laboratory, has been published by Bjork.$^{(8)}$ This equation has been used to calculate the pressure as a function of internal energy at various densities. The resulting map of thermodynamic states is shown in Fig. 1. Also shown is the Hugoniot, i. e., the locus of states which can exist behind normal shock waves. This locus is the set of points which satisfy the condition

$$e = \frac{p}{2\rho_0}\left(1 - \frac{\rho_0}{\rho}\right) \tag{38}$$

where ρ_0 is the normal density of iron, 7.86 grams per cubic centimeter. The experimental Hugoniot curve, recently determined up to pressures of nine megabars by Altshuler et al$^{(9)}$ is included, and agrees quite well with the theoretical curve. In addition to this experimental check, the pressures shown on Fig. 1 at zero energy* agree quite well with the Mie-Grüneisen values

$$\left. p \right]_{e=0} = \rho\, \Gamma(\rho)\, \Delta(\rho) \tag{39}$$

given by Altshuler et al in an earlier publication.$^{(10)}$ Thus Fig. 1 may be considered a valid representation of the thermodynamic states of compressed iron.

Three isentropes have been added to this map, by a trapezoidal-rule integration of

$$de = -p\,dv\,, \quad \text{or} \quad \frac{de}{d(\rho/\rho_0)} = \frac{p/\rho_0}{(\rho/\rho_0)^2} \tag{40}$$

---

* It should be noted that Eq. (39) provides a simple way of calculating the relative contributions from the two terms in Eq. (32)

$$e = \frac{p}{\rho\Gamma(\rho)}\left[1 - \frac{\rho\Delta(\rho)\Gamma(\rho)}{p}\right] = \frac{p}{\rho\Gamma(\rho)}\left(1 - \frac{[p(\rho)]_{e=0}}{p(\rho,e)}\right)$$

which holds for constant entropy. The three isentropes shown may be thought of as describing the histories of three particles which lie along the axis of symmetry in a given impact, and which are therefore processed by successively weaker stages of the same shock wave. Particle 1, for example, is raised from its normal state to the point shown on the Hugoniot by a shock wave moving at 20.8 km/sec; its subsequent expansion to low density takes place along the isentrope shown. In similar fashion, particles 2 and 3 are processed by the shock when it is traveling at 16.5 and 8.62 km/sec, respectively. The p, ρ-coordinates of these three isentropes are re-plotted in Fig. 2. Large portions of these curves are accurately reproduced by a constant value of γ, i.e., they have a constant slope.

6. Procedure for finding γ. In applying a constant - γ theory to any given impact problem, only a single value of γ may be used. If, in the example cited above, one chooses the value appropriate to particle 1 at the shock, the approximation will begin to deteriorate for the lower-density states of this particle, and will be less accurate for all states of particles 2 and 3. In order to minimize the error, it would appear that γ should match the higher-density, higher-pressure portions of the flow. Partly for this reason, and partly for ease of application, the procedure recommended here is to choose γ so as to match conditions at the impact point. For any impact, one may imagine that there is a small region in the immediate vicinity of the impact point, where the collision is equivalent to the planar impact of two semi-infinite bodies.

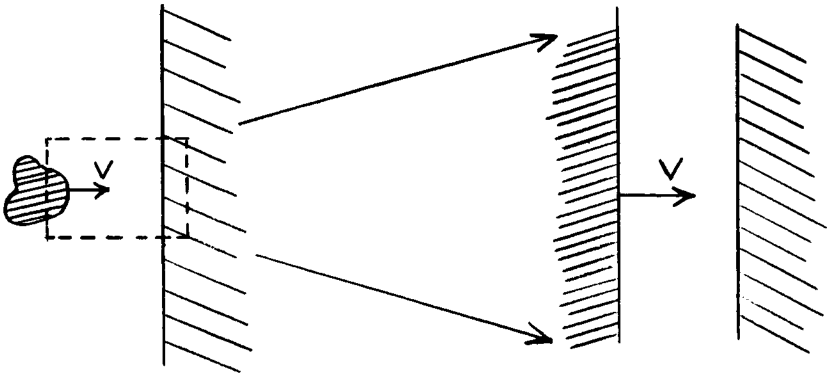

We shall see below how to calculate exactly the pressure p_1, internal energy e_1, density ρ_1, and particle velocity u_1, behind the shock wave that starts into the target, as well as the speed of the shock, u_s. For a strong shock in an ideal gas, use of the state Equation (34) in the strong-shock form of the Rankine-Hugoniot relations, Eqs. (27) - (30), reveals that these quantities would be related by

$$\frac{u_1}{u_s} = \frac{p_1}{\rho_0 u_s^2} = \frac{2}{\gamma+1} \ ; \ \frac{\rho_1}{\rho_0} = \frac{\gamma+1}{\gamma-1} \ ; \ e_1 = \frac{2}{(\gamma+1)^2} u_s^2 \tag{41}$$

The procedure suggested here is to choose the value of γ that satisfies Eq. (41), wherein the quantities u_1, e_1, p_1, and ρ_1 used are the actual values that would occur at the impact point in the target material. For example, if the target is compressed to twice normal density at the impact point, the "effective γ" for the process would be 3.0.

It should be noted that γ can be found from any of Eqs. (41), i.e.,

$$\gamma = 2\frac{u_s}{u_1} - 1 = 2\frac{\rho_0 u_s^2}{p_1} - 1 = \frac{\rho_1/\rho_0 + 1}{\rho_1/\rho_0 - 1} = \sqrt{\frac{2u_s^2}{e_1}} - 1 \tag{42}$$

Fig. 3 shows the effective γ for iron, as a function of shock speed u_s. This curve was taken from the calculated Hugoniot of Fig. 1, together with the experimental data of Altshuler et al$^{(9)}$ and of Walsh et al.$^{(11)}$ Typically of most materials, the effective γ is on the order of 10 to 20 for weak shock waves, and is more like 2 to 3 for strong shock waves.

To calculate the actual conditions at the impact point, only the Hugoniot curves of the projectile and target are needed. Consider the impact, at speed V, of two semi-infinite bodies

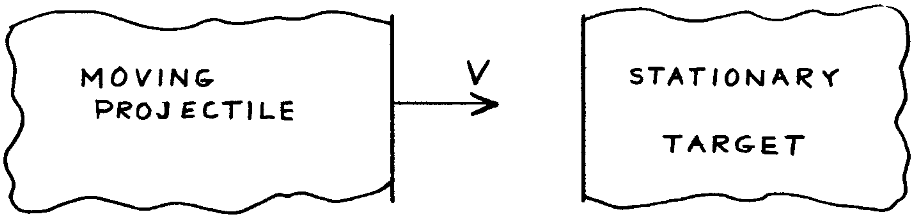

Immediately after impact, a shock wave moves into the target at speed V_s, and the material behind it, at pressure p_i, follows the shock at speed V_i

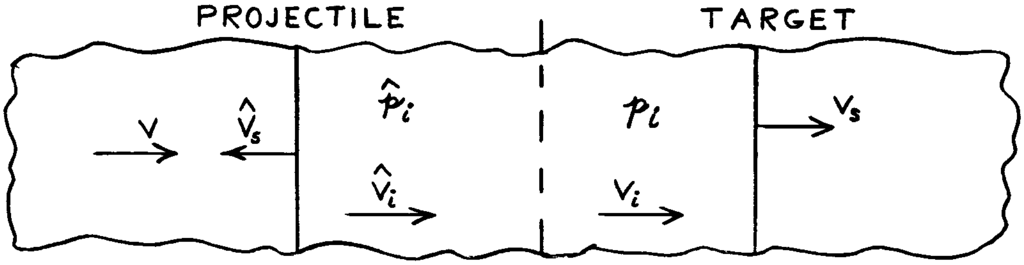

Meanwhile, another shock wave propagates back into the oncoming projectile material, reducing its speed from V to $\hat{V}_i$, and raising its pressure to $\hat{p}_i$. Equality of pressure and particle speed across the interface requires that $p_i = \hat{p}_i$ and $V_i = \hat{V}_i$. Consider now the shock propagation in each medium separately, in each case using a coordinate system such that the shock moves into a medium at rest

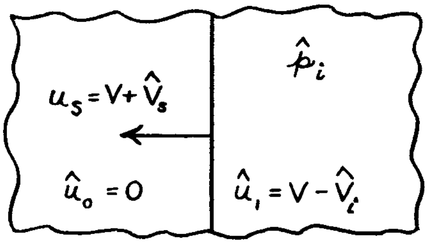

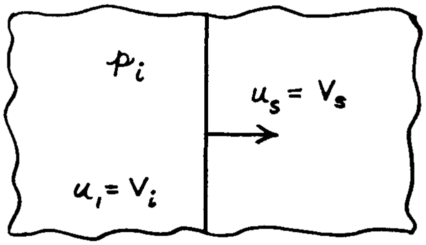

The problem is to choose, for a given impact speed V, a pair of values V_s and $\hat{V}_s$ such that $p_i = \hat{p}_i$ and $V_i = \hat{V}_i$. Olshaker and Bjork[(12)] have described a convenient graphical method of solution. For the present purpose, where the solution is required over a range of impact speeds, it is much simpler to turn the problem around, choosing the pressure at the interface, and asking what impact speed this corresponds to. The choice of p_i (which equals $\hat{p}_i$) determines the particle velocities u_1 and $\hat{u}_1$, from the Hugoniot curves for the two materials. The impact speed is then determined by the equality of particle speeds in the laboratory frame of reference, namely

$$\begin{aligned} V_i &= u_1 = \hat{V}_i = V - \hat{u}_1 \\ \text{or} \quad V &= u_1 + \hat{u}_1 \end{aligned} \tag{43}$$

The value of γ can then be found from any of Eqs. (42). This process is illustrated in Fig. 4; here are shown the p_1, u_1 Hugoniot data for iron and lead, taken from Altshuler et al.[(9)] Choosing an interface pressure of 8 megabars gives u_1 = 6.6 km/sec and 7.0 km/sec in lead and iron, respectively. Thus the impact speed required to generate these conditions must have been 13.6 km/sec. If lead is the target, the effective γ is determined as follows:

a) The shock speed is determined, either from a graph of u_1 vs. u_s, or p_1 vs. u_s, or else from Eq. (14a)

$$u_s = \frac{p_1}{\rho_0 u_1} = 10.69 \text{ km/sec}$$

b) γ is then found from Eqs. (4)

$$\gamma = \frac{2u_s}{u_1} - 1 = 2.24$$

Repeating this process at a succession of values of p_1 determines $\gamma(V)$, as shown in Fig. 5.

The determination of $\gamma(V)$ takes on a simple form when the shock velocity and particle velocity are linearly related

$$u_s = c + s u_1 \tag{44}$$

The measured Hugoniots for many materials are well approximated by this relation, at least up to pressures around two megabars. Table I lists values of c and s for a number of materials. Using Eq. (14a), the particle velocity corresponding to a given pressure is

$$u_1 = c \left\{ \frac{\sqrt{1 + 4s\, p_1/\rho_0 c^2} - 1}{2s} \right\} \tag{45}$$

The impact speed can then be found by applying this formula to the projectile and target materials, and γ is found in the usual way, for example from

$$\gamma = \frac{2(c + s u_1)}{u_1} - 1 \tag{46}$$

The linear relation between shock velocity and particle velocity ceases to be valid at extremely high pressures, but our present experience indicates that it is a satisfactory extrapolation method for impact speeds up to 50 km/sec. The Grüneisen constant, Γ, may be as large as 3.0 for the materials of interest here. Thus, as long as γ is less than 4.0, the perfect-gas approximation may be interpreted in the sense indicated above, namely that the leading term of the Mie-Grüneisen equation dominates, and the choice of γ is essentially an approximation to the Grüneisen factor. If the "effective γ" is greater than 4, however, no such interpretation can be made, and the use of a perfect gas must be viewed as an attempt to match the entire Mie-Grüneisen equation with a single term. Obviously, the approximation will not be as good in this regime, and the theoretical predictions at low impact speed (i.e., high γ) must be considered less reliable on this account. An estimate of the impact conditions for which γ is less than 4.0 can easily be derived from the relations above, from which it can be shown that γ will be less than 4.0 whenever the impact pressure is greater than

$$p_1 > \rho_0 c^2 \frac{10}{(5-2s)^2}$$

As s ranges from 1 to 1.5, this pressure varies from $\frac{10}{9}\rho_0 c^2$ to $\frac{10}{4}\rho_0 c^2$ Thus, the present theory may be expected to agree with experiment at lower velocities, the lower the value of $\rho_0 c^2$. Reference to Table I, for example, shows that, at a given velocity, impacts into lead would be better described than those into, say, copper. We shall see below that this is indeed the case.

7. Conservation of Energy and Momentum. The total energy and momentum of the system must be conserved, as may be confirmed by forming the proper volume integral of the vector equations of motion, Eqs. (1) - (3). The actual integrals, whose values must be constant, may be derived as follows consider, as the mass element, a ring of volume $r\,dr\,d\theta \cdot 2\pi r \sin\theta$

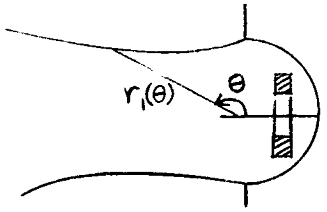

The total energy E and momentum P are

$$E = \int_0^\pi \int_0^{r_1(\theta)} \left(e + \frac{1}{2}\left[u^2 + w^2\right]\right) \rho \cdot 2\pi r^2 \sin\theta\, dr\, d\theta \tag{47}$$

$$= 2\pi \rho_0 \dot{R}_s^2 R_s^3 \int_0^\pi \sin\theta \int_0^{\eta_1(\theta)} \left(g + \frac{1}{2}\left[\phi^2 + \omega^2\right]\right) \psi \eta^2\, d\eta\, d\theta$$

$$P = \int_0^{\pi}\int_0^{r_1(\theta)} (u\cos\theta - w\sin\theta)\,\rho\cdot 2\pi r^2 \sin\theta\, dr\, d\theta$$

$$= 2\pi\rho_0 \dot{R}_s R_s^3 \int_0^{\pi} \sin\theta \int_0^{\eta_1(\theta)} (\phi\cos\theta - \omega\sin\theta)\psi\eta^2 d\eta\, d\theta \qquad (48)$$

Here we encounter a fundamental difficulty. If we are to have a self-similar solution, the differential equations require $R_s = A t^N$. However, a single value of N will not permit both of the relations above to be independent of time. Constancy of energy can be achieved only with $N = 2/5$, while momentum conservation requires $N = 1/4$, and in either case the parameter A is used to match the quantity being conserved. Thus it appears at first glance that a satisfactory solution cannot be achieved under the assumption of similarity. The essence of the difficulty is that, having used N to make one of the integrals independent of time, only a single free parameter, A , is left. But we still have two quantities to be matched, as well as a second integral to be made independent of time. We will describe, in Section C of this part, one method for overcoming these difficulties. The essence of the method is that N is determined by a totally different consideration, and a second free parameter is introduced in such a way that both conservation conditions may be satisfied simultaneously.

8. <u>Final Form of the Problem Posed.</u> The final set of differential equations that must be solved consists of Eqs. (18), (19), (20), and (36), subject to the boundary conditions at the shock $\eta = 1,\ -\pi/2 \leq \theta \leq +\pi/2$

$$\phi(1,\theta) = f(1,\theta) = \frac{2}{\gamma+1}\ ;\ \omega(1,\theta) = 0\ ;\ \psi(1,\theta) = \frac{\gamma+1}{\gamma-1} \qquad (49)$$

The value of γ is to be found, for each specific impact case, from the method outlined in Section A-6. The specification of N will be described in detail below.

As a final note on the mathematical nature of the problem, it should be pointed out that two pairs of characteristics of Eqs. (18), (19), (20), and (36) can be found by standard methods. One pair corresponds to the particle paths of the original unsteady flow, while the other pair, related to the Mach lines of the original flow, reveals that the equations have elliptic or hyperbolic character, according to whether

$$(\phi - \eta)^2 + \omega^2 - \frac{\gamma f}{\psi} \gtrless 0 \tag{50}$$

The line in the η, θ plane along which this quantity vanishes is referred to below as the "sonic" line, because of its relation to the Mach lines of the original flow.

B. Spherically Symmetric (Constant-Energy) Solution

This section describes a solution in which the shock propagation into the target is represented by one half of a spherically-symmetric disturbance:

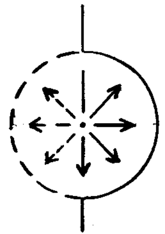

Such a solution allows variations only in the radial direction, and does not describe the pattern of mass ejection from the expanding crater. Moreover, we shall see below that only the total energy may be conserved, but not the total momentum. The justification for the use of such an apparently defective model is that it closely approximates the results found from a more acceptable (asymmetric) model. In this section, we present the symmetric solution without apology, deferring its justification until after the asymmetric solution has been treated in Section C.

1. Solution for $R_s(t)$. When the flow is spherically symmetric, all derivatives with respect to θ vanish, and the similarity equations become ordinary differential equations. Denoting the ordinary derivative with respect to η by a prime, these are

$$(\phi - \eta)\psi' + \psi\left(\phi' + 2\frac{\phi}{\eta}\right) = 0 \tag{51}$$

$$-\frac{1-N}{N}\phi + (\phi - \eta)\phi' + \frac{f'}{\psi} = 0 \tag{52}$$

$$-2\frac{1-N}{N}f + (\phi - \eta)\left(f' - \frac{\gamma f}{\psi}\psi'\right) = 0 \tag{53}$$

These may be solved explicitly for the derivatives ψ', ϕ', and f' in the form

$$\psi' = \frac{-(\phi-\eta)^2 \dfrac{2\psi\phi}{\eta} + 2\dfrac{1-N}{N} f - \dfrac{1-N}{N}\psi\phi(\phi-\eta)}{(\phi-\eta)\left[(\phi-\eta)^2 - \dfrac{\gamma f}{\psi}\right]} \tag{54}$$

$$\phi' = \frac{\dfrac{1-N}{N}\phi(\phi-\eta) + \dfrac{\gamma f}{\psi}\,\dfrac{2\phi}{\eta} - 2\dfrac{1-N}{N}\,\dfrac{f}{\psi}}{(\phi-\eta)^2 - \dfrac{\gamma f}{\psi}} \tag{55}$$

$$f' = \frac{f\left\{(\phi-\eta)\left[2\dfrac{1-N}{N} - \dfrac{2\gamma\phi}{\eta}\right] - \gamma\dfrac{1-N}{N}\phi\right\}}{(\phi-\eta)^2 - \dfrac{\gamma f}{\psi}} \tag{56}$$

The boundary conditions at the shock are

$$\phi(1) = f(1) = \frac{2}{\gamma+1} \quad ; \quad \psi(1) = \frac{\gamma+1}{\gamma-1} \tag{57}$$

Equations (54) - (56) (with $N = 2/5$) were first presented by G. I. Taylor,(13) who worked out a few numerical and approximate analytic solutions, for γ ranging from 1.2 to 1.67, the range appropriate for gases. Subsequently, an analytic solution of these equations (also with $N = 2/5$) was published by J. L. Taylor,(14) Latter,(15) and Sakurai.(16) Simultaneously with Taylor's work, Sedov(6) had also found this analytic solution. He worked in a different coordinate system, where

$$x = \frac{N\phi}{\eta}, \qquad y = \frac{N^2}{\eta^2}\,\frac{\gamma f}{\psi} \tag{58}$$

In these coordinates, the basic equations may be combined to yield a single differential equation involving only y and x (see Appendix A for details of the derivation):

$$\frac{x-N}{y}\,\frac{dy}{dx} = -(\gamma-1) + \frac{\left[(x-N)^2 - y\right]\left[2-(3\gamma-1)\,x\right]}{y\left[3x - \frac{2}{\gamma}(1-N)\right] - x\,(x-N)(x-1)} \tag{59}$$

Having y as a function of x , the quantities η and ψ are found by integrating

$$\eta\,\frac{dx}{d\eta} = \frac{y\left[3x - \frac{2}{\gamma}(1-N)\right] - x\,(x-N)(x-1)}{(x-N)^2 - y} \tag{60}$$

$$(x-N)\,\frac{\eta}{\psi}\,\frac{d\psi}{d\eta} = -\eta\,\frac{dx}{d\eta} - 3x \tag{61}$$

The boundary conditions at the shock are

$$x_{SH} = \frac{2N}{(\gamma+1)} \qquad\qquad y_{SH} = \frac{2\gamma N^2(\gamma-1)}{(\gamma+1)^2} \tag{62}$$

The parameter N must be specified, before solutions of these equations can be found. It appears that physically acceptable solutions of these equations exist only when $N = 2/5$, a value which conserves the total energy, according to Section A-7 above. When N is taken to be different from 2/5, the solution exhibits infinite slopes. In fact, by working in the x, y coordinates, the solution can be shown to become double-valued. Figure 6 shows results typical of those found in the range $0.25 \leq N \leq 0.4$ when a solution of this sort is attempted. This nonexistence of symmetric solutions apparently explains the difficulty encountered by Davids, Huang, and Juanzemis[17] in attempting to find a spherically-symmetric solution for constant momentum ($N = 1/4$).

In what follows, N is chosen as 2/5, and the terms "constant-energy" and "spherically-symmetric" are used interchangeably in referring to the solution.

The closed-form solution found by Sedov (or equivalently, with η as independent variable, by Latter, J. L. Taylor, and Sakurai) is

$$y(x) = \frac{\gamma(\gamma-1)}{2} x^2 \, \frac{2/5 - x}{\gamma x - 2/5} \tag{63}$$

and expressions for the remaining details of the solution can be found, for example in Sedov(6) or in Hayes and Probstein.(18) Detailed numerical results are given only for γ in the range appropriate to gases. Calculations have been done for γ = 2, 3, 4, 5, 6, 8, 10, 12, 16, and 20, and the distributions of velocity, density, and pressure are shown in Figs. 7a-j. These figures display the usual feature, that in all cases the density drops off rather sharply behind the shock, indicating that most of the mass processed is concentrated near the shock. As γ approaches seven, the distributions approach the exact solution, for $\gamma = 7$(6)

$$\psi = \frac{4}{3}\eta \quad , \qquad \phi = \frac{1}{4}\eta \quad , \qquad f = \frac{1}{4}\eta^3 \tag{64}$$

For γ greater than seven, a cavity begins to form at small values of η, as pointed out in Sedov,(6) and the particle velocities show a marked increase near the edge of this cavity.

Having these distributions, an explicit description of the shock propagation can now be given, if the total energy E of the system is specified. The sum of the internal and kinetic energy of the fluid that has been set into motion is given by the integral

$$\int_0^{R_s} \left(e + \frac{1}{2}u^2\right)\rho \cdot 2\pi r^2 dr = \int_0^{R_s} \left(\frac{1}{\gamma-1}\,\frac{p}{\rho} + \frac{1}{2}u^2\right) 2\pi\rho r^2 dr \tag{65}$$

$$= 2\pi\rho_0 R_s^3 \dot{R}_s^2 \, I_1(\gamma)$$

where,

$$I_1(\gamma) = \int_0^1 \left(\frac{1}{(\gamma-1)} \frac{f}{\psi} + \frac{1}{2}\phi^2 \right) \psi \eta^2 d\eta \tag{66}$$

This integral has been evaluated for the values of γ mentioned above, and is shown in Fig. 8. The values obtained by G. I. Taylor(13) at lower values of γ are also shown here, together with the result reported by Davids and Huang(19) at $\gamma = 16$, about which more will be said below. A further check is the value $I_1 = 1/72$ when $\gamma = 7$, which can be found by a simple integration.

If the total energy E is now specified, a simple differential equation for $R_s(t)$ results

$$E = 2\pi \rho_0 R_s^3 \dot{R}_s^2 I_1(\gamma) \tag{67}$$

The term $2\pi\rho_0 R_s^3$ is three times the target mass processed up to the time t. Thus, $3I_1(\gamma)$ may be thought of as a dimensionless coefficient giving the ratio of the mass-averaged value of $e+\frac{u^2}{2}$ to the quantity $\dot{R}_s^2$, i.e.

$$3I_1(\gamma) = \frac{E\Big/\frac{2}{3}\pi\rho_0 R_s^3}{\dot{R}_s^2} = \frac{\left(e+\frac{1}{2}u^2\right)_{AVG.}}{\dot{R}_s^2} \tag{68}$$

But $\dot{R}_s^2$ is proportional to the energy at the shock

$$\dot{R}_s^2 = \frac{(\gamma+1)^2}{4}\left(e+\frac{1}{2}u^2\right)_{SH} \tag{69}$$

Thus

$$I_1(\gamma) = \frac{4}{3(\gamma+1)^2} \frac{\left(e+\frac{1}{2}u^2\right)_{AVG.}}{\left(e+\frac{1}{2}u^2\right)_{SH}} \tag{70}$$

Because most of the mass is concentrated near the shock, the mass-averaged value of any quantity is very nearly its value at the shock. Thus the factor $4/3(\gamma+1)^2$ is a good approximation to $I_1(\gamma)$, as shown in Fig. 8. This factor originates from Eq. (69), which states that the larger the value of γ, the larger must be the shock speed, if a given energy is to be achieved behind the shock. We may attach the same significance to $I_1(\gamma)$: if a given energy is to be distributed in two materials for which the γ's differ, the shock speed will have to be greater in the material having the larger γ.

The solution of Eq. (67) is simply the Taylor solution for a strong blast wave

$$R_s(t) = \left(\frac{25}{8\pi I_1(\gamma)} \frac{E t^2}{\rho_0}\right)^{1/5} \tag{71}$$

Here the influence of γ is shown more clearly. For given E and ρ_0, the shock radius will grow more rapidly for large values of γ :

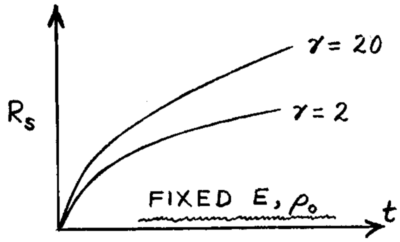

To apply Eq. (71) to a given case, the total energy E must be specified. In all the applications made below, this energy is taken to be the kinetic energy of the impacting particle.

Figures 9a and 9b present a comparison of the Taylor solution with experiment. Eichelberger and Gehring(1) have published time histories of the shock and crater radius, for a Lucite block struck by an iron pellet at 4.6 km/sec. These time histories are compared with the prediction of

Eq. (71) in Fig. 9a. The agreement is reasonable, although the measured rate of advance of the shock is faster than that of the constant-energy solution, corresponding to a value of N around 0.67. It is important, in this connection, to recall that any constant-energy, self-similar solution will have $N = 0.4$. Changing the value of γ will change only the amplitude. In addition, any equation of state that permits a similarity solution will also leave N unchanged in a constant-energy solution. Furthermore, in a solution which conserves both energy and momentum, the evidence advanced in Section C below suggests that, if anything, N will be less than 0.4. On the other hand, it is true in general that the shock speed will decelerate from the blast-wave behavior $(R_s \sim t^{2/5})$ at early time to the acoustic limit $(R_s \sim t)$ at late time. The data of Fig. 9a apparently lie in a transitional regime between these two limits. Thus it appears that the only way to achieve a better comparison with the data of Fig. 9a is to include the nonsimilar effect, associated with the term $\Delta(\rho)$ in the equation of state. The present report does not treat this effect, but it is encouraging to note how well the blast-wave theory does in spite of this deficiency. Moreover, the blast-wave theory can be expected to improve at higher impact speeds.

Figure 9b presents a different type of experimental check on the blast-wave theory. Here we show the wave speed versus shock position, measured in a very ingenious series of experiments by Frasier and Karpov.(2) The data pertain to a wax target, struck by an Ethocell pellet at 4 km/sec, and apparently lie in a range where the shock strength is too low to justify the strong-shock assumptions. However, the data do not appear to be inconsistent with a transition from a high shock speed down to the stress-wave velocity. The constant-energy solution is not extrapolated beyond this velocity, since the blast-wave approximation is clearly inadequate in that range.

In general, then, the blast-wave solution may be considered a reasonable approximation to this very limited amount of experiment, and, if used with caution, may be expected to serve as a suitable basis for crater prediction.

2. Crater formation criterion. The blast-wave solution given in Eq. (71) may be considered a valid description of the shock propagation in the target so long as the pressures being generated are large enough to justify an inviscid-fluid model. These pressures decay rapidly, however, and to provide a valid solution at later time, a transition is needed from the blast-wave model to one which properly describes the plastic flow, and ultimately the elastic response of the target. Such a solution would predict the configuration in which the target material finally comes to rest, and the definition of the final crater dimensions would be unequivocal. A solution of this sort is not presently available, however. In its absence, the best that can be done is to identify the point at which the transition from blast-wave theory ought to occur, and to make an estimate, based on conditions at that instant, of what the final crater dimensions will be.

The method for predicting crater size that is adopted in the present report is that the shock radius at the instant at which the blast-wave solution is to be cut off is the radius of the crater that will ultimately develop. The use of such a procedure is equivalent to the statement that all of the material processed by the high-pressure phases of the shock wave will ultimately be ejected from the target.

The cutoff point must be the point at which the shock-wave intensity has decayed to some preassigned level. If we require that the pressure behind the shock shall have fallen to the level $\mathbb{P}$ (to be identified below with the material strength), then, since the pressure behind the shock is given in general by

$$p_1 = \frac{2}{\gamma+1} \rho_0 \dot{R}_s^2 \tag{72}$$

we would identify the crater radius as the value of R_s at the instant when

$$\dot{R}_s = \sqrt{\frac{\gamma+1}{2} \frac{\mathbb{P}}{\rho_0}} \tag{73}$$

If the solution for the shock radius is written as

$$R_s = A t^{2/5} \ , \qquad A = \left(\frac{25}{8\pi I_1} \frac{E}{\rho_0} \right)^{1/5} \tag{74}$$

then the time can be replaced in favor of the shock radius, according to

$$t = \left(R_s / A \right)^{5/2} \tag{75}$$

The shock speed is therefore

$$\dot{R}_s = \frac{2}{5} A t^{-3/5} = \frac{2}{5} A \left(\frac{A}{R_s} \right)^{3/2} \tag{76}$$

Equating this to Eq. (73), and replacing R_s by the crater radius R_c, we have

$$\frac{2}{5} A \left(\frac{A}{R_c} \right)^{3/2} = \sqrt{\frac{\gamma+1}{2} \frac{\mathbb{P}}{\rho_0}}$$

or

$$R_c = \left(\frac{1}{\pi(\gamma+1) I_1(\gamma)} \frac{E}{\mathbb{P}} \right)^{1/3} \tag{77}$$

Taking E to be the kinetic energy of a spherical projectile of density ρ_p and diameter d then gives

$$\frac{R_c}{d} = \left(\frac{1}{12\,(\gamma+1)\,I_1(\gamma)} \; \frac{\rho_p V^2}{\mathbb{P}} \right)^{1/3} \tag{78}$$

This solution is shown in Fig. 10 for various values of γ. For a given projectile-target combination, γ is large at low impact speeds, and decreases as V increases. Thus the crater radius is predicted to grow with a power of V somewhat less than 2/3. In most cases, the power is approximately 1/3. The influence of γ displayed in Fig. 10 is the same as that mentioned earlier: at a given kinetic energy, the higher values of γ produce faster shock waves, which will penetrate more deeply before they decay to the prescribed pressure $\mathbb{P}$. Stated another way: if a given energy is to be added to the target by a shock wave across which the energy change per unit shock speed is relatively small, then the shock speed itself must be relatively large. We will return to a discussion of this point below.

The value of $\mathbb{P}$ must be chosen, in order to predict actual crater dimenions. It was pointed out above that the inviscid-fluid approximations are valid only so long as the pressures being generated at the shock are large compared with the target's resistance to shear deformation. Thus, the pressure at which the blast-wave solution is to be cut off must be a measure of the shear strength of the material. Part II, below, points out that the proper value to use for this property is the intrinsic shear strength, which lies between the limits $G/30$ and $G/2\pi$, G being the dynamic shear modulus, as measured, for example, by ultrasonic techniques. Using these values for the intrinsic shear strength, the predictions of Eq. (71)

are compared with experiment in Figs. 11-13. In preparing the theoretical curve for iron striking lead (Fig. 11), the variation of γ and V was taken from Fig. 5, and the material properties used were found from Table 4 . The lower strength leads to a deeper crater prediction, since the shock wave must penetrate more deeply in decaying to a lower pressure. The experimental data, taken from the compilation by Herrmann and Jones(20) are seen to agree quite well with the higher-strength prediction. Figure 12 gives results for iron striking iron. In addition to low-speed experimental data, this figure also shows Bjork's machine solution. Again the agreement is reasonable. Figure 13 shows the results found for aluminum striking copper. Here the agreement with experiment is somewhat poorer. The Hugoniot data for iron, lead, and copper were taken from Altshuler et al,(9) while for aluminum the low-pressure data of Walsh et al(11) were used, together with the high-pressure estimate made by Lake and Todd.(21)

On the basis of this evidence, it would appear that the best agreement with experiment is achieved by using the value $G/2\pi$ for the intrinsic shear strength. Part II, below, presents a discussion of why such a conclusion might be expected.

The approximations on which this theory is based will improve at higher impact speeds. Thus it is not surprising to find such good agreement for the case of lead targets, in which hypervelocity conditions are achieved at relatively low speed. The fact that the slope of these data and of Bjork's results are well matched lends substance to the belief that crater radius will grow somewhat more slowly with impact speed in the very high-speed range, compared with its growth rate at lower speed.

3. Scaling Laws. The only target properties that appear in the crater-size formula are the strength $\mathbb{P}$ and the equation of state, as represented by $\mathcal{I}_1(\gamma)$. For the materials considered, however, the latter influence is of secondary importance, since $\gamma(V)$ is approximately the same for a variety of projectile-target combinations. This point is illustrated in Figs. 14a, b, and c, which show the functions $\gamma(V)$ for targets of Aluminum, Beryllium, Iron, Molybdenum, Columbium (Niobium), Vanadium, Tantalum, Tungsten, and Lead, being struck by projectiles of Fused Quartz, Aluminum, and Iron. These calculations used the data of Table I and the equations of Section A6, Part I. Crater-size predictions for these projectile-target combinations can now be made by using these results for $\gamma(V)$ in conjunction with Fig. 10. Thus an important scaling law is that the crater radii produced in two targets, by a given projectile impacting at a given speed, will have the ratio

$$\frac{R_c)_1}{R_c)_2} \approx \left(\frac{\mathbb{P}_2}{\mathbb{P}_1}\right)^{1/3} \tag{79}$$

The fact that $\gamma(V)$ is not greatly different for various materials also permits a simple scaling with respect to projectile density. For impact into a given target at given speed, the craters made by different projectiles are related by

$$\frac{R_c)_1}{R_c)_2} \approx \left\{\frac{(\rho_p)_1}{(\rho_p)_2}\right\}^{1/3} \tag{80}$$

Finally, it should be noted that the scaling shown here differs from that recommended by Olshaker and Bjork.(12) Their scaling is based on the observation that craters produced in a given target by projectiles of various materials, all having the same mass and velocity (and thus different diameter are proportional to the particle velocity generated in the target at the impact point. Thus, for B striking A ,

$$R_c)_{B \rightarrow A} = \text{const} \times u_1)_{\text{in } A}, \text{ at the impact point} \tag{81}$$

The experimental data which provide the basis for this scaling are all taken at relatively low impact speeds. Because the particle speed at the impact point is one half the impact speed for like-on-like impacts, the scaling law can be written as

$$\frac{R_c)_{B \rightarrow A}}{R_c)_{A \rightarrow A}} = \frac{u_1)_{B \rightarrow A}}{V/2} \tag{82}$$

If the shock driven into A by B is stronger than that driven into A by A , this scaling would predict a larger crater for B striking A than for A striking A . The present theory gives a different scaling law; for given kinetic energy of the projectile, and given $\mathbb{P}$,

$$\frac{R_c)_{B \rightarrow A}}{R_c)_{A \rightarrow A}} = \left\{ \frac{[(\gamma+1) I_1(\gamma)]_{A \rightarrow A}}{[(\gamma+1) I_1(\gamma)]_{B \rightarrow A}} \right\}^{1/3} \tag{83}$$

It can be seen from Eq. (46) that γ decreases as u_1 increases. Thus, for the case mentioned above, where $u_1)_{B \rightarrow A} > V/2$, it follows that $\gamma_{B \rightarrow A} < \gamma_{A \rightarrow A}$, so the prediction of the present theory would be $R_c)_{B \rightarrow A} < R_c)_{A \rightarrow A}$ just the reverse of that predicted by the Olshaker-Bjork formula. The reason for the difference is simply due to the influence of γ that has been discussed above. Although the present theory uses the shock strength at the impact point to determine γ , nevertheless the solution does not match the shock speed at that point. Rather, the role of γ is to characterize the strength of the shock throughout its entire subsequent history. The stronger the shock, the less rapidly it must travel, on the average, in order to transfer a given energy to the target.

Unfortunately, the data required to resolve this difference are not presently available. In actual fact, of course, the speed of the shock as it advances into the target will remain close to the one-dimensional, impact-point value until the time when the projectile has been destroyed. Thereafter, its speed will be governed by the requirement that the total energy and momentum be conserved. One must certainly expect that the Olshaker-Bjork type of scaling will be correct when the entire cratering process is controlled by conditions during the time when the projectile is being destroyed. This condition has been shown to exist at low impact speed. Whether it will continue to hold at higher impact speeds is presently open to question. On the other hand, the blast-wave theory in its present form is valid only at impact speeds such that the collision time is a small fraction of the time required for the crater to form, and so its predictions are relatively insensitive to the details of the impact process. The fact that it leads to a scaling law different from that observed at low speed is therefore not surprising, but must be regarded as tentative, pending the availability of a less approximate theory, and of definitive experiments.

It would appear that these qualitative conclusions would remain unchanged even if more realistic Grüneisen coefficients were employed in a blast-wave solution. The extent by which they might be modified by the results of a non-similar solution will form an interesting area for further research.

4. Comparison with Other Theories. It is of interest to compare the present analysis with a similar theory given by Davids et al.(17),(19) These authors also use a spherically symmetric model, and represent the equation of state by a gas of constant γ , which they determine by fitting the Hugoniot (not the isentropes) by an equation of the form $p \sim \rho^{\gamma}$. They work out a numerical solution for $\gamma = 16$, and $N = 2/5$, but apparently do not take advantage of the closed-form solution. The value which they find numerically for the cavity radius differs slightly from that given by the exact result, and this small discrepancy may explain why their value of $I_1(\gamma)$, plotted in Fig. 8, is somewhat below the present results. As noted earlier, they have also attempted a solution for constant momentum ($N = 1/4$). The principal difference between their theory and the one described here lies in the criterion used for crater formation. Like Bjork, these authors do not incorporate the material strength. Rather, they define the crater as the cavity radius at the point where a certain graph of shock radius versus time is judged to have reached an essentially constant value. They infer from this that crater radius will vary as the 2/5 power of the impact speed.

The present formula for crater size is very similar to that derived empirically by Eichelberger and Gehring.(1) Their result states that the crater volume varies directly with the kinetic energy of the projectile, and inversely with the Brinell hardness of the target, B

$$\frac{2}{3}\pi R_c^3 = 4 \times 10^{-9}\,\frac{E}{B}$$

where E and R_c are taken in cgs units, and B in the customary units of kilograms force per square millimeter. The present result is

$$\frac{2}{3}\pi R_c^{3} = \frac{2}{3(\gamma+1)\,I_1(\gamma)} \quad \frac{E}{G/2\pi}$$

which differs from Eichelberger and Gehring's formula by the influence of γ, and by the use of $G/2\pi$. There appears to be no simple relation between the dynamic shear modulus and the Brinell hardness, so that no general comparison can be made. For the case of copper, $G/2\pi$ is about ten times the Brinell hardness, and the two crater-size predictions are equal at $\gamma = 4.6$, a representative value. In general, both predictions yield the same order of magnitude, and differ principally in that the present one indicates a lower growth rate of crater size with impact speed.

C. Asymmetric Solutions[*]

In this section we present a blast-wave solution which explicitly describes the pattern of mass ejection from the target. Because of the lack of spherical symmetry, two independent variables enter, and the solution of the problem is considerably more difficult to find. Certain approximations are resorted to, in order to obtain partial solutions. From these, a very important result is found, namely that this more difficult, but more physically realistic solution is for practical purposes the same as the vastly-simpler constant-energy solution described above.

In addition, this section returns to the question of the simultaneous conservation of energy and momentum, and describes one method by which this can be achieved. The method is illustrated by applying it to the case of a one-dimensional impact, such as might occur when a thin disk strikes a target.

The first six of the subsections below describe the axisymmetric case, while the last three present the one-dimensional solution.

1. Two-Dimensional Solution. The model which allows for spatial variations in two directions behind a hemispherical shock wave was introduced in Section A, above. The similarity equations, Eqs. (18) - (20), and Eq. (36), are partial differential equations, containing both η and θ

---

[*] The term "asymmetric" as used here refers to symmetry with respect to the target surface, while the term "axisymmetric" refers to symmetry about the axis along which the projectile impacts. All of the solutions of this report are taken to be axisymmetric, but may be either symmetric or asymmetric with respect to the target surface.

as independent variables. They are of mixed character, containing both elliptic and hyperbolic regions, and, furthermore, they must meet a zero-pressure boundary condition along a line whose location is unknown in advance. To make matters worse, the differential equations contain a parameter N whose value is unspecified. No attempt has been made to solve these equations. Instead, partial solutions are sought by restricting attention to conditions along the axis of symmetry. In this way, we can learn a great deal about the solution, with relatively little effort. The most important item uncovered is the criterion for choosing N : for each γ , N must be chosen so as to permit a smooth transition from the elliptic to the hyperbolic region.

In the similarity coordinates, the flow field has the appearance

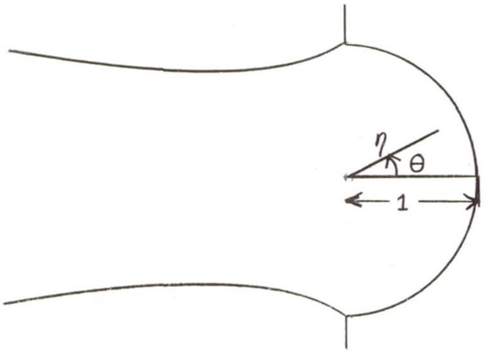

In the undisturbed region, it is as though fluid particles were all converging radially toward the origin. They pass through the shock, and are ultimately ejected toward the low-pressure region outside. On the basis of the spherically symmetric solution, we may expect that most of the mass processed at any instant is heavily concentrated near the shock. Thus the problem bears a marked resemblance to the steady, hypersonic flow over a blunt body

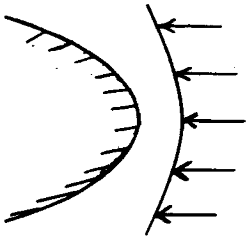

and we may expect that analytical methods which are successful in treating that problem may also be used to good advantage in the present case. One such method is to investigate the solution along the axis of symmetry:

$$\theta = 0 \; : \; 0 \leq \eta \leq 1 \; ; \quad \theta = \pi , \quad 0 \leq \eta \leq \infty \tag{84}$$

Along this line, the axial symmetry of the problem requires that all first derivatives with respect to θ be zero, except for the derivative of the tangential velocity component. This component is antisymmetric in θ ; for example, in the case where material is flowing outward from the region near the axis

$\vec{q}$ denotes resultant velocity:

$$\vec{q} = \vec{u} + \vec{w}$$

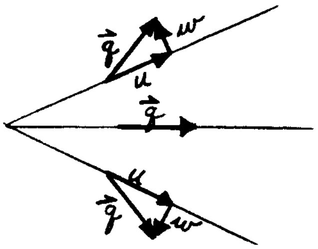

the distribution of ω at a given radius has the appearance

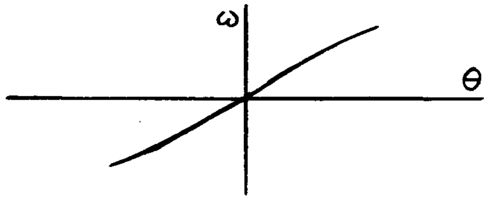

Thus $\frac{\partial \omega}{\partial \theta}(\eta, 0) \neq 0$. Denoting this quantity by $\frac{1}{2}\tau$:

$$\tau(\eta) = 2 \frac{\partial \omega}{\partial \theta} \; (\eta \; ; \; \theta = 0 \text{ or } \pi) \tag{85}$$

The similarity equations, along the axis of symmetry, become

$$(\phi - \eta)\psi' + \psi\left(\phi' + \frac{\tau}{\eta} + 2\frac{\phi}{\eta}\right) = 0 \tag{86}$$

$$-\frac{1-N}{N}\,\phi + (\phi-\eta)\,\phi' + \frac{f'}{\psi} = 0 \tag{87}$$

$$-2\,\frac{1-N}{N}\,f + (\phi-\eta)\left(f' - \frac{\gamma f}{\psi}\,\psi'\right) = 0 \tag{88}$$

where primes indicate ordinary differentiation with respect to η . These equations are referred to in what follows as the "centerline" equations. Except for the presence of τ in (86), these are identical with the Taylor equations for a spherically-symmetric disturbance, discussed in Section B. The function $\tau(\eta)$ represents the influence of off-axis conditions, as must be expected whenever a partial differential equation is specialized to a single line in the plane of its independent variables.

Equations (86) - (88) may be solved explicitly for the derivatives in the form

$$\psi' = \frac{-(\phi-\eta)^2\left(\frac{2\psi\phi}{\eta} + \frac{\psi\tau}{\eta}\right) + \frac{2(1-N)}{N}\,f - \frac{1-N}{N}\,\psi\phi\,(\phi-\eta)}{(\phi-\eta)\left\{(\phi-\eta)^2 - \frac{\gamma f}{\psi}\right\}} \tag{89}$$

$$\phi' = \frac{\frac{1-N}{N}\,\phi\,(\phi-\eta) + \frac{\gamma f}{\psi}\left(\frac{2\phi}{\eta} + \frac{\tau}{\eta}\right) - \frac{2(1-N)}{N}\,\frac{f}{\psi}}{(\phi-\eta)^2 - \frac{\gamma f}{\psi}} \tag{90}$$

$$f' = \frac{f\left\{(\phi-\eta)\left[2\,\frac{1-N}{N} - \gamma\left(\frac{2\phi}{\eta} + \frac{\tau}{\eta}\right)\right] - \gamma\,\frac{1-N}{N}\,\phi\right\}}{(\phi-\eta)^2 - \frac{\gamma f}{\psi}} \tag{91}$$

The boundary conditions at the shock are

$$\phi(1) = f(1) = \frac{2}{\gamma+1}\ ; \quad \psi(1) = \frac{\gamma+1}{\gamma-1}\ ; \quad \tau(1) = 0 \tag{92}$$

These equations contain two unspecified quantities, N and $\tau(\eta)$. The next two subsections discuss the determination of these.

2. Criterion for Choosing N. The centerline equations obviously have a singularity at the point where the denominator $(\phi-\eta)^2 - \frac{\gamma f}{\psi}$ vanishes. This quantity is the special case, for $\omega = 0$, of the function discussed in Section A-8, whose sign determines whether the partial differential equations have elliptic or hyperbolic character. Thus the point on the axis of symmetry where this denominator changes sign corresponds to the intersection of the "sonic line" with the axis. In order that the solution may pass smoothly through this singular point, the numerators of Eqs. (89) - (91) must also vanish at this point. A little algebra shows that this condition may be achieved simultaneously in all three numerators if

$$(\phi^*-\eta^*)\left\{\frac{2}{\gamma}\frac{1-N}{N} - 2\frac{\phi^*}{\eta^*} - \frac{\tau^*}{\eta^*}\right\} = \frac{1-N}{N}\phi^* \tag{93}$$

where the asterisk denotes conditions at the sonic point. The function $\tau(\eta)$ cannot be chosen arbitrarily; thus the only parameter that can be used to guarantee a smooth crossing of the sonic point is N, and this consideration forms the criterion for the choice of N. For each γ, and a specification of τ, N is chosen so as to provide a continuous transition through the singularity. Thus N will in general be a function of γ. It should be noted in passing that this problem never came up in the spherically-symmetric, constant-energy case. There the vanishing of the denominator always coincides with either the origin $\eta = 0$ (for $\gamma \leq 7$) or with the edge of the cavity (for $\gamma > 7$), so the entire flow field is elliptic in a constant-energy solution.

3. Approximations for $\tau(\eta)$. In order to actually carry out a smooth crossing of the sonic point, Eqs. (89) - (91) must be solved for various values

of N (and given γ) until such a crossing is found. Before such an integration can be done, however, $\tau(\eta)$ must be specified. In actual fact, no rigorous determination of $\tau(\eta)$, and with it $N(\gamma)$, can be made without solving the full partial differential equations. Approximations to N may be found, however, by approximating τ , and then integrating Eqs. (89)-(91). Rather than approximating τ itself, one may instead relate τ to other physical quantities which may be approximated more easily. In particular, by differentiating Eq. (20), the θ -component of the momentum equation, with respect to θ , and by then specializing to the axis of symmetry, one finds

$$-\frac{1}{2}\ \frac{1-N}{N}\ \tau+\frac{1}{2}(\phi-\eta)\tau'+\frac{\tau^2}{4\eta}+\frac{\phi\tau}{2\eta}+\frac{1}{\eta\psi}\ \frac{\partial^2 f}{\partial\theta^2}(\eta,0)=0 \qquad (94)$$

from which it is seen that approximations to the pressure distribution* can be used to generate corresponding approximations to $\tau(\eta)$. This process can be continued, of course, by taking higher-order derivatives, with respect to θ , of any of the equations of motion. Each of the resulting expressions will contain at least one unknown function, so the utility of the procedure is dictated by one's ability to approximate the unknown function. For this purpose, Eq. (94) is especially useful. At the shock, the pressure is uniform, while behind the shock it begins to decrease. The rate of decrease is faster near $\theta = \pm\frac{\pi}{2}$, as the influence of the vacuum outside the developing crater makes itself felt. Qualitatively, the pressure distribution would

---

* Approximations to the pressure distribution are what make possible centerline solutions of the blunt-body problem.

be expected to have the appearance

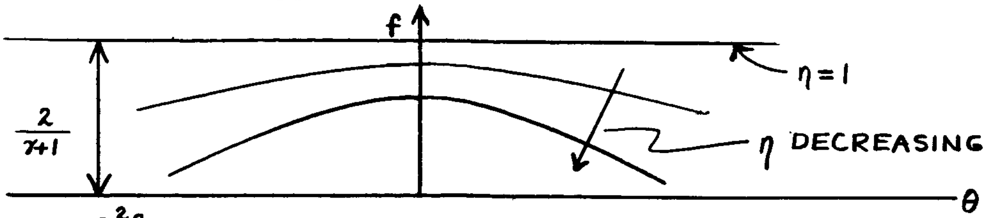

The quantity $\frac{\partial^2 f}{\partial \theta^2}(\eta, 0)$, which is essentially the curvature of these lines at $\theta = 0$, will be zero at the shock, and will become negative with increasing magnitude as η falls below one. Such considerations suggest the approximation

$$\frac{\partial^2 f}{\partial \theta^2}(\eta, 0) = -K(1-\eta)^a f(\eta, 0) \tag{95}$$

where K and a are constants. Crudely, one may think of this approximation as fitting a cosine variation to the curves above, with a multiplicative function of η introduced in such a way as to guarantee zero curvature at the shock.

The constants K and a must be chosen so as to yield values of τ which are at most of unit order. This consideration is derived from the fact that, near the axis, the velocity vectors are expected, on physical grounds, not to diverge very rapidly from the axis

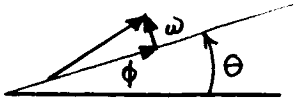

The angle which the velocity vector makes with the radius is of order $\frac{\partial \omega}{\partial \theta}(\eta, 0)\,\frac{\theta}{\phi}$. But both θ and ϕ are of order one or less. Thus the order of $\partial\omega/\partial\theta$ must be the same, if the velocity vectors are to diverge from the axis at a moderate rate.

4. <u>Results for $a = 1$, $K = 1, 10.$</u> A limited number of solutions

have been calculated, using the values $\alpha = 1$, $K = 1.0$ and 10. For a given value of γ, and selected values of N, Eqs. (89), (90), (91) and (94) are integrated by a Runge-Kutta procedure, starting from the shock values given by Eq. (92). The results found with $\alpha = 1$, $K = 10$, $\gamma = 3$, and $N = 0.374, 0.375$, and 0.376, are shown in Fig. 15a. The first graph on this figure displays the denominator, whose vanishing identifies the "sonic" point. The second plot shows the function $H(\eta)$, defined as

$$H(\eta) = (\phi - \eta)\left\{\frac{2}{\gamma}\,\frac{1-N}{N} - \frac{2\phi}{\eta} - \frac{\tau}{\eta}\right\} - \frac{1-N}{N}\,\phi \tag{96}$$

which, according to Eq. (93), must also vanish at the sonic point if an acceptable solution is to be achieved. This does occur at $N = 0.375$, and the corresponding distributions of ψ, ϕ, f, and τ are shown in the remaining four graphs of Fig. 15a. Figures 15b - e give similar results for $\gamma = 2$, 2.5, 4, and 6. To illustrate the effect of K, another calculation was done, at $\gamma = 4$, with $K = 1.0$, and $\alpha = 1$. The results, given in Fig. 16, differ from those found for $K = 10$ chiefly by the fact that τ is somewhat smaller, and N is closer to 2/5. This trend is qualitatively what would be expected; a larger value of K strengthens the influence of the pressure gradient in drawing material laterally away from the axis of symmetry. The fact that more fluid is being extracted in this direction acts to retard the shock motion, i.e., N is decreased.

5. <u>Comparison with the Symmetric Solution.</u> The values of N found in the above calculations were in all cases quite close to the value 2/5 that applies for the symmetric, constant-energy solution. Furthermore, the quantity τ does not attain an appreciable value until some distance away from $\eta = 1$, where the density has fallen to a low value. Thus we might expect that, near

the shock at least, the asymmetric solutions will not differ greatly from the constant-energy solution. This is indeed the case. Figure 17, which compares the symmetric and centerline solutions for $\gamma = 3$, shows that, along the centerline at least, the motion of most of the mass involved is well approximated by the solution for $N = 2/5$. One may expect this trend to persist even for θ greater than zero, suggesting that the Taylor solution will in general be an excellent approximation to the considerably-more-complicated asymmetric solution. The comparison shown in this figure is typical of the results found at other values of γ. This close similarity between the two solutions forms the justification for our use of the simpler constant-energy solution in making crater predictions.

Furthermore, this close similarity appears to be a general feature. Admittedly, the evidence for this conclusion comes from a limited number of cases, in which a special pressure variation was used. Nonetheless, it is difficult to imagine how the true distribution of $\Upsilon(\eta)$ could be radically different from that used here. The function $\Upsilon(\eta)$ must always be zero at the shock, and must rise to a value comparable to the value of ϕ near the sonic point, i. e., it must be of unit order. Future research in this area should examine other approximations for Υ, but it is considered highly unlikely that any contrary evidence will be found.

So far as blast-wave theory is concerned, then, the energy of the projectile plays the dominant role, its momentum being only of secondary importance. One plausible physical explanation[*] is based on the experimental

---

[*] This explanation was suggested to the authors by Mr. Robert J. Vidal of this Laboratory

observation(22) that targets struck by hypervelocity projectiles often acquire momenta many times that of the projectile, implying that the material ejected from the target must also carry several times the projectile momentum. Thus it appears that the momentum of the projectile itself makes only a minor contribution to the over-all conservation process.

A corollary of this conclusion is that the conditions of hypervelocity impact can be simulated* by any experiment which duplicates the energy of the incident particle, irrespective of whether its momentum is correctly matched. In particular, any intense source of short-pulse electromagnetic radiation, such as the output of some currently available lasers, should be capable of providing such a simulation. Such an experimental technique appears to hold promise, and Appendix B discusses the basis for it in some detail.

A final point must be made concerning the importance of energy versus momentum. One must not infer, from our use of a constant-energy solution, that "energy scaling" will hold, in the sense that crater volume is proportional to the projectile's kinetic energy over a range of impact speeds. The fact is that this theory predicts a result more nearly of the form $R_c \backsim V^{1/3}$, due to the fact that γ is allowed to vary with impact speed in an effort to fit the equation of state over the whole range. And equally important, the penetration law $R_c \backsim V^{1/3}$, sometimes described as "momentum scaling", does

---

[*] The fact that such a simulation is possible was first pointed out to the authors by Dr. Franklin K. Moore.

not imply that the projectile momentum is a controlling parameter. The theory presented here is derived from an analysis in which energy and momentum can both be conserved. Because the shock wave is such a strong agent in affecting the motion of the fluid particles, and because the low pressure region is, by comparison, so weak in this regard, the flow of the greater portion of the mass involved takes place as though it were caused by a spherically-symmetric disturbance. Given this fact, only the total energy need be considered.

6. Isolation of the Sonic Point. This subsection describes the analytic means that are used to determine the exact location of the sonic point and to provide a valid solution at that point. In doing so, it is useful to work with the variables

$$x = \frac{N\phi}{\eta}, \quad y = \frac{N^2}{\eta^2}\,\frac{\gamma f}{\psi}, \quad z = \frac{N\tau}{\eta} \tag{97}$$

In terms of these variables, Eqs. (80), (87), (88), and (94) become (see Appendix A for details of the derivation)

$$\frac{x-N}{y}\,\frac{dy}{dx} = -(\gamma-1) + \frac{\left[(x-N)^2 - y\right]\left[2-(\gamma-1)z-(3\gamma-1)x\right]}{y\left(3x+z-\frac{2}{\gamma}\left[1-N\right]\right) - x(x-N)(x-1)} \tag{98}$$

$$\eta\,\frac{dx}{d\eta} = \frac{y\left(3x+z-\frac{2}{\gamma}\left[1-N\right]\right) - x\,(x-N)(x-1)}{(x-N)^2 - y} \tag{99}$$

$$\eta\,\frac{dz}{d\eta} = \frac{z - \frac{1}{2}z^2 - 2xz - \frac{2N^2}{\psi\,\eta^2}\,\frac{\partial^2 f}{\partial\theta^2}\,(\eta,0)}{x-N} \tag{100}$$

$$(x-N)\frac{\eta}{\psi}\frac{d\psi}{d\eta} = -\eta\frac{dx}{d\eta} - 3x - z \tag{101}$$

The vanishing of the denominator is now given by

$$(x-N)^2 - y = \frac{N^2}{\eta^2}\left[(\phi-\eta)^2 - \frac{\gamma f}{\psi}\right] = 0 \tag{102}$$

When this occurs, inspection of Eq. (99) shows that the solution will be single-valued only if

$$y\left(3x+z-\frac{2}{\gamma}[1-N]\right) - x(x-N)(x-1) = 0 \tag{103}$$

at the same point. If (102) and (103) are both true at the same point, then (103) may be simplified to read

$$(x-N)\left\{3x+z-\frac{2}{\gamma}[1-N]\right\} - x(x-1) = 0 \tag{104}$$

which a little algebra will show to be equivalent to the condition that the function $H(\eta)$, defined in Eq. (96), be zero. At the sonic point, where (102) and (103) are both true, the derivatives in Eqs. (98), (99), and (101) become indeterminate. The manipulations required to resolve this indeterminacy are given in Appendix C. There it is shown that the slopes at the sonic point (designated by an asterisk) are given by

$$\left.\frac{dy}{dx}\right)^* = k_1, \qquad \left.\frac{dz}{dx}\right)^* = k_2 \tag{105}$$

where k_1 is a solution of the quadratic

$$Ak_1^2 + Bk_1 + C = 0 \tag{106}$$

and where

$$k_2 = \left\{(\gamma-1)+\frac{k_1}{x^*-N}\right\}\frac{z^*\left(1-\frac{1}{2}z^*-x^*\right)-2\left(\frac{N^2}{\eta^2}\frac{1}{\psi}\frac{\partial^2 f}{\partial\theta^2}(\eta,0)\right)^*}{(x^*-N)\left[2-(\gamma-1)z^*-(3\gamma-1)x^*\right]} \tag{107}$$

The functions A, B, and C appearing here are defined in Appendix C. They depend on the sonic-point values of x, y, z, η, ψ, f, ϕ, and τ, in addition to their dependence on N and γ. Having found k_1 and k_2, the formulas presented in Appendix C permit one to find $\left.dx/d\eta\right)^*$, $\left.\psi'\right)^*$, $\left.\phi'\right)^*$, $\left.\tau'\right)^*$, and $\left.f'\right)^*$, and with these, the solution can be continued smoothly through the sonic point. All that is required is the list of sonic-point values referred to above. These can be found by extrapolating from a set of solutions, at various values of N, which approach more and more closely to the sonic point. The procedure is illustrated in Fig. 18; here are shown, in the x, y plane, some of the numerical solutions obtained for the case $\gamma = 3$, with $K = 10$, $a = 1$. The line marked "numerator = 0" is the locus of points at which Eq. (103) is satisfied, while that marked "denominator = 0" is the locus of points satisfying (102). By extrapolating these two loci, one may isolate the values x^* and y^* at which these two conditions are fulfilled simultaneously. Similar extrapolations permit a determination of z^*, η^*, ψ^*, f^*, ϕ^*, and τ^*. These, in turn, fix the values of all the slopes, so that the solution in the neighborhood of the singularity is complete. The pair of separatrices shown in Fig. 18 was found by just this method.

Even with the solution determined in this fashion, there still remains some question as to the precise value of N to be identified with it. For practical application, there seems to be no point in specifying N to five- or six-figure accuracy. Thus, in carrying over results from the very fine scale of Fig. 18 to the "practical" scale of Fig. 15a, the whole solution is tagged with the number $N = 0.375$. In actual fact, the solution shown in Fig. 1 consists of the solution common to 0.37500 and 0.37501 for $x > 0.055$, plus the extrapolation through the sonic point.

7. <u>One-Dimensional Solution.</u> The remainder of this section presents a treatment of the disturbance field behind a strong planar blast wave. Because only one spatial dimension is present, a complete solution can be worked out. This solution illustrates a method for simultaneous energy and momentum conservation in a self-similar solution. In addition, the formulas which are derive can be used to predict the craters that will be formed by the planar impact of slab-or disk-shaped projectiles.

We make the perfect-gas approximation from the outset, choosing the value of γ in each case according to the method outlined above. The problem is to determine the motion of a half-space of material resulting from the impulsive application of a large pressure to its free surface, which is then exposed to a perfect vacuum. The large impulsive pressure may be imagined to arise in various ways, for example by the detonation of an explosive at the free surface, or by the face-on impact of a disk-or slab-shaped projectile:

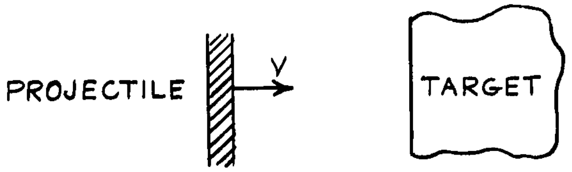

In the ensuing motion, a strong shock wave propagates into the target, while the free surface expands rapidly into the vacuum on the left

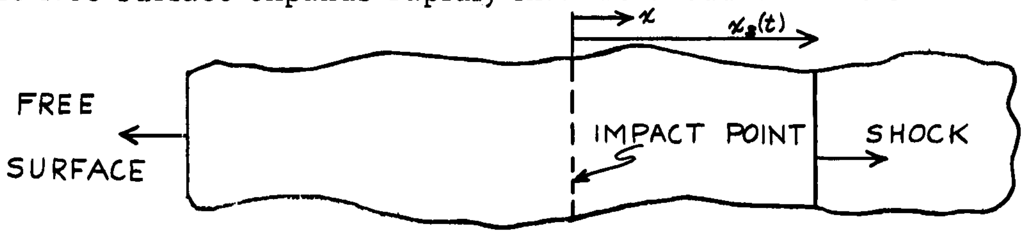

We may expect that a blast-wave solution will correctly describe the motion when the time after impact is large compared to the time during which the impulsive pressure was applied. Thus the free surface will lie, effectively, at $x = -\infty$. The blast-wave solution of this problem has been discussed by a large number of authors.(23)-(27) An excellent review of these is given by Mirels.(28)

The equations of motion are

$$\frac{\partial \rho}{\partial t} + \frac{\partial}{\partial x}(\rho u) = 0 \tag{108}$$

$$\frac{\partial u}{\partial t} + u\,\frac{\partial \rho}{\partial x} + \frac{1}{\rho}\,\frac{\partial p}{\partial x} = 0 \tag{109}$$

$$\left\{\frac{\partial}{\partial t} + u\,\frac{\partial}{\partial x}\right\}\left(\frac{p}{\rho^{\gamma}}\right) = 0 \tag{110}$$

In a self-similar solution, the dependent variables are assumed to depend only on the similarity coordinate

$$\eta = \frac{x}{x_s(t)} \tag{111}$$

and are made dimensionless by the definitions

$$u = \dot{x}_s\,\phi(\eta) \qquad \rho = \rho_0\,\psi(\eta) \qquad p = \rho_0\,\dot{x}_s^{\,2}\,f(\eta) \tag{112}$$

As before, all time dependence is eliminated from the differential equations if the shock advances as a power of the time

$$x_s = A t^N \tag{113}$$

Thus the similarity equations become

$$(\phi - \eta)\,\psi' + \phi'\psi = 0 \tag{114}$$

$$(\phi-\eta)\,\phi' - \frac{1-N}{N}\,\phi + \frac{f'}{\psi} = 0 \qquad (115)$$

$$-2\,\frac{1-N}{N}\,f + (\phi-\eta)f' - \frac{\gamma f}{\psi}(\phi-\eta)\,\psi' = 0 \qquad (116)$$

Solved for the derivatives, these become

$$\phi' = -\frac{1-N}{N}\;\frac{\frac{2f}{\psi} - \phi(\phi-\eta)}{(\phi-\eta)^2 - \frac{\gamma f}{\psi}} \qquad (117)$$

$$\psi' = -\frac{1-N}{N}\;\frac{(\phi-\eta)\,\psi\,\phi - 2f}{(\phi-\eta)\left\{(\phi-\eta)^2 - \frac{\gamma f}{\psi}\right\}} \qquad (118)$$

$$f' = -\frac{1-N}{N}\,f\;\frac{\gamma\phi - 2(\phi-\eta)}{(\phi-\eta)^2 - \frac{\gamma f}{\psi}} \qquad (119)$$

with the usual boundary conditions at the shock

$$\phi(1) = f(1) = \frac{2}{\gamma+1}\;;\quad \psi(1) = \frac{\gamma+1}{\gamma-1} \qquad (120)$$

8. Determination of N. Before Eqs. (117) - (119) can be integrated, the parameter N must be specified. Just as in the axisymmetric case, the criterion that determines N is that the solution pass smoothly through the sonic point. The values of N that accomplish this feat have been reported in the literature for several values of γ, and a few more were calculated in the present effort. These results are summarized in Table II, and are plotted in Fig. 19 for γ between 1.0 and 10. The distributions of pressure, density and velocity that are obtained in this type of solution are shown in Fig. 20 for the case $\gamma = 7/5$, which has the exact solution(23), (27)

$$\psi = 6(5-4\eta)^{-5/2},\quad \phi = \frac{5}{6}(2\eta-1),\quad f = \frac{5}{6}(5-4\eta)^{-3/2} \qquad (121)$$

In further analogy to the axisymmetric case, the values of N which permit a smooth crossing of the sonic point are different from those corresponding to conservation of the total energy or momentum (per unit area in the plane of the target surface). Denoting these respectively by $\mathcal{E}$ and $\mathcal{P}$, the appropriate integrals are

$$\mathcal{E} = \int_{-\infty}^{x_s} \left(\frac{p}{\gamma-1} + \frac{1}{2}\rho u^2\right) dx = \rho_0 x_s \dot{x}_s^2 \int_{-\infty}^{1} \left(\frac{f}{\gamma-1} + \frac{1}{2}\psi\phi^2\right) d\eta \qquad (122)$$

$$\mathcal{P} = \int_{-\infty}^{x_s} \rho u \, dx = \rho_0 x_s \dot{x}_s \int_{-\infty}^{1} \psi \phi \, d\eta \qquad (123)$$

Because $x \backsim t^N$, the energy integral will be independent of time only if N = 2/3, while the momentum integral requires N = 1/2. Neither of these values, however, leads to a physically acceptable solution. Instead, the solution for N = 2/3 is symmetric about $x = 0$, while that for N = 1/2 becomes double-valued. The solution passing through the sonic point is the only one that starts at the shock, and yields a velocity distribution like that of Fig. 20, in which material moves rapidly to the left at large negative values of η .

The values of N corresponding to constant energy and constant momentum are compared with the curve of N(γ) in Fig. 19. It should be noted that for γ in the range from 2.0 to 10, N(γ) is relatively constant, at a value not much different from the value that holds for constant energy. As a corollary of this, we find once again that the constant-energy distributions of pressure, density and velocity are very nearly the same as those having the smooth sonic-line crossing. Figure 20 illustrates this point for the case γ = 1.4. (The constant-energy solution used here is described in detail below.) The close identity between these two types of solution is exactly the same behavior as found above in our approximate treatment of the centerline equations. The fact that the one-dimensional results are found without approximation (there is no term analogous to τ) may be taken as evidence for the generality of the conclusions reached in the axisymmetric case.

9. Simultaneous Conservation of Energy and Momentum. There can hardly be any question about the fact that the solutions which cross the sonic line smoothly are the only acceptable ones. Having chosen N so as to achieve such a smooth crossing, however, it is now impossible to satisfy either of the conservation conditions, in the form given by Eqs. (122) and (123). One means of resolving this difficulty is pointed out by Zeldovich.[25] He suggests that a small portion of the mass be ignored in calculating the total energy and momentum. This small mass, which originally lies at the free surface and is strongly compressed during the initial stages of the impact, acquires an entropy during the impact phase which is different from that predicted by the similarity solution. This entropy depends only on conditions at the shock, through integration of the differential equations, and has nothing to do with the details of how the shock was formed. The entropy of each particle remains constant, once it has been processed by the shock. Thus the small portion of mass processed during the impact phase always bears the imprint, so to speak, of this phase, and its motion is never correctly given by the similarity solution. Zeldovich's argument is that in seeking a self-similar solution, one should consider only that mass whose motion is expected to be properly described by such a solution. His argument derives considerable support from the fact that non-similar numerical

solutions$^{(27)}$ of the partial differential equations in x and t fair smoothly into his similarity solution when the time is large compared to the duration of the impulsive pressure.

Mathematically speaking, the exclusion of this mass corresponds to the replacement of the infinite lower limit in Eqs. (122) and (123) by a finite number $-x_0(t)$. The introduction of a second free parameter permits two conservation conditions to be satisfied. In the remainder of this section, we work out in detail the relations that follow from neglecting this small amount of mass.

The point $-x_0(t)$ $(x_0 > 0)$, which forms the boundary of the neglected mass, will be far to the left of the origin, since the mass neglected is small. As a prelude to modifying the conservation integrals, then, we must first determine the asymptotic form of the solution at large negative values of η .

The key to finding such an asymptotic solution is to neglect the pressure-gradient terms in the momentum equation, Eq. (115). We have seen before that in these solutions the particle velocity is large at large negative η , with a slope of order one. The pressure, on the other hand, is approaching zero, signifying that its derivative is also becoming extremely small. Neglecting this term yields the simple solution

$$\phi \approx \frac{\eta}{N} \tag{124}$$

With ϕ known, the density ψ can now be found from Eq. (114) as

$$\psi \approx A_1 \left|\eta\right|^{-\frac{1}{1-N}} \tag{125}$$

Finally, use of ϕ and ψ in (116) gives the asymptotic pressure formula

$$f \approx A_2 \left|\eta\right|^{2-\frac{\gamma}{1-N}} \tag{126}$$

Substituting back into Eqs. (114)-(116) shows that these approximations are internally consistent.

The constants A_1 and A_2 are not independent. Lees and Kubota,(29) among others, have shown that the similarity equations in general have the solution

$$\psi^{\gamma-2\frac{1-N}{N}} \quad |\phi-\eta|^{-2\frac{1-N}{N}} = K_1 f \tag{127}$$

where, from conditions at $\eta = 1$, K_1 is found to be

$$K_1 = \frac{(\gamma+1)^{\gamma+1}}{2(\gamma-1)^{\gamma}} \tag{128}$$

Equation (127) is derived by dividing (114) by $\psi(\phi-\eta)\Big/\frac{2(N-1)}{N}$, and by subtracting from this the result of dividing (116) by $f(\phi-\eta)$. The relationship between A_1 and A_2 is found by substituting the asymptotic pressure and density solutions into the general integral, Eq. (127). One finds that

$$A_2 = \frac{A_1^{\gamma}}{K_1\left\{\frac{A(1-N)}{N}\right\}^{\frac{2(1-N)}{N}}} \tag{129}$$

The quantity A_1 is found by integrating the similarity equations out to a large negative value of η , where the asymptotic behavior is reached. For example, in the case $\gamma = 1.4$, the exact solution given in Eq. (121) shows that $A_1 = 3/16$. In general, A_1 depends on γ .

If we now neglect a small amount of mass m_0 (mass per unit area), we have

$$m_0 = \int_{-\infty}^{-x_0(t)} \rho\, dx = \rho_0 x_s \int_{-\infty}^{\eta_0} \psi\, d\eta = \rho_0 A t^N \int_{-\infty}^{\eta_0} \psi\, d\eta \tag{130}$$

The integral here can be evaluated directly. By writing the continuity equation in the form

$$\frac{d}{d\eta}(\phi\,\psi) = \eta\,\psi' \tag{131}$$

and integrating by parts, we find in general that

$$\int_a^b \psi\, d\eta = -\left[\psi\,(\phi - \eta)\right]_a^b \tag{132}$$

Thus

$$\int_{-\infty}^{\eta_0} \psi\, d\eta = -\left[(\phi-\eta)\,\psi\right]_{\eta=\eta_0} = \frac{1-N}{N}\, A_1 \left|\eta_0\right|^{1-\frac{1}{1-N}} \tag{133}$$

and

$$m_0 = \rho_0 A\, t^N\, \frac{1-N}{N}\, A_1 \left|\eta_0\right|^{1-\frac{1}{1-N}} \tag{134}$$

In order to make m_0 independent of time, we must choose

$$\eta_0 = -K_2\, t^{1-N} \qquad K_2 > 0 \tag{135}$$

which gives

$$m_0 = A\, A_1\, K_2^{-\frac{N}{1-N}}\, \frac{1-N}{N}\, \rho_0 \tag{136}$$

The parameter K_2 is the second free parameter which, with A, will permit two conservation conditions to be satisifed.

If we neglect the mass m_0 in the energy-conservation integral, we have

$$\mathcal{E} = \rho_0\, x_s\, \dot{x}_s^{\,2} \int_{\eta_0}^{1} \left(\frac{f}{\gamma-1} + \frac{1}{2}\,\psi\,\phi^2\right) d\eta \tag{137}$$

This integral, evaluated at the upper limit, yields a constant. At the lower limit, we may use the asymptotic solution. Doing so reveals that the internal energy contribution is negligible compared with the kinetic energy term, and we have

$$\mathcal{E} = \rho_0 A t^N A^2 N^2 t^{2N-2} \left\{ \left[\int \frac{A_1}{2N^2} |\eta|^{2-\frac{1}{1-N}} d\eta \right]_{\eta=\eta_0} + \text{const.} + O\left(|\eta_0|^{3-\frac{\gamma}{1-N}} \right) \right\} \tag{138}$$

The second term in the curly brackets comes from the upper limit, the third term from the internal energy. Carrying out the integration gives

$$\mathcal{E} = \rho_0 \frac{A^3}{2} t^{-(2-3N)} \left\{ A_1 \frac{|\eta_0|^{3-\frac{1}{1-N}}}{3-\frac{1}{1-N}} + \text{const.} + O\left(|\eta_0|^{3-\frac{1}{1-N}} \right) \right\}$$

$$= \rho_0 \frac{A^3}{2} t^{-(2-3N)} \left\{ A_1 \frac{1-N}{2-3N} K_2^{3-\frac{1}{1-N}} t^{2-3N} + \text{const.} + O\left(t^{3-\gamma-3N} \right) \right\} \tag{139}$$

$$= \rho_0 A^3 \frac{A_1}{2} \frac{1-N}{2-3N} K_2^{\frac{2-3N}{1-N}} \left\{ 1 + O\left(t^{-[2-3N]} \right) + O\left(t^{-[\gamma-1]} \right) \right\}$$

as t becomes large (this is the limit at which we expect the blast-wave solution to hold), the second and third terms here become negligible, since N is less than 2/3, and γ greater than one.

Neglecting the same amount of mass in the momentum integral gives

$$\mathcal{P} = \rho_0 x_s \dot{x}_s \int_{\eta_0}^{1} \psi \phi \, d\eta \tag{140}$$

This integral can be evaluated exactly. Re-writing Eq. (115) as

$$\psi (\phi - \eta) \phi' - \frac{1-N}{N} \psi \phi + f' = 0 \tag{141}$$

and integrating, we have

$$-\frac{1-N}{N}\int_a^b \psi\,\phi\,d\eta + f\Big]_a^b + \int_a^b \psi(\phi-\eta)\,\phi'\,d\eta = 0 \tag{142}$$

Consider only the last term. We've already seen in Eq. (132) that

$$\frac{d}{d\eta}(\phi-\eta)\,\psi = -\psi \tag{143}$$

An integration by parts gives

$$\int_a^b \psi\,(\phi-\eta)\,\phi'\,d\eta = \psi(\phi-\eta)\phi\Big]_a^b + \int_a^b \psi\,\phi\,d\eta \tag{144}$$

Substituting this in (142) gives the desired result

$$\left(2-\frac{1}{N}\right)\int_{\eta_0}^{1}\psi\,\phi\,d\eta = -\big[f\big]_{\eta_0}^{1} - \big[\phi\,(\phi-\eta)\,\psi\big]_a^b \tag{145}$$

The right-hand side is found to be zero at the upper limit, and at the lower limit, the pressure contribution is small compared with the second term. Thus

$$\int_{\eta_0}^{1} \psi\,\phi\,d\eta = \frac{A_1}{N}\,\frac{1-N}{2N-1}\,|\eta_0|^{2-\frac{1}{1-N}} \tag{146}$$

As $|\eta_0| \rightarrow \infty$, the integral vanishes. Thus, if we were to include all the mass, and describe its motion by the self-similar solution, we would find zero net momentum. In fact, Zeldovich takes this point of view, and apparently considers the solution valid only for such a momentum condition. However, it would appear to be more consistent to neglect mass in the momentum integral as well. Doing so, we have

$$P = \rho_0\, x_s\, \dot{x}_s \int_{\eta_0}^{1} \psi\,\eta\,d\eta = \rho_0 A t^N N A t^{N-1}\,\frac{A_1(1-N)}{N(2N-1)}\,K_2^{\frac{1-2N}{1-N}}\,t^{1-2N} \tag{147}$$

$$= \rho_0 A^2 A_1\,\frac{1-N}{2N-1}\,K_2^{\frac{1-2N}{1-N}}$$

This relation, together with (139), enables us to find A and K_2 in terms of $\mathcal{E}$ and $\mathcal{P}$. Note that the velocity of the impacting slab is related to these parameters by

$$\frac{2\mathcal{E}}{\mathcal{P}} = \frac{2N-1}{2-3N} A K_2 \tag{148}$$

while the neglected mass is of the same order as that of the projectile

$$\frac{\mathcal{P}^2}{2\mathcal{E}} = \rho_0 A A_1 \frac{(1-N)(2-3N)}{(2N-1)^2} K_2^{-\frac{N}{1-N}} = \frac{N(2-3N)}{(2N-1)^2} m_0 \tag{149}$$

Solving for A and K_2 in terms of $\mathcal{E}$ and $\mathcal{P}$ gives

$$K_2 = \left\{ \frac{4A_1(1-N)(2-3N)^2}{(2N-1)^3} \quad \frac{\mathcal{E}^2 \rho_0}{\mathcal{P}^3} \right\}^{1-N} \tag{150}$$

$$A = G(\gamma) \frac{\mathcal{P}^2}{\rho_0 \mathcal{E}} \left(\frac{\rho_0 \mathcal{E}^2}{\mathcal{P}^3} \right)^N \tag{151}$$

where

$$G(\gamma) = \frac{2(2-3N)}{2N-1} \left\{ \frac{(2N-1)^3}{4A_1(1-N)(2-3N)^2} \right\}^{1-N} \tag{152}$$

The actual solutions of the similarity equations have never been reported, except for $\gamma = 1.4$. Thus the variation of A with γ is not presently known. When this information becomes available, it will be possible to compare the final formula for the shock propagation

$$x_s(t) = G(\gamma)\,\frac{\mathcal{P}^2}{\rho_0\,\mathcal{E}}\,\left(\frac{t}{\mathcal{P}^3/\rho_0\,\mathcal{E}^2}\right)^N \qquad (153)$$

with the one-dimensional constant-energy result

$$x_s(t) = \left(\frac{9}{4\,I_0(\gamma)}\,\frac{\mathcal{E}\,t^2}{\rho_0}\right)^{1/3} \qquad (154)$$

Figure 21 shows the function $I_0(\gamma)$, found by a hand computation using the exact solution which is given, for example, in Ref. 6. The constant-energy distributions of pressure, velocity, and density are compared with the asymmetric result in Fig. 20 for $\gamma = 1.4$.

The "craters" corresponding to these shock-wave time-histories may be found as the shock depth at the instant when the pressure behind the shock has decayed to the level $\mathbb{P}$. Denoting this quantity by x_{c_1}, a little algebra gives, for the asymmetric solution

$$x_c = \frac{G(\gamma)\,\mathcal{P}^2}{\rho_0\,\mathcal{E}}\left\{\frac{2N^2G^2}{\gamma+1}\,\frac{\rho_0\,\mathcal{E}^2}{\mathcal{P}^2\,\mathbb{P}}\right\}^{\frac{N}{2(1-N)}} \qquad (155)$$

and for the one-dimensional, constant-energy solution

$$x_c = \frac{2}{(\gamma+1)\,I_0(\gamma)}\,\frac{\mathcal{E}}{\mathbb{P}} \qquad (156)$$

The method described above can be applied, with analogous results, to the axisymmetric case. Far from the impact point, we may imagine that the flow is confined within a cone for which $\theta \approx \pi$

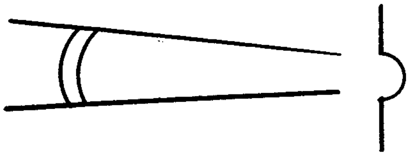

Within this cone, all quantities have a negligible variation with θ , and the velocity component ω is small compared with ϕ . The problem is then essentially the same as that treated above, and the same series of steps can be taken. The only new term present in the axisymmetric case is the term $2\phi/\eta$ in the continuity equation, which merely has the effect of changing certain exponents. The conclusion remains the same, namely that simultaneous conservation of energy and momentum can be achieved by neglecting a small amount of mass.

II. BOUNDARIES FOR APPLICATION OF THE BLAST WAVE ANALYSIS

A. The Space Vehicle Environment

The probability of collisions between space vehicles and meteoroids of sufficient size to cause serious damage is too small and too variable to allow convenient verification of empirical relationships by satellite experiments. Therefore, it is necessary to improve prediction methods as much as possible. Diverse sources of evidence can be used. Among these sources are theoretical analyses, hypervelocity impact experiments, studies of meteors, meteorites, meteor craters, and impacts of smaller meteoroids on satellites, etc. A survey of information pertinent to this problem has been published by Davison and Winslow.(31)

There is little agreement concerning the properties of the impacting particles. Density estimates and assumptions range from 0.05 gm/cm^3 (32, 33) to 7.8 gm/cm^3.(34) Dense meteoroids are assumed to be of asteroidal origin and low density meteoroids are assumed to come from comets. Whipple(35) indicates that in space about 10% of sporadic meteoroids and not more than 20% of all meteoroids are of asteroidal origin. Of the meteoroids observed in the vicinity of the earth about 50% are sporadic and 50% are in streams. Relative velocities range up to 80 kilometers per second (assuming a particle in a closed orbit about the sun moving at 42 kilometers per second approaching the earth in a direction opposite to the earth's motion at 30 kilometers per second, and colliding with a satellite moving at approximately 8 kilometers per second around the earth).

Whipple(32) states that the average velocity of photographic meteoroids is 28 km/sec. The average velocity of smaller meteoroids is less.(36) Whipple(32) chooses a velocity of 15 km/sec for the smallest meteoroids and assumes an arbitrary variation of velocity with magnitude. The fainter meteoroids and those detected by radar observations tend to be more sporadic than the brighter meteoroids.(35) The mass of individual meteoroids has been determined from brightness measurements on the Harvard Photographic Meteor Program. Meteors of visual magnitude zero were found to have masses of the order of 25 grams. Based upon previous rough estimates(32) of the penetration of meteoroids through structural materials, the mass range of interest is from about 10^{-2} to 10^{-4} grams. Conversion of visual magnitude to estimated mass is accomplished by the following formula(34)

$$M = 2.5 \log_{10} \frac{m_0}{m}$$

in which M is the magnitude

m_0 is the mass of a zero magnitude meteor

and m is the mass of the meteor

Photographic techniques are used for meteoroids down to the 5th magnitude. The use of radio echo techniques may be extended to the 12th magnitude.(32) A comparison with these mass estimates indicates that the most direct evidence of interest for this penetration problem will come from radio echo measurements.

In a study of photographic meteor wakes and trains McCrosky(37) found that the particles which break off to cause the wake, have masses of 10^{-5} or 10^{-6} grams. This evidence of the mode of fragmentation and the size of fragments making up the larger meteoroids lends additional weight to Whipple's suggestion that most of the meteoroids are low density bodies.

The original estimates of the density of photographic meteoroids have been revised upward recently.(38) On the basis of new estimates of luminous efficiency a one gram meteoroid having a velocity of 30 km/sec. has a density of 0.44 gm/cm^3. These estimates result from experiments in which particles of known properties were projected down through the atmosphere and simultaneously photographed from the earth.

B. Energy Transformation During Impact

An attempt has been made to present the hypervelocity impact problem as a chronological sequence of events involving realistic solids. This approach leads to consequences that are difficult to unify in mathematical terms but which, it is hoped, will give some insight into the nature of impact processes.

During the brief period of meteoroid impact there are several stages of energy transformation. It is important to consider the time history of these stages because target characteristics will partially determine which stage predominates in the production of damage to the space vehicle. Both the meteoroid and the target may undergo polymorphic phase changes, however, the time occurrence of such phase transitions will not be simultaneous unless the materials involved are identical. It is extremely unlikely that the meteoroid will be identical in mechanical properties with the satellite target materials.

Table 3 lists the stages of energy transformation undergone by the meteoroid-target interface under hypervelocity impact conditions. Every impact will not necessarily involve each of the listed steps since the impact kinetic energy varies over a very wide range.

The temperatures attained in satellite materials during impact are important for several reasons. The temperature attained is a measure of the energy absorbed into thermal motion. It also affects the assumption of fluid properties in the blast wave analysis and the ejection of material from the cavity in the final stages of the impact process during which one would expect that fluids would be lost from the cavity but solids would be retained.

Solids may be heated or cooled by impact. The dominant factor affecting the sign of the temperature change is the Grüneisen factor (Γ_j). The Grüneisen factor for the jth mode of a particular lattice vibration is

$$\Gamma_j = -\frac{\partial \ln \nu_j}{\partial \ln V}$$

so that Γ_j is a measure of the change in lattice vibration frequency for a given change in volume. The role of the Grüneisen factor in the equation of state of solids is indicated by Slater(39) in a derivation based upon the statistical mechanics of a system of oscillators. The equation for the pressure is

$$p = p_0 + \frac{1}{V}\sum_j \Gamma_j \frac{h\nu_j}{e^{\frac{h\nu_j}{kT-1}}}$$

in which the first term on the right is the pressure at absolute zero and the summation is the so-called thermal pressure. h is Planck's constant and k is the Boltzmann constant.

The role of the Grüneisen factor has also been indicated by Eastabrook(40) starting with an equation derived using the Euler reciprocity relation

$$\left(\frac{\partial p}{\partial T}\right)_V = \left(\frac{\partial S}{\partial V}\right)_T$$

in which T is the absolute temperature and S is the entropy. This may be rewritten using Maxwell's relations

$$-\left(\frac{\partial p}{\partial V}\right)_T \left(\frac{\partial V}{\partial T}\right)_p = -\left(\frac{\partial S}{\partial T}\right)_V \left(\frac{\partial T}{\partial V}\right)_s$$

so that

$$\Gamma = \frac{\alpha_V \, V \, K_T}{C_V} \qquad (157)$$

in which α_V is the volume coefficient of thermal expansion = $\left(\frac{1}{V}\,\frac{\partial V}{\partial T}\right)_p$

K_T is the isothermal bulk modulus = $-V\left(\frac{\partial p}{\partial V}\right)_T$

and C_V is the heat capacity at constant volume = $T\left(\frac{\partial S}{\partial T}\right)_V$

$\Gamma\left(= -\frac{V}{T}\left(\frac{\partial T}{\partial V}\right)_s\right)$ is the Grüneisen "constant" which is an average of the Γ_j's taken in a way so that the equation is satisfied. Since the various Γ_j's may be either positive or negative, wide variations in the values of Γ necessary to satisfy Eq. (157) are observed. The factors C_V, V and K_T are positive quantities, so that Γ will be negative when the volume thermal expansion coefficient is negative. Some materials have negative values of thermal expansion coefficient, at least over part of the temperature range for which these measurements have been made. Among these materials are vitreous silica (SiO_2), silicon, germanium, diamond (C), indium antimonide (InSb), several lithium aluminum silicates and uranium pyrophosphate (UP_2O_7). The thermal expansion coefficient of uranium pyrophosphate is of special interest because it is negative at high temperatures.

Temperatures during impact have been calculated by several investigators. Wide variations in temperature are found depending upon material properties. The calculations by Walsh et al(11) of temperature rise along an adiabat are obtained by integrating the equation

$$\int_{T_i}^{T} \frac{dT}{T} = -\int_{V_i}^{V} \frac{\Gamma(V)\,dV}{V}$$

This calculation depends upon knowledge of the process and an estimate of the volume dependence of Γ .

Benedek's$^{(41)}$ temperature calculations depend upon knowledge of the volume dependence of the cohesive energy.$^{(42)}$ The equation used is

$$V(\mu) - V(0) = E(\mu) - E(0) - \Phi(\mu) - \Phi(0)$$

in which

$$E(\mu) - E(0) = \frac{\frac{1}{2}C^2\mu^2}{(1-S\mu)^2}$$

and μ = volume compression

V = vibrational energy

E = total internal energy

Φ = cohesive energy

and C and S are the constants in the equation

$u_s = C + S u_1$ for the shock and particle velocities

Knowing the vibrational energy, the temperature is calculated by use of the Debye approximation for the specific heat.

Wackerle's$^{(43)}$ calculations are based upon the following formula:

$$T_H = T_0\, e^{\Gamma_0 \mu} + \left(\frac{\Gamma}{2C_V}\right) e^{\Gamma_0 \mu} \int_0^{\mu} e^{-\Gamma_0 \mu} \left[\mu\left(\frac{\partial P}{\partial \mu}\right) - P\right] d\mu$$

in which Γ_0 is Γ evaluated from the STP values of α_V , C_P and adiabatic bulk sound speed,and T_0 and T_H are the initial and final temperatures along the Hugoniot. The results of the calculations described above indicate roughly the expected dependence upon thermal expansion coefficient and Γ ; that is, the low expansion materials show, initially at least, smaller temperature changes than high expansion materials. The calculated temperature rise of vitreous silica is only 5°C at impact pressures up to 262 kilobars.

It is evident that the space vehicle designer can have a degree of control over the temperatures attained during impact. In regions in which it is desirable to absorb the maximum amount of energy in thermal vibrations, the choice of materials with high Γ is indicated. In regions in which it is desirable to prevent melting in order to keep material in the crater after impact one would choose materials with low values of Γ . Therefore, one expected feature of these configurations is a sandwich structure with the high Γ material on the outside and low Γ material on the inside.

C. Stress Wave Velocities in Solids

1. Elastic Stress Waves. At low velocities the impact of a small particle upon the outer (extended) surface of a satellite will introduce a stress wave in the target which involves the dilatational wave velocity given by

$$C_1 = \left[\frac{Y(1-\nu)}{\rho(1+\nu)(1-2\nu)}\right]^{1/2} \tag{158}$$

where Y = Young's modulus

ν = Poisson's ratio

Note that the bulk compressional wave velocity (Eq. (158)) is significantly different from the compressional wave velocity found in a long thin bar$^{(44)}$

(i.e., where the bar cross section is small compared with a wave length). The change in velocity which occurs as the wavelength approaches the cross-sectional dimension is due to the increase in lateral restraints. For the high frequencies associated with short duration meteoroid impact, the higher dilatational wave velocity is more appropriate. In isotropic solids, Poisson's ratio is always less than one-half and greater than zero, hence $C_1 \geq C_0$ (the velocity in a long thin bar).

For isotropic solids, the fastest elastic wave travels with the bulk dilatational wave velocity. Hence, meteoroid impact will be in the hyper-velocity region if the impact velocity is greater than the fastest elastic wave velocity in the target material given by Eq. (158).

In Table 4, the bulk dilatational wave velocity is tabulated for several plastics, metals, ceramics and glasses. Beryllium has the highest stress wave velocity among the metallic elements. Corundum (α - alumina) and silicon carbide are among the highest for ceramic bodies. Therefore, impact velocities above 13 kilometers per second are probably in the hyper-velocity region for elastic wave propagation in all materials.

The transition region between subsonic and supersonic velocities is defined here as the velocity range lying above the lowest elastic wave velocity (Rayleigh waves for short duration impact) and below the highest elastic wave velocity (bulk dilatational wave velocity). The transition region will become broader as Poisson's ratio increases towards 0.5 so that different target materials will have both different critical impact velocities (i.e., where $V = C_1$) and different transition velocity ranges.

In compression, most materials exhibit an increasing Young's modulus with increasing strain, i.e.,

$$\frac{d\sigma_t}{d\varepsilon} \leq Y \leq \frac{d\sigma_c}{d\varepsilon} \tag{159}$$

Similarly, the bulk modulus (K) usually increases under isostatic compression. In isotropic materials, the relationship between the shear modulus (G), Young's modulus and bulk modulus is given by

$$G = \frac{3KY}{9KY} \tag{160}$$

Since both Y and K increase under isostatic compression, the shear modulus of isotropic solids will also increase under the same conditions. In some solids the elastic moduli increase with temperature. In these cases isostatic compression will cause a decrease in the elastic moduli. Negative pressure coefficients of elastic constants have been measured at room temperature for fused silica and Pyrex glass both of which have positive temperature coefficients of the elastic constants below 500°C.

The behavior of the elastic constants of single crystals under isostatic pressure is more complex.(45) The shear stiffness coefficient (C_{44}) decreases with pressure in certain cubic crystals, notably KCl and RbCl.(46) In the less symmetric crystals, several of the elastic constants may have negative pressure coefficients. Alpha-quartz, for example, has at least two negative pressure coefficients as shown in Table 5. In alpha-quartz, the shear stiffness along the optic axis (C_{66}) decreases with pressure while the shear stiffness along the x and y axes (C_{44}) increases with pressure. Clearly, generalizations about the effects of pressure upon the shear modulus based upon atomic force-constant considerations must include more than the nearest neighbor interactions if negative pressure coefficients are to be predicted.

2. Plastic Stress Waves. The elastic wave velocity relations given in the previous section are valid for small amplitude stress waves. With increasing stress-wave intensities, the velocity relations become nonlinear functions. These nonlinearities arise from two different factors. The first is the nonlinearity caused by higher order terms in the stress-strain relations for finite deformations.(47) The theory for finite amplitude stress waves is a complete subject in itself and will not be treated here. The second is the nonlinearity associated with plastic deformation where the tangent modulus of elasticity $(\partial\sigma/\partial\varepsilon)_{\varepsilon_1}$ associated with infinitesimal amplitude stress waves is dependent upon the strain. High-intensity stress waves whose stress amplitude exceeds the elastic limit are known as plastic waves. In general, the plastic-wave velocity is dependent upon both the strain and the strain rate.(48)

Strain-rate effects in metals have received extensive experimental study. Each class of metals or alloys appears to behave in a different manner. Dislocation theory(49) provides a theoretical explanation of strain-rate effects. The evidence suggests that for crystalline materials, strain rate dependence is associated with motions of dislocations. Dislocations are arrays of lattice-point defects which may take several different forms, e.g., a line, a loop, a helix, a screw or combinations thereof. Each type of dislocation has a characteristic velocity which is dependent upon the host lattice structure and the absolute temperature. Hence a general discussion of strain-rate dependence becomes quite complex. The possibility of dislocation motion at velocities above the highest elastic stress wave velocity is the subject of considerable controversy. If the velocity of any dislocation motion may not exceed the fastest stress wave velocity (C_l), under hypervelocity impact conditions, dislocations ahead of the penetrating projectile are not free to move and the intrinsic strength or dynamic yield point is determined by the interatomic forces alone.

Plastic waves have been studied extensively under tension impact conditions. Because of the decreasing slope of $d\sigma_t / d\varepsilon$ with increasing strain for most metals, the plastic wave portion of a tension impact disturbance travels with a lower velocity than the elastic wave portion causing the stress pulse to become elongated at positions remote from the point of disturbance.(44)

3. Shock Waves in Solids. Since the elastic moduli for isotropic solids usually increase under compressive stress, the several stress wave velocities will also increase with compressive stress. Thus, attempts to propagate intense stress waves will result in the generation of a discontinuous wavefront. Stress waves which require discontinuous functions to describe the wavefront are known as shock waves. The shock wave velocity* will usually be greater than the corresponding elastic wave velocity in a given isotropic solid.

In a gaseous medium, the thickness (t_s) of an intense shock front is equal in length to a few mean free paths of the gas molecules.(50) By analogy, the shock front thickness in a solid medium is on the order of a few phonon mean free paths. In gases, thermodynamic equilibrium is reached

---

*The term shock wave as used in the literature generally refers to an intense bulk-dilatational wave. However, in the broader context used here, shear-mode shock waves are also possible.

only at finite distances behind the shock front. Similarly, thermodynamic equilibrium in solids behind an intense shock front requires distances equivalent to several phonon mean free paths. The lack of thermodynamic equilibrium within the shock front can be illustrated by comparison of the impact velocity with the instantaneous velocity of lattice vibrations (near room temperature). Assuming, for convenience, that the lattice vibrations behave as harmonic oscillators, (i.e., $x = X \sin \omega t$) then the instantaneous lattice-point velocity dx/dt will be given by

$$\frac{dx}{dt} = \omega X \cos \omega t$$

where ω = $2\pi f$

f = frequency of lattice vibrations

X = maximum displacement of the vibrating atom within the lattice unit cell

For a maximum displacement of one-tenth thelattice spacing (d), a lattice frequency of 10^{13} cycles per second (infrared band), and a nominal lattice spacing of 5 angstroms, the maximum instantaneous lattice-point velocity is

$$\left(\frac{dx}{dt}\right)_{max} = \omega X$$

$$\left(\frac{dx}{dt}\right)_{max} \simeq 3 \text{ Km/sec}$$

Thus, the maximum lattice-point velocity is less than the impact velocity in the hypervelocity region. This simple calculation is sufficient to illustrate that even on an atomic scale, impact velocities in the supersonic range represent a gross disturbance to the lattice point displacements at the impact interface.

The phonon mean free path (Λ) in alpha-quartz at 0°C is 40×10^{-8} cm or about 8 lattice spacings(51) given by

$$\Lambda = \frac{3K}{H\bar{C}}$$

where K = thermal conductivity

H = heat capacity per unit volume

$\bar{C}$ = "mean sound velocity" - space averaged elastic wave velocity

The shock front thickness (t_s) in alpha-quartz would be in the order of one micron near room temperature ($t_s > \Lambda$).

D. Collisions Involving Porous Bodies

The calculations involving porous meteoroids are especially important because of the relatively great frequency of occurrence of cometary meteoroids. Impacts and shock waves in porous materials have been studied to a very limited extent. Altshuler et al (10) obtained shock wave data for porous (specific gravity = 5.52) and non-porous (specific gravity = 7.85) iron to 5×10^6 atm. The equation of state for tuff, a porous rock, is also available.(5,8)

In the following sections, the conditions during impacts between porous materials and non-porous materials are compared to indicate the differences caused by the presence of pores.

Case I - Impacts of Porous Meteoroids Against Solid Surfaces

Calculations of the shock-wave characteristics for impacts between porous and solid iron, using Altshuler's data and assuming planar shock waves, will be used to indicate the effect of porosity. The Hugoniots are shown in Figure 25. The presence of porosity results in an increase in the pressure and energy per unit mass at a given density of material in the shock front. Since the pressures in the meteoroid and space vehicle surfaces must be equal at the point of impact, the shock and particle velocities can be determined. For example, consider the case of a porous iron meteoroid colliding with a solid iron space vehicle surface at an impact velocity of 9 km/sec. If we ask which combination of particle velocities for the porous and non-porous materials add up to the impact velocity, we find using Figure 26 that at equal interface pressure the particle velocity (u_1) in the solid vehicle skin is 3.8 km/sec. While the particle velocity ($\hat{u}_1$) in the porous "meteoroid" is 5.2 km/sec. The shock velocities and density ratios can be read from Figure 27. The energy per unit mass can be calculated from

$$e_1 = \frac{p_1}{2\rho_0}\left(1 - \frac{\rho_0}{\rho_1}\right)$$

The results are given in Table 6. The energy per unit mass in the porous "meteoroid" (1.4×10^{11} ergs/gm).is significantly greater than that in the solid vehicle skin (0.76×10^{11} ergs/gm). It seems likely that this energy distribution will result in decreased meteoroid penetration due to greater evaporation which in turn is due to greater conversion of kinetic energy into thermal energy at impact. This conversion into thermal energy is illustrated in Figure 28, which has been revised from Altshuler's paper. Curve $v_0 - p_1$ is the schematic shock compression curve for a non-porous material. The thermal energy (E_T) added to a unit mass compressed to v_1 is indicated by the area of triangle $p_1 v_1 v_0$ less the area of triangle $p_k v_1 v_0$ which is work required to compress the material to v at 0°K. (E_k). The same type of material (i.e., iron) containing pores will be compressed by shock waves to various states along $v_\infty p_2$. If we neglect the small amount of energy required to remove the pores by compression at absolute zero, (indicated by the dotted line), the extra thermal energy added (ΔE_T) to the porous material to compress it to v_1 is given by the area $p_1 p_2 v_\infty v_0 p_1$. Presumably, the increased temperature and pressure at p_2 will cause increased evaporation or melting of the porous material when the pressure is released.

Cases II-V

When a non-porous meteoroid collides with a porous vehicle skin (Case II), the particle velocity in the meteoroid is less than that in the vehicle skin (see Table 5). The shock velocities and density ratios are also reversed and the sign of the internal energy difference changes. When a non-porous meteoroid collides with a non-porous vehicle skin (Case III) at the same velocity as the preceding cases, the resulting interface pressure is increased and the internal energy increase per unit mass is the same in both bodies. When a porous "meteoroid" collides with a porous vehicle skin (Case IV), the initial interface pressure is lower than in the previous cases and the internal energy increase per unit mass is the same in both bodies and is roughly the same as the value in Case III. To increase the impact velocity so that the initial interface pressure is the same as that in Case III with porous materials requires an impact velocity of 12.2 Km/sec. In this case (Case V) the particle and shock velocities and the density ratios are increased. The internal energy increases per unit mass in this case is 2.0×10^{11} ergs/gm.

It is evident that even a small amount of porosity significantly effects the shock variables. The most important of these effects is the increased thermal energy per unit mass. In the initial phase of crater formation, the increased energy converted to thermal motion becomes unavailable to do structural damage.

If the materials are very porous, as seems to be the case for cometary meteoroids, the impact area is increased considerably and the initial interface pressure will be decreased. Due to the large increase in impact area it may be better to calculate the crater depth using a one-dimensional theory.

E. Crater Wall Criterion

1. The Intrinsic Strength of Crystals. At low strain rates the shear strength in crystalline materials is determined by the type and distribution of dislocations. At high strain rates or when the geometry hinders dislocation motion, the measured strength approaches the theoretical limit imposed by interatomic forces.

Under isostatic compression, the engineering strength of most non-porous materials increases markedly. Bridgeman's data (52) on static compressive strength of several metals and ceramics for pressures in the region of 400,000 psi are given in Table 7. The static compressive strength increases with hydrostatic pressure becoming manyfold higher in normally hard and brittle materials. These data provide evidence of the importance of relaxation processes to static and dynamic mechanical properties. The processes are highly restrained under isostatic pressure so that the static strength approaches the dynamic strength.

A method, originally due to Frenkel, for estimating the theoretical shear strength of crystals is described by Kittel.(51) If one considers the stress due to displacement of one perfect plane of atoms relative to another as shown in the sketch below, the stress to a first approximation can be represented by a sine function

$$\sigma = \frac{Ga}{2\pi d} \sin\left(\frac{2\pi x}{a}\right)$$

in which σ is the stress, G is the shear modulus, a is the space between atoms in a plane, d is the spacing between planes and x is the displacement within a plane.

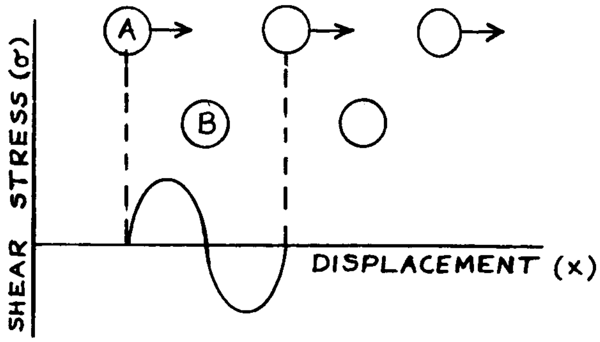

As atom Ⓐ moves over atom Ⓑ the stress increases, passes through a maximum and then decreases to zero. When atom Ⓐ is directly above atom Ⓑ, it is in a state of unstable equilibrium with respect to forces in the x direction. If the stress at the maximum value of this function is considered to be the critical shear stress, the value of the critical shear stress (σ_c) is given by $\sigma_c = Ga/2\pi d$ so that when a and d are approximately equal, as for the case of shear in a $\langle 100\rangle$ direction on a $\{100\}$ plane in a cubic crystal

$$\sigma_c = \frac{G}{2\pi}$$

in which G is the shear modulus given C_{44}. This approach to calculation of the critical shear strength has been refined, according to Kittel,(51) by J. D. Mackenzie using an estimate of the form of the interatomic forces and by "consideration of other configurations of mechanical stability that the lattice may develop as it is sheared." These effects reduce the critical shear strength to about G/30 in some cases.

Strengths as high as those predicted by this atomic model have been observed for a number of materials in whisker form. In these crystals the geometry restricts dislocation motion. Hoffman(53) lists the Young's modulus, ultimate tensile stress, and the tensile stress to Young's modulus ratio for the strongest whiskers prepared from a number of materials. Several materials from this list are retabulated below with addition of the dynamic shear modulus and the maximum shear stress ($\sigma_{s\,max}$) to shear modulus ratio (assuming $\sigma_{s\,max} = \frac{1}{2}\sigma_t$).

COMPARISON OF THEORETICAL AND OBSERVED STRENGTH

	Young's Modulus (E)	Dynamic Shear Modulus (G)	Ultimate Tensile Stress (σ_t)	$\frac{\sigma_t}{E}$	$\frac{\sigma_s\ max}{G}$
Iron	29×10^6 psi	11.9×10^6 psi	1.9×10^6	1/15	1/12
Copper	18	6.7	0.43	1/42	1/32
Sapphire (corundum)	74	23.5	1.7	1/43	1/28
Carbon	1×10^6		0.88	1/11	----

The ratios σ_s/G can be compared with $1/2\,\pi$ and 1/30. The observed ratios correspond quite well with the theoretically derived values. Since the observed strength of whiskers increases with decreasing whisker diameter and since the whiskers may have failed in tension rather than shear, the results for smaller diameter whiskers failing in shear are expected to yield larger ratios. The possibility of still larger strengths is confirmed by the recent results of McQueen and Marsh (54) who showed that the yield strength of copper is in excess of 150 kilobars for shock wave experiments. If the maximum shear stress is one half the tensile stress at yielding, this indicates a shear stress of 1.02×10^6 psi. Therefore, for copper $\sigma_s/G = 0.152$ which can be compared with $1/2\,\pi = 0.159$, giving an unexpectedly close comparison.

McQueen and Marsh also indicate a critical pressure on the Hugoniot which corresponds to the yield point ($dP/dV = 0$). The negative pressure at this point is a theoretical tensile strength. These theoretical strengths, with corresponding shear stresses and other data are given in Table 8. The calculated values of σ_s/G based on this information are somewhat larger than $1/2\pi$. Based upon all of the information given above, the critical shear strength $= G/2\pi$ is considered to be the best available value for the shear strength at high strain rates.

2. The Influence of Shear Strength on Crater Formation. It has been a common practice in fitting impact equations to experimental data to normalize the impact velocities to the velocity of sound in the undisturbed medium. The presence of a transition region, the velocity range near the sound velocity in which there is a change in the relationship between crater depth and impact velocity, has served as a partial justification for this practice. However, the reason for the change in the relationship between crater depth and impact velocity has not been clear. It seems reasonable that the processes governing failure (i.e., crater formation) should depend primarily on the properties of the disturbed medium rather than the undisturbed medium since there is a substantial pressure discontinuity at the shock front even after the crater has reached its final form.

Pressure profiles for impact of iron on iron and a natural meteoroid on tuff have been calculated numerically by Bjork.(5, 8) These profiles indicate, as might be expected, that the pressure gradients in the disturbed material are greatest near the crater lip. It seems likely that shearing of the material at the crater lip is the first requirement for ejection of material from the crater, at least in regions far from the impact point.

If one considers a cube of material at the crater lip, and assumes that the material on the inside (toward the impact point) has already been removed or melted, it is possible to visualize the shear stresses on this material. The cube is pressed from behind by the high pressure material in the cavity. Motion is resisted by the pressure of the material moving ahead of it and by inertial forces and shear stresses. As the crater wall reaches its final position, the motion of material slows down and stops while the pressure gradients and shear stresses remain substantial so that, at this point, the inertial forces in the tangential direction can be neglected. Therefore, the principal factors determining whether or not the material at the crater lip will be ejected are the pressure gradient tangential to the wave front and the shear stresses in the wave front.

It is obvious that the choice of a cube as the beam or ring element on which the forces act is arbitrary. At the very high pressure gradients established near the impact point these forces will act on a very thin ring since the material nearer the impact point will have been ejected (Figure 29a). As the intensity of the shock decreases, the thickness of the ring on which these forces act will increase (Figure 29b). But the increase in thickness is limited because the pressure decreases sharply toward the open crater (Figure 29c). This increase in thickness is consistent with the observation that small fragments are ejected from the crater early in the process at high velocities and large fragments at low velocities later in the process.(22) Reasonable dimensions for the radial distance over which the pressure difference acts to cause shear are also indicated by the thickness of the crater lip after crater formation is complete

(Figure 29d).

3. The Dynamic Shear Modulus and Intrinsic Strength of Structural Materials. An examination of the elastic property data in Tables 4, 5, and 7 indicates that high values of dynamic shear modulus are observed for low density metals such as beryllium, refractory metals such as tungsten, and for ceramics such as corundum (Al_2O_3) and silicon carbide which contain elements from the center of periods 2 and 3 of the periodic table. If one calculates the intrinsic shear strength as a fraction of the shear modulus as suggested by Frenkel and Mackenzie, the low density metals and ceramics will have the highest strength to specific gravity ratios. The intrinsic shear strength ($G/2\pi$) to specific gravity ratio of beryllium is 1.85×10^6 psi and for silicon carbide it is 1.23×10^6 psi. A comparable value for 34T stainless steel is 0.22×10^6 psi.

There remains some uncertainty with respect to the choice of shear modulus values. The values chosen here are for polycrystalline samples. However, almost all single crystals show a substantial degree of elastic anisotropy. The effect of anisotropy on crater formation has been illustrated by Eichelberger and Gehring.(55) If the impacting particles are much larger than the individual grains of the target material so that the forces resulting from impact are spread over many grains, the correct choice would seem to be the properties of the polycrystalline body. In intermediate cases, in which failure can occur due to forces spread over only a few grains, the choice is uncertain. Some materials are very weak in shear in particular crystal directions. For example, the shear moduli for beta brass (CuZn) given by Lazarus(56) are $C_{44} = 8.24 \times 10^{11} \frac{\text{dynes}}{\text{cm}^2}$ and $1/2\ (C_{11} - C_{12}) = 0.975 \times 10^{11}$ dynes/cm^2.

This large anisotropy is characteristic of body centered cubic structures composed of metals whose ions have closed shells (Zener[57]). In the case of large grain size and substantial anisotropy, it may be important to use the smallest shear modulus to calculate the intrinsic strength.

4. Variation of the Dynamic Shear Modulus with Temperature and Pressure. The effect of temperature and pressure on the shear modulus, may be important in calculation of the intrinsic strength. The temperature is of direct importance in the case of space radiators operated at temperatures high enough to affect the mechanical properties of the materials used. The shear modulus of materials usually decreases with increasing temperature but in a few cases, for example vitreous silica, an increase is observed. The temperature variation of the shear modulus is influenced by the change in shear modulus with volume at zero temperature, the thermal energy and the thermal expansion. The effect of target temperature on crater volume has been illustrated by Eichelberger and Gehring(55) based mainly on data given by Allison et al.(58) The results indicate a marked dependence of crater volume on the properties of target materials as these properties are affected by temperature. The metal used were lead, aluminum, copper, zinc, and cadmium. These targets were impacted at 5.01 Km/sec. The crater volumes increased substantially with increasing target temperature.

The variation of the shear modulus of pure aluminum as a function of temperature has been studied by Kê.(59) The shear modulus decreases linearly with temperature for aluminum single crystals and there is a pronounced decrease in shear modulus of polycrystalline aluminum in the temperature range from 200-400°C. Internal friction measurements at low frequencies indicate that this variation in polycrystalline aluminum is caused by grain boundary relaxation.

The internal friction measurements indicate a long relaxation time for the grain boundary movement. Therefore, the linear variation in shear modulus shown for the single crystal sample is more appropriate than the values for pure polycrystalline aluminum for use with samples at the high strain rates characteristic of meteorite impact.

Similar data for beryllium has not been found so far. For equiaxed grains of uniform size, Zener(60) has shown that the ratio of the relaxed to the unrelaxed modulus is given by

$$\frac{G_R}{G_U} = \frac{2(7+5\nu)}{5(7-4\nu)}$$

in which ν is the Poisson's ratio. The Poisson's ratio of beryllium is very low and shows marked anisotropy, varying from 0.10 ± 0.02 ⊥ "c" axis to 0.035 ± 0.01 ∥ "c" axis. Therefore, the ratio of the relaxed to unrelaxed shear modulus (G_R/G_U) will be between 0.42 and 0.45. The variation of the dynamic elastic modulus (Young's modulus) with temperature is given by White and Burke.(61) It decreases from about 45 x 10^6 psi at room temperature to about 39.5 x 10^6 psi at 1200°F. If the temperature variation of the shear modulus is similar to the temperature variation of Young's modulus, the combined effect of the ordinary temperature variation and grain boundary relaxation could lead to a relaxed shear modulus at 1200°F as small as 37% of the room temperature value. As mentioned earlier, the unrelaxed values are probably applicable at the high strain rates characteristic of meteoroid impact. The characteristics of the grain boundaries can be altered by alloying if this is considered necessary.

The pressure dependence of the shear modulus may also be important. The important pressure for the crater wall criterion is that existing in the material near the crater wall at the time the crater formation ceases. These pressures are relatively low compared with the pressures existing at earlier times. Since the pressures are lowest near the crater lip and the elastic constants usually increase with the increasing pressure, the weakest material subject to shear forces is the material at the crater lip. The pressure range of interest is 10^4 to 10^5 bars.

The pressure dependence of the elastic constants has been measured by several investigators.(46, 62-64) Measurements have been made for KCℓ, NaCℓ, CuZn, Cu, Ag, Au, Al, α SiO_2 and Mg; in most cases to pressures of about 10 kilobars, the lower end of the range of interest.

If we take impacts of aluminum on copper as an example to evaluate the importance of the pressure dependence of the shear modulus, we find that the shear modulus of copper can be expected to increase about 2.8% in 10^4 bars and about 28% in 10^5 bars. The pressure derivative of the shear modulus of other materials is larger than that of copper in many cases but in these cases the shear modulus and critical shear strength are usually smaller so that the pressure range is smaller and the percentage change in the shear modulus for this pressure range may remain about the same. These changes in shear modulus are somewhat smaller than the uncertainties in the choice of a strength criterion. Furthermore, the increases due to pressure may be somewhat offset by decreases due to temperature rise when the shock wave passes. Therefore, the use of the shear modulus at atmospheric pressure in the critical shear strength criterion is justified until further improvements are made in this shear strength criterion. The most important variation in properties likely to occur in space radiators is the decrease in the elastic constants due to high operating temperatures. For aluminum used at 370°C ($\sim$ 700°F) the decrease in shear modulus for a single crystal is about 23%. In the case of steel impacting on 25-0 aluminum, the increase in temperature from room temperature to 370°C results in a 19% increase in crater radius. Again, in view of the crudeness of the crater-wall criterion it doesn't seem necessary to make a correction but, at higher temperatures, a correction would probably be necessary.

III. SUMMARY AND ILLUSTRATIVE CALCULATIONS

This part presents a brief synopsis of the present status of this theory, and shows how to use the formula for crater size. No familiarity with other parts of the report is assumed. The formulas below are presented in such a way that the interested reader may apply them readily, without the necessity for going through the lengthy analysis above.

1. Review of the Analysis

When a particle strikes a target surface at high speed, large amounts of energy and momentum are quickly deposited over a very small portion of the surface. This release drives a strong shock wave, usually hemispherical in shape, into the target, generating extremely large pressures. Because these pressures (normal stresses) are so large compared with the material's resistance to shear deformation, one may consider that the target material behaves like an inviscid, compressible fluid. Thus the problem of determining the response of the target is essentially that of solving for the flow behind a strong, hemispherical shock wave. This flow pattern is described by the standard fluid-mechanical equations expressing the conservation of mass, momentum, and energy, together with the equation of state of the medium. The solution of these equations is an exceedingly formidable task. They are coupled, nonlinear partial differential equations in two independent spatial variables, as well as the time. Furthermore, as the shock wave advances into the target, distributing its energy over more and more mass, the strength of the shock decays, so that ultimately the fluid-mechanical approximation itself ceases to be valid. At this stage, a transition to a model which properly accounts for the plastic and elastic behavior of the medium is needed.

In order to make possible an analytic solution of this complicated problem, a series of approximations to the physical picture has been made. They can be grouped into three main areas, and are described in the paragraphs that follow.

The first simplification is to examine only that class of solutions in which the fluid motion is self-similar, i.e., the distribution of physical quantities at successive instants is assumed to be the same when viewed on a scale defined by the shock radius at each instant. The mathematical consequence of this is to suppress time as an independent variable. Each physical quantity, instead of depending separately on the time and on the distance r from the impact point, is now a function of the combination $r/R_s(t)$, where $R_s(t)$ is the shock-wave radius at any instant. This reduction in the number of independent variable constitutes a significant simplification in the differential equations that must be solved. At the same time, it imposes two restrictions.

The first restriction, which assures that there will be no explicit time dependence in the differential equations, is that the shock radius must grow as a power of the time. Thus, out of all the possible solutions of the basic equations, we examine only that class for which $R_s \sim t^N$.

The second condition imposed by the similarity assumption is that the boundary conditions must also be independent of the time, and this in turn restricts the type of state equation that can be used to those of the form

$$e = p\varphi(\rho)$$

where e is the internal energy per unit mass, p the pressure, and φ is any function of the density ρ. In actual fact, the thermodynamic states of typical target materials are well represented by the Mie-Grüneisen equation of state, in the range of interest here. This equation may be written in the form

$$e = \frac{p}{\rho \Gamma(\rho)} - \Delta(\rho)$$

where the Grüneisen constant, Γ , depends weakly on ρ , and where the function Δ depends only on density. The leading term of this equation can be accommodated in a self-similar solution, and will obviously be a good approximation at very high pressure, where the second term, $\Delta(\rho)$, is negligible. The theory in its present state assumes that $\Delta(\rho)$ can be neglected, and makes the further approximation of using the equation of state of a perfect gas of constant specific-heat ratio γ

$$e = \frac{p}{(\gamma - 1)\rho}$$

This approximation amounts to the neglect of the small variation in the Grüneisen factor $\Gamma(\rho)$, and permits all the known analyses for blast waves in perfect gases to be applied to the present problem. In every impact, some portion of the hydrodynamic flow will occur at pressures sufficiently low that the influence of the term $\Delta(\rho)$ is not negligible. In an attempt to account partially for the presence of the term $\Delta(\rho)$, the value of γ that is used in any particular impact case is taken as the value that matches the actual state equation at the impact point. For a perfect gas, the density ratio across a strong shock is always $(\gamma + 1)/(\gamma - 1)$. Thus, if the actual density ratio across the shock that starts into the target from the impact point were to be 2, then γ would be chosen as 3. For a given projectile-target combination, the "effective γ" depends on the impact speed.

The second important area in which approximations have been made deals with the extent to which the conservation of energy and momentum are satisfied. Two types of solution have been studied. The first, which allows for spatial variations in two directions, permits conservation of energy and momentum, and explicitly describes the pattern of mass ejection from the target. The second type of solution considers only variations radially from the impact point, conserves only the total energy, and does not describe the pattern of mass ejection. All the results that have been found for the former solution indicate that it is nearly identical to the vastly simpler constant-energy solution. The physical explanation for this is not presently known, although several speculations have been advanced. The simplest of these is based on the experimental observation that targets struck by hypervelocity projectiles often acquire momenta many times that of the projectile, implying that the material ejected from the target must also carry several times the projectile momentum. Thus it appears the momentum of the projectile itself plays a relatively minor role in the overall conservation process.

These first two approximations -- that of similarity, and that dealing with neglect of momentum conservation -- are sufficient to permit an extremely simple solution for the time history of the shock radius

$$R_s(t) = \left(\frac{25}{8\pi I_1(\gamma)} \quad \frac{E\,t^2}{\rho_0} \right)^{1/5}$$

where E is the kinetic energy of the projectile, t the time after impact, ρ_0 the undisturbed target density, and $I_1(\gamma)$ a function representing the influence of the equation of state. This prediction shows reasonable agreement with the very limited amount of data that have been published so far. It disagrees chiefly in that the experiments tend to favor a time dependence more like $t^{2/3}$, which suggests that the experiments lie in a range intermediate between the strong-shock limit ($R_s \sim t^{2/5}$) and the acoustic limit ($R_s \sim t$). In any event, the agreement between experiment and the present form of the theory is not bad, and may be expected to improve at higher impact speed. Thus, if used with caution, it will serve as a basis for crater-size predictions.

This brings us to our third and final approximation, which is not associated with the fluid-mechanical equations as such, but rather with the later stages of crater formation, where the plastic and elastic response of the target becomes important. This stage is reached when the inviscid-fluid approximation breaks down, i. e., when the target's resistance to shear deformation is no longer negligible compared to the pressure being generated by the shock. Thus, the blast-wave solution must be cut off at the instant when this pressure has become equal to the intrinsic shear strength, $G/2\pi$, G being the dynamic shear modulus. Ideally, one would use the conditions at the instant of cutoff as the starting values for a plastic- and elastic-wave solution, from which the ultimate crater radius could be found, as a function of the cutoff value of the shock radius, among other things. The theory in its present form does not actually carry out such a solution. Instead, the radius of the crater is taken to be equal to the cutoff value of the shock radius. The formula that results

$$\frac{R_c}{d} = \left(\frac{1}{12(\gamma+1)I_1(\gamma)} \, \frac{\rho_p V^2}{G/2\pi} \right)^{1/3}$$

is quite simple, and agrees well with experiment, especially in materials like lead, in which hypervelocity conditions are achieved at relatively low impact speeds.

In summary, then, the net effect of the set of approximations described above is to make possible a simple solution, giving the dependence of the crater radius on the pertinent impact parameters. In addition to its utility in making predictions, the analysis contributes to our fund of analytical understanding of the phenomenon as a whole, especially as regards the importance of momentum conservation, and the separate influences of the state equation and material strength. The theory is capable of considerable improvement, by accounting for nonsimilar effects in the fluid-dynamic phase, and by accomplishing a better description of the plastic and elastic stages of the process. The need for more definitive experiments on shock-wave time histories is clearly indicated, and, furthermore, it appears that some measurements of the dynamic strength properties of targets must be made if the results of experiments are to be interpreted properly.

2. Illustrative Calculations

The formula recommended for crater size is Eq. (78) of Section I.

$$\frac{R_c}{d} = \left(\frac{1}{12(\gamma+1)\,I_1(\gamma)} \quad \frac{\rho_p V^2}{\mathbb{P}} \right)^{1/3}$$

Here R_c denotes the crater radius (the crater is assumed to be hemispherical) and d is the diameter of the projectile. (For nonspherical projectiles, d should be taken as the diameter of a sphere of equal mass.) ρ_p is the density of the projectile material, and V the impact speed. The symbol $\mathbb{P}$ denotes the intrinsic shear strength of the target, $G/2\pi$, where G is the dynamic shear modulus as measured, for example, by an ultrasonic technique. Table 4 lists values of $G/2\pi$ for a number of materials. Both $\rho_p V^2$ and $\mathbb{P}$ have the units of pressure. A convenient set of units to work with is to take ρ_p in gm/cm^3, V in cm/sec, and $\mathbb{P}$ in gm/cm-sec^2, i. e., in dynes/cm^2. Some useful conversion factors are

Multiply:	By	To Get
feet/sec	30.48	cm/sec
km/sec	10^5	cm/sec
psi	6.895×10^4	dynes/cm^2
megabars	10^{12}	dynes/cm^2

The only quantity remaining to be determined is γ, which characterizes the state equation of the target. The quantity γ is actually the adiabatic index of a perfect gas whose equation of state matches that of the target in the vicinity of the impact point. The determination of γ is thus essentially a solution for the initial conditions that exist between the shock wave that propagates into the target and the shock wave that travels back into the projectile. The steps to follow are given below

1. Choose a value for the pressure p_1 in the region between the shocks. This pressure is the same in the target and projectile.

2. Find the particle speeds in both the target and projectile materials by applying the following equation to each one, respectively

$$u_1 = c \left\{ \frac{\sqrt{1 + 4s \;\, p_1/\rho_0 c^2} \;\; - 1}{2s} \right\}$$

Table I gives the values of c, s, and $\rho_0 c^2$ for various materials.

3. The impact speed, V, is now found by adding the two velocities found in the preceding step: $V = u_1)_{\text{PROJECTILE}} + u_1)_{\text{TARGET}}$. This is the speed required to generate, at the impact point, the pressure chosen in Step 1.

4. The value of γ corresponding to the impact speed of Step 3 is now found from

$$\gamma = \frac{2\left[c + s u_1\right]}{u_1} - 1$$

wherein the values used are those appropriate to the target material.

Repeating these steps at a series of values of p_1 then determines $\gamma(V)$, and this, in turn, allows one to calculate R_c/d, using Fig. 8 for the function $(\gamma+1)\, I_1(\gamma)$.

CONCLUDING REMARKS

The net result of the set of approximations described above is to make possible an extremely simple solution, giving the dependence of crater radius on the diameter, density, and speed of the projectile, and on the dynamic strength and state equation of the target. Both fluid-mechanical and solid-state considerations play a role in this solution, and their individual effects are combined by the simple expedient of terminating the blast-wave solution at the point where the shock pressure has decayed to the intrinsic strength of the target. The fact that the solution for the fluid-mechanical phase is simple enough to permit such an incorporation of the target strength is a direct consequence of the fact that a constant-energy approximation can be used. The formula that results displays reasonable agreement with experiment, and may be expected to improve at higher impact speeds, where the strong-shock approximations hold over a longer portion of the process.

Improvements in both the fluid and solid aspects of the theory described above can be achieved, at little or no expense in simplicity of the results. In regard to the blast-wave portion, it would appear that the most fruitful area to explore is the development of non-similar solutions. The most definitive test to which this part of the solution can be put is the prediction of shock location as a function of time. The experimental evidence presently available in this area is quite limited, and apparently lies in a transitional regime where the shock speed has begun to decay from the blast-wave behavior $(R_s \backsim t^{2/5})$ toward the acoustic limit $(R_s \backsim t)$. To properly account for this behavior, the hydrodynamic phase of the solution must be extended, so as to incorporate the nonsimilar effects that enter by way of the low-pressure term in the state equation. In spite of this deficiency, however, even the presently available form of the solution gives a surprisingly accurate prediction of the shock-wave location, and it may be expected to improve at higher impact speeds.

On the solid-state side of the question, the most obvious area in need of improvement is the rule for determining the crater size. There is no theoretical obstacle to making the transition from blast-wave theory to a plastic- and elastic-wave description at late time. Such an analysis would provide a general relation between the final crater dimensions and the shock radius at the instant of transition. Presently, these are assumed equal.

Finally, there is a need for further study of the importance of momentum conservation, since the neglect of this consideration is crucial in achieving the simplicity of the present solution.

Certain aspects of these theoretical findings have application to the design and interpretation of experiments. Quite apart from its obvious use as a practical method of estimating penetration, the implications of this theory are that many experimental conditions must be carefully examined if results of experiments are to be properly interpreted. In particular, it is important to know the dynamic strength of the target material. Furthermore, the influence of the equation of state demonstrated in these studies produces, at high speed, a variation of crater radius with impact velocity suggestive of "momentum scaling". The fact is that the total energy is the dominant parameter throughout the range of impact speeds, while reduction of the crater size below the value appropriate to pure "energy scaling" can be attributed to the effect of the equation of state. Thus, extensive experiments in substances whose state equations are not well known would appear to be incapable of determining the relative contributions from these two sources.

REFERENCES

1. Eichelberger, R. J., and Gehring, J. W., "Effects of Meteoroid Impacts on Space Vehicles". American Rocket Society Journal 32, No. 10 (Oct. 1962) 1583-1591.

2. Halperson, S. M., and Hall, D. A., "Shock Studies in Transparent Plastic by High-Speed Photographic Techniques". Report of NRL Progress, (Sept. 1961) 37-39.

3. Frasier, J. T., and Karpov, B. G., "Impact Experiments on Wax". Proceedings of the Fifth Symposium on Hypervelocity Impact, Denver, October 30 - November 1, 1961, Vol. II, Part II (April 1962) 371-388.

4. Frasier, J. T., "Hypervelocity Impact Studies in Wax". Ballistic Research Laboratories, Report No. 1124 (Feb. 1961).

5. Bjork, R. L., "Effects of a Meteoroid Impact on Steel and Aluminum in Space". Tenth International Astronautical Congress Proceedings, Vol. II, Springer Verlag (1960) 505-514.

6. Sedov, L. I., "Similarity and Dimensional Methods in Mechanics". Academic Press (1959).

7. Rice, M. H., McQueen, R. G., and Walsh, J. M., "Compression of Solids by Strong Shock Waves". Solid State Physics, Advances in Research and Applications, Vol. 6, Academic Press (1958).

8. Bjork, R. L., "Analysis of the Formation of Meteor Crater, Arizona: A Preliminary Report". Journal of Geophysical Research 66 (1961) 3379-3387.

9. Altshuler, L. V., Bakanoya, A. A., and Trunin, R. F., "Shock Adiabats and Zero Isotherms of Seven Metals at High Pressures". Soviet Physics, JETP 15, No. 1 (July 1962) 65-74.

10. Altshuler, L. V., Krupnikov, K. K., Ledenev, B. N., Zhuchikhin, V. I., and Brazhnik, M. I., "Dynamic Compressibility and Equation of State of Iron under High Pressure". Soviet Physics, JETP, 34, (7) No. 4 (Oct. 1958) 606-614.

11. Walsh, J. H., Rice, M. H., McQueen, R. G., and Yarger, F. L., "Shock-Wave Compressions of Twenty-Seven Metals. Equations of State of Metals". Physical Review, 108 (Oct. 15, 1957) 196-216.

12. Olshaker, A. E., and Bjork, R. L., "Hydrodynamics Applied to Hypervelocity Impact. I. Scaling Laws for Dissimilar Materials". Proceedings of the Fifth Symposium on Hypervelocity Impact, Denver, October 30 - November 1, 1961, Vol. I, Part I (April 1962) 185-223.

13. Taylor, G. I., "The Formation of a Blast Wave by Very Intense Explosion, I, Theoretical Discussion". Proceedings of the Royal Society (A) 201 (1950) 159-174.

14. Taylor, J. L., "An Exact Solution of the Spherical Blast Wave Problem". Phil. Mag. 46 (1955) 317-320.

15. Latter, R., "Similarity Solution for a Spherical Shock Wave". Journal of Applied Physics, 26 (1955) 954-960.

16. Sakurai, A., "On Exact Solution of the Blast Wave Problem". J. Phys. Soc., Japan 10 (1955) 827-828.

17. Davids, N., Huang, Y. K., and Juanzemis, W., "Some Theoretical Models of Hypervelocity Impact". Proceedings of the Fifth Symposium on Hypervelocity Impact, Denver, October 31 - November 1, 1961, Vol. 1, Part I (April 1962) 111-132.

18. Hayes, W. D., and Probstein, R. F., "Hypersonic Flow Theory". Academic Press (1959).

19. Davids, N., and Huang, Y. K., "Shock Waves in Solid Craters". Journal of the Aerospace Sciences 29 (1962) 550-557.

20. Herrmann, W., and Jones, A. H., "Survey of Hypervelocity Impact Information". Massachusetts Institute of Technology, A.S.R.L., Report No. 99-1 (Sept. 1961).

21. Lake, H. R., and Todd, F. C., "Digital Computer Solution for the Propagation of a Spherical Shock Wave in Aluminum". Paper presented at the Oklahoma Academy of Science Meeting, December 14-15, 1961, NASA Accession Number N62-11438.

22. Kineke, J. H., "Observations of Crater Formation in Ductile Materials". Proceedings of the Fifth Symposium on Hypervelocity Impact, Denver, October 30 - November 1, 1961, Vol. I, Part II (April 1962) 339-370.

23. Hafele, W., "Zur Analytischen Behandlung ebener, starker, instationarer Stoswellen". Zeitschrift fur Naturforschung 10a (1955) 1006.

24. Von Hoerner, S., "Losungen der hydrodynamischen Gleichungen mit linearen Verlauf der Gerchwindigkeit". Zeitschrift fur Naturforschung, 10a (1955) 687.

25. Zeldovich, Ya. B., "Motion of a Gas Due to a Pressure of Short Duration (Shock)". Soviet Physics-Acoustics, American Institute of Physics Translation 2 (1956) 25-35.

26. Adamskií, V. B., "Integration of a System of Autosimulating Equations For the Problem of a Short Duration Shock in a Cold Gas". Soviet Physics-Acoustics, American Institute of Physics Translation 2 (1956) 1-7.

27. Zhukov, A. I., and Kazhdan, Ya.m., "Motion of a Gas Due to the Effect of a Brief Impulse". Soviet Physics-Acoustics, American Institute of Physics Translation 2 (1957) 375-381.

28. Mirels, H., "Hypersonic Flow Over Slender Bodies Associated with Power Law Shocks". Advances in Applied Mechanics, Vol. VII, Academic Press, New York (1962).

29. Lees, L., and Kubota, T., "Inviscid Hypersonic Flow over Blunt-Nosed Slender Bodies". Journal of Aeronautical Sciences 24 (1957) 195-202.

30. Franken, P., "High Energy Lasers". International Science and Technology (Oct. 1962).

31. Davison, E. H., Winslow, Jr., P. C., "Space Debris Hazard Evaluation". NASA TN D-1105 (Dec. 1961).

32. Whipple, F. L., "The Meteoritic Risk to Space Vehicles". Vistas in Astronautics, Vol. 1, Pergamon Press (1958).

33. Whipple, F. L., "Particulate Contents of Space". Medical and Biological Aspects of the Energies of Space, Edited by P. A. Campbell, Columbia University Press (1961).

34. Bjork, R. L., "Meteoroids Versus Space Vehicles". American Rocket Society Paper 1200-60 (May 1960).

35. Whipple, F. L., "Photographic Meteor Orbits and Their Distribution in Space". Astronomical Journal 59 (1218) 201 (July 1954).

36. Whipple, F. L., "A Comet Model III, The Zodiacal Light". Astrophysical Journal 121 (3) 750 (May 1955).

37. McCrosky, R. E., "Some Physical and Statistical Studies of Meteor Fragmentation". PhD. Thesis Harvard University (Nov. 1955).

38. Whipple, F. L., "On Meteoroids and Penetration". 9th Annual American Astronautical Society Meeting (Jan. 1963).

39. Slater, J. C., "Introduction to Chemical Physics". McGraw-Hill Book Company, New York (1939).

40. Eastabrook, J. N., "Thermal Expansion of Solids at High Temperatures". Phil. Mag. (Eighth Ser.), 2, 1421 (1957).

41. Benedek, G. B., "The Temperature of Shock Waves in Solids". Harvard University, Cruft Lab. Tech. Rept. 316 (Jan. 1960).

42. Benedek, G. B., "Deduction of the Volume Dependence of the Cohesive Energy of Solids from Shock-Wave Compression Measurements". Phys. Rev. 114, 467 (1959).

43. Wackerle, J., "Shock-Wave Compression of Quartz". J. Appl. Phys. 33 (3) 922 (March 1962).

44. Von Kàrmàn, T., and Duwez, P., "The Propagation of Plastic Deformation in Solids". J. Appl. Phys., Vol. 21 (Oct. 1950) 987-994.

45. Cook, R. K., "Variation of Elastic Constants and Static Strains with Hydrostatic Pressure: A Method for Calculation from Ultrasonic Measurements". J. Accoustical Soc. 29(4) (1957) 445-449.

46. Huntington, H. S., "The Elastic Constants of Crystals". Solid State Physics, Vol. 7, Academic Press, Inc. (1958) 213-351.

47. Marnaghan, F. D., "Finite Deformation of an Elastic Solid". J. Wiley (1951)

48. Malvern, L. E., "Plastic Wave Propagation in a Bar of Material Exhibiting a Strain Rate Effect". Inart. Appl. Math. 8, (1951) 405-411.

49. Bell J. F., "An Experimental Study of the Interrelation Between the Theory of Dislocations in Polycrystalline Media and Finite Amplitude Wave Propagation in Solids". Johns Hopkins Univ., Baltimore, Md., Tech. Rept. 7 (March 1961).

50. Penney, W. S., and Pike, H. H. M., "Shock Waves and the Propagation of Finite Pulses in Fluids". Reports on Progress in Physics (13) (1950) 46-82.

51. Kittel, C., "Introduction to Solid State Physics". Second Edition, John Wiley (1956).

52. Bridgeman, P. W., "Studies in Large Plastic Flow and Fracture With Special Emphasis on the Effects of Hydrostatic Pressure". McGraw-Hill (1952).

53. Hoffman, G. A., "Whiskers". J. Metals 10 (9) 591 (Sept. 1958).

54. McQueen, R. G., and Marsh, S. P., "Ultimate Yield Strength of Copper". J. Appl. Phys. 33 (2) 654 (Feb. 1962).

55. Eichelberger, R. J., and Gehring, J. W., "Effects of Meteoroid Impacts on Space Vehicles". Ballistic Research Lab. Rept. No. 1155 (Dec. 1961).

56. Lazarus, D., "The Variation of the Adiabatic Elastic Constants of KCℓ, NaCℓ, CuZn, Cu, and Al with Pressure to 10,000 Bars". Phys. Rev. 76 (4) 545 (August 15, 1949).

57. Zener, C., "Contributions to the Theory of Beta-Phase Alloys". Phys. Rev. 71 (12) 846 (June 15, 1947).

58. Allison, F. E., Becker, K. R., and Vitali, R., "Effects of Target Temperature on Hypervelocity Cratering". Fourth Symposium on Hypervelocity Impact, APGC-TR-60-39 (1) (Sept. 1960).

59. Ke, T., "Experimental Evidence of the Viscous Behavior of Grain Boundaries in Metals". Phys. Rev. 71 (8) 533 (April 15, 1947).

60. Zener, C., "Theory of the Elasticity of Polycrystals with Viscous Grain Boundaries". Phys. Rev. 60, 906 (1941).

61. White, D. W., Jr., and Burke, J. E., "The Metal Beryllium". Am. Soc. Metals, Cleveland (1955).

62. Daniels, W. B., and Smith, C. S., "Pressure Derivatives of the Elastic Constants of Copper, Silver, and Gold to 10,000 Bars". Phys. Rev. 111 (3) 713 (August 1, 1958).

63. Schmunk, R. E., and Smith Charles S., "Pressure Derivatives of the Elastic Constants of Aluminum and Magnesium". J. Phys. Chem. Solids 9, 100-112 (1959).

64. Lazarus, D., "The Variation of the Adiabatic Elastic Constants of KCl, $NaCl$, CuZn, Cu and Al with Pressure up to 10,000 Bars". Phys. Rev. 76 (4) 545 (August 15, 1949).

65. McQueen, R. G., and Marsh, S. P., "Equation of State for Nineteen Metallic Elements from Shock-Wave Measurements to Two Megabars". J. Appl. Phys. 31 No. 7 (July 1960) 1253-1269.

66. Jaffe, I., Beauregard, R., and Amster, A., "Determination of the Shock Pressure Required to Initiate Detonation of an Acceptor in the Shock Sensitivity Test". American Rocket Society Journal 32 No. 1 (Jan. 1962) 22-25.

67. Susse, C., "Variation of the Elastic Constants of Quartz as a Function of Pressure up to 1000 Atmospheres". J. Phys. Radium 16 (April 1955) 348-349.

68. McSkimin, H. J., "Ultrasonic Pulse Technique for Measuring Accoustic Losses and Velocities of Propagation in Liquids as a Function of Temperature and Hydrostatic Pressure". J. Accoustical Soc. 28 (11) (Nov. 1957) 1185.

69. Herrmann, W., and Jones, A. H., "Correlation of Hypervelocity Impact Data". Proceedings of the Fifth Symposium on Hypervelocity Impact, Denver, October 30 - November 1, 1961, Vol. II, Part II (April 1962) 389-438.

70. Herrmann, W., and Jones, A. H., "Survey of Hypervelocity Impact Information". M.I.T., ASRL Report No. 99-1 (Sept. 1961).

APPENDIX A

TRANSFORMATION OF THE BLAST-WAVE EQUATIONS

This appendix outlines the steps by which the centerline equations may be transformed to the x, y, z coordinate system, where:

$$x \equiv \frac{N\phi}{\eta} \quad , \quad y \equiv \frac{N^2}{\eta^2}\frac{\gamma f}{\psi} \quad , \quad z \equiv \frac{N\tau}{\eta} = \frac{2N}{\eta}\frac{\partial\omega}{\partial\theta}(\eta, 0) \qquad \text{(A-1)}$$

For the constant-energy solution, of course, τ, and hence z, are zero. A convenient starting point is to use the centerline equations in the form

$$(\phi-\eta)\,d\psi + \psi\,d\phi + \psi\left(\frac{\tau}{\eta} + 2\frac{\phi}{\eta}\right)d\eta = 0 \qquad \text{(A-2)}$$

$$-\frac{1-N}{N}\,\phi\,d\eta + (\phi-\eta)\,d\phi + \frac{df}{\psi} = 0 \qquad \text{(A-3)}$$

$$-2\frac{1-N}{N}\,f\,d\eta + (\phi-\eta)\left(df - \frac{\gamma f}{\psi}\,d\psi\right) = 0 \qquad \text{(A-4)}$$

The quantities ϕ and f can be eliminated from these, using

$$d\phi = \frac{\eta}{N}\left(dx + \frac{x}{\eta}\,d\eta\right) \qquad \text{(A-5)}$$

$$\frac{df}{f} = \frac{dy}{y} + 2\frac{d\eta}{\eta} + \frac{d\psi}{\psi} \qquad \text{(A-6)}$$

The resulting set of equations contains only ψ, η, x, y and z:

$$(x-N)\,d\ln\psi + dx + (3x+z)\,d\ln\eta = 0 \qquad \text{(A-7)}$$

$$-x + (x-N)\frac{dx}{d\ln\eta} + x^2 + \frac{1}{\gamma}\frac{dy}{d\ln\eta} + 2\frac{y}{\gamma} + \frac{y}{\gamma}\frac{d\ln\psi}{d\ln\eta} = 0 \qquad \text{(A-8)}$$

$$-2y + (x-N)\frac{dy}{d\ln\eta} + (\gamma-1)y\left(\frac{dx}{d\ln\eta} + 3x + z\right) + 2xy = 0 \tag{A-9}$$

Equation (A-7) has been used in deriving the form of (A-9) shown here. If we now use the continuity equation (A-7) to eliminate $\frac{d\ln\psi}{d\ln\eta}$ from (A-8), and the energy equation (A-9) to eliminate $dy/d\ln\eta$, a little algebra leads to

$$\frac{dx}{d\ln\eta} = \frac{\frac{y}{\gamma}\left(3\gamma x + \gamma z - 2[1-N]\right) - x(x-N)(x-1)}{(x-N)^2 - y} \tag{A-10}$$

which may be regarded as a means of finding η, once x, y and z are known. Next, since the quantity $\frac{1}{y}\frac{dy}{d\ln\eta}$ can be written as

$$\frac{1}{y}\frac{dy}{d\ln\eta} = \frac{d\ln y}{dx}\,\frac{dx}{d\ln\eta}$$

equation (A-9) can be rearranged to

$$\frac{dx}{d\ln\eta} = \frac{2-(\gamma-1)z-(3\gamma-1)x}{\gamma-1+(x-N)\frac{d\ln y}{dx}} \tag{A-11}$$

Equating this value of $dx/d\ln\eta$ to that given by (A-10) then gives

$$\frac{1}{y}\frac{dy}{dx} = \frac{[(x-N)^2-y][2-(\gamma-1)z-(3\gamma-1)x]}{(x-N)\left[y\left(3x+z-\frac{2}{\gamma}\{1-N\}\right)-x(x-N)(x-1)\right]} - \frac{\gamma-1}{x-N} \tag{A-12}$$

In these coordinates, the equation for $\partial\omega/\partial\theta$ may be written as

$$\frac{dz}{d\ln\eta} = \frac{z-\frac{1}{2}z^2-2xz-2y_{\theta\theta}}{x-N} \tag{A-13}$$

where

$$y_{\theta\theta} = \frac{N^2}{\eta^2\psi}\,\frac{\partial^2 f}{\partial\theta^2}(\eta, 0)$$

APPENDIX B

SIMULATION OF METEOROID IMPACT BY ENERGY RELEASE

A major conclusion reached in Part I, above, is that crater formation is controlled chiefly by the energy of the impacting particle, its momentum playing only a secondary role. Thus we may expect to simulate hypervelocity impact by any experiment in which a strong shock wave is driven into a target by the deposition of energy in any form.

It is of central importance, in considering any simulation of this type, to be certain that the mode of energy deposition does in fact drive a strong shock wave into the target. We shall return to this question below, but for the moment we assume that this condition has been achieved, and present the formulas that follow as a consequence.

The relation between crater radius and the amount of energy absorbed by the target is Eq. (77):

$$R_c = \left(\frac{1}{\pi(\gamma+1) I_1(\gamma)} \frac{E}{\mathbb{P}} \right)^{1/3} \tag{B-1}$$

To specify γ in the particle-impact case, we matched the actual conditions behind the shock at the impact point, and found that γ depended only on the impact speed V. We may follow the same procedure for the case of energy deposition by some other means, except that we must now identify the experimental parameter that fixes the shock strength, and hence γ. The quantity that does this is the power being absorbed by the target, per unit area in the plane of the shock. To see why this is so, consider a plane shock wave of unit area advancing at speed u_s into a medium of undisturbed density ρ_0 .

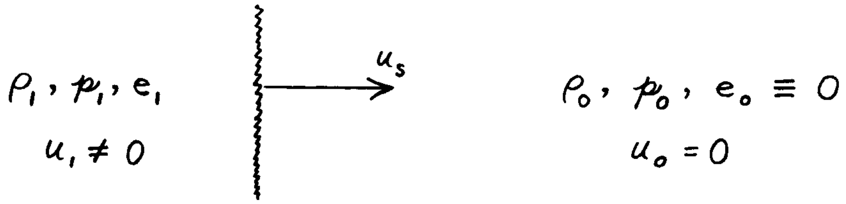

In unit time, this shock processes an amount of mass given by $\rho_0 u_s$ per unit area, and raises it to the energy (per unit mass)

$$e_1 = \frac{p_1}{2\rho_0}\left(1 - \frac{\rho_0}{\rho_1}\right) \qquad \text{(B-2)}$$

Thus the rate of energy acquisition by the material behind the shock, per unit time and area, is

$$\text{power/area} = \rho_0 u_s \frac{p_1}{2\rho_0}\left(1 - \frac{\rho_0}{\rho_1}\right) = \frac{1}{2} p_1 u_1 \qquad \text{(B-3)}$$

The strength of any shock wave may therefore be characterized by the amount of power per unit area which it delivers to the medium through which it travels. In particular, such a specification of shock strength serves to define γ . The Hugoniot curve for iron is interpreted in this light in Fig. 22, where it is seen that weak shock waves, characterized by $\gamma = 10$ (i.e., $\rho_1/\rho_0 = 11/9$) impart about 10^9 watts/cm^2, while extremely strong shocks, for which $\gamma = 2$, transfer to the medium some 10^{13} watts/cm^2. These orders of magnitude are typical of metals. In fact, for any material whose Hugoniot is given by

$$u_s = c + s u_1 \qquad \text{(B-4)}$$

a little algebra will show that

$$\text{power/area} = \rho_0 c^3 \cdot \frac{1}{2} \left(\frac{2}{\gamma - (2s-1)}\right)^2 \left(1 + \frac{2s}{\gamma - (2s-1)}\right) \qquad \text{(B-5)}$$

This function is shown in Fig. 23. In view of the fact that 1.0 megabar-km/sec is equal to 10^{10} watts/cm^2, it can be seen that shock waves in the range of interest here will generally have "power ratings" from 10^9 to 10^{13} watts/cm^2. It is interesting, in this connection, to note that the experiments reported by Altshuler et al[9] achieved shock waves of strength equivalent to 4×10^{11} watts/cm^2

If we consider the deposition of a total energy E over an area A of the target surface in a time τ, it is clear that γ will be a function only of $E/A\tau$. Thus the craters formed, according to Eq. (B-1), will depend on the two parameters E and $A\tau$. Fig. 24 shows the craters predicted by Eq. (B-1) for deposition of energy in iron targets, at various values of E and $A\tau$. Overlaid as dotted lines are analogous predictions for the craters formed by impact of iron projectiles of various sizes, striking at various speeds. As noted above, there is a one-to-one correspondence between impact speed and the power density at the impact point, and both of these are shown on the abscissa scale of this figure. The point to be noted is that any experimental technique capable of driving shock waves of strength greater than 10^{11} watts/cm^2 can simulate impact conditions which are presently beyond the capability of conventional projection techniques. One energy source that immediately suggests itself for such an application is the laser. By focussing the beam from such a device, power densities of 10^{13} watts/cm^2, delivered in less than a microsecond, can be achieved(30) with existing equipment. The fact that the maximum output of these devices is currently being improved at such a rapid rate indicates that simulation by a laser beam is a promising experimental technique.

The calculations presented in Fig. 24 to illustrate the simulation possibilities start from the hypothesis that the energy absorption takes place by means of a blast wave mechanism. Particularly in the case of electromagnetic energy deposition, this assumption needs careful scrutiny. There would appear to be little doubt that is is the correct mechanism when the rate of energy input is sufficiently high. Certainly, the different phenomena brought into play, at one extreme, by striking a match and, at the other, by detonating a nuclear bomb, provide evidence that the mechanism of energy absorption changes, at some point, from one of linear heat conduction to the nonlinear shock-wave mechanism. Exactly where such a transition will occur in solid media is not presently known, although it is presumably amenable to theoretical analysis. The conclusions reached above are based on the assumption that a shock wave will be the correct mechanism whenever the incident power density exceeds 10^{11} watts/cm^2.

APPENDIX C

SOLUTION NEAR THE SONIC POINT

At the "sonic" point, two quantities must be zero:

$$(x^* - N)^2 - y^* = 0 \tag{C-1}$$

$$y^*\left(3x^* + z^* - \frac{2}{\gamma}[1-N]\right) - x^*(x^* - N)(x^* - 1) = 0 \tag{C-2}$$

The asterisk is used here and in the equations that follow to denote conditions at the sonic point. Because these quantities are zero, the values of dy/dx and $dx/d\eta$ are indeterminate, according to Eqs. (A-12) and (A-10). To resolve the indeterminacy, put

$$y = y^*(1+\epsilon), \quad x = x^*(1+\delta), \quad z = z^*(1+\sigma) \tag{C-3}$$

and let

$$\left(\frac{dy}{dx}\right)^* \equiv k_1 \quad , \quad \left(\frac{dz}{dx}\right)^* \equiv k_2 \tag{C-4}$$

so that

$$\epsilon = k_1 \frac{x^*}{y^*}\,\delta \quad , \quad \sigma = k_2 \frac{x^*}{z^*}\,\delta \tag{C-5}$$

While all three of x^*, y^* and z^* appear in these equations, it should be noted that only two of them are independent, since (C-1) and (C-2) must hold simultaneously.

By using Eq. (C-3), the expression for $(dy/dx)^*$ may be written as

$$\frac{k_1}{x^* - N} = -(\gamma - 1) + \frac{\left[2 - (\gamma-1)z^* - (3\gamma - 1)x^*\right]\left[2(x^* - N) - k_1\right]}{(x^* - N)^2(3 + k_2) + k_1\left[3x^* + z^* - \frac{2}{\gamma}(1-N)\right] - \left[3x^{*2} - 2(N+1)x^* + N\right]} \tag{C-6}$$

A second relation between k_1 and k_2 may be found from

$$k_2 = \left(\frac{dz}{dx}\right)^* = \frac{(dz/d\ln\eta)^*}{(dx/d\ln\eta)^*}$$

$$= \frac{\left[z^*\left(1-\frac{z^*}{2}-2x^*\right)-2y^*_{\theta\theta}\right]\left[2(x^*-N)-k_1\right]}{(x^*-N)\left\{(x^*-N)^2(3+k_2)+k_1\left(3x^*+z^*-\frac{2}{\gamma}[1-N]\right)-\left(3x^{*2}-2[N+1]x^*+N\right)\right\}} \qquad \text{(C-7)}$$

Thus, (C-6) may be written as

$$\frac{k_1}{x^*-N} = -(\gamma-1)+\frac{\left[2-(\gamma-1)z^*-3(\gamma-1)x^*\right](x^*-N)}{z^*\left(1-\frac{z^*}{2}-x^*\right)-2y^*_{\theta\theta}} \qquad \text{(C-8)}$$

which gives a linear relation between k_1 and k_2. Using this relation in (C-6) then gives a quadratic for k_1 :

$$Ak_1^2+Bk_1+C=0 \qquad \text{(C-9)}$$

where

$$A = F_5 + F_{10} \qquad \text{(C-10)}$$

$$B = F_9 - F_6 - F_1F_5 + F_2 - F_1F_{10} \qquad \text{(C-11)}$$

$$C = -F_1F_9 + F_1F_6 - F_2F_3 \qquad \text{(C-12)}$$

$$F_1 = -(\gamma-1)(x^*-N) \qquad \text{(C-13)}$$

$$F_2 = (x^*-N)\left[2-(\gamma-1)z^*-(3\gamma-1)x^*\right] \qquad \text{(C-14)}$$

$$F_3 = 2(x^*-N) \qquad \text{(C-15)}$$

$$F_5 = 3x^*+z^*-\frac{2}{\gamma}(1-N) \qquad \text{(C-16)}$$

$$F_6 = 3x^{*2}-2(N+1)x^*+N \qquad \text{(C-17)}$$

$$F_9 = 3(x^*-N)^2 + (x^*-N)(\gamma-1)\;\frac{z^*\left(1-\frac{z^*}{2}-x^*\right)-2\,y^*_{\theta\theta}}{2-(\gamma-1)\,z^*-(3\gamma-1)\,x^*} \tag{C-18}$$

$$F_{10} = \frac{z^*\left(1-\frac{z^*}{2}-x^*\right)-2\,y^*_{\theta\theta}}{2-(\gamma-1)\,z^*-3(\gamma-1)\,x^*} \tag{C-19}$$

Having k_1 and k_2, one can now find

$$\eta^*\left(\frac{dx}{d\eta}\right)^* = \frac{(x^*-N)^2(3+k_2)+k_1\left(3x^*+z^*-\frac{2}{\gamma}\,[1-N]\right)-F_6}{2\,(x^*-N)-k_1} \tag{C-20}$$

$$\left(\frac{d\psi}{d\eta}\right)^* = -\;\frac{\eta^*\left(\frac{dx}{d\eta}\right)^*+3\,x^*+z^*}{(x^*-N)\;\frac{\eta^*}{\psi^*}} \tag{C-21}$$

$$\left(\frac{d\phi}{d\eta}\right)^* = \phi^*\left[\frac{1}{x^*}\left(\frac{dx}{d\eta}\right)^*+\frac{1}{\eta^*}\right] \tag{C-22}$$

$$\left(\frac{d\tau}{d\eta}\right)^* = \frac{\frac{1}{2}\,\frac{1-N}{N}\,\tau^*-\frac{\tau^{*2}}{4\eta^*}-\frac{\phi^*\tau^*}{2\eta^*}-\frac{1}{\eta^*\psi^*}\left(\frac{\partial^2 f}{\partial\theta^2}(\eta,0)\right)^*}{\frac{1}{2}(\phi^*-\eta^*)} \tag{C-23}$$

$$\left(\frac{df}{d\eta}\right)^* = f^*\left\{\frac{1}{y^*}\,\frac{k_1}{(d\eta/dx)^*}+\frac{2}{\eta^*}+\frac{1}{\psi^*}\left(\frac{d\psi}{d\eta}\right)^*\right\} \tag{C-24}$$

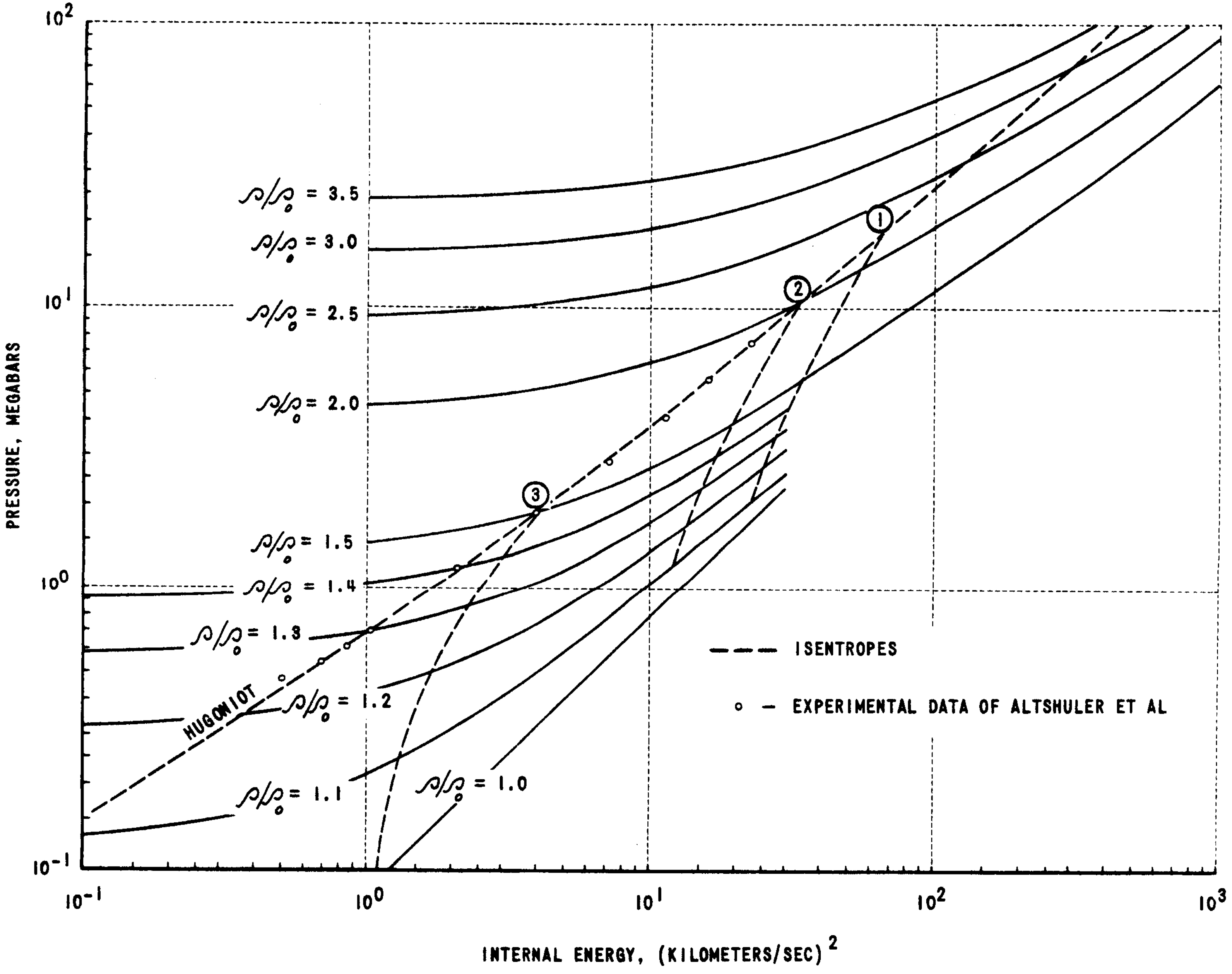

Figure 1 EQUATION OF STATE OF IRON

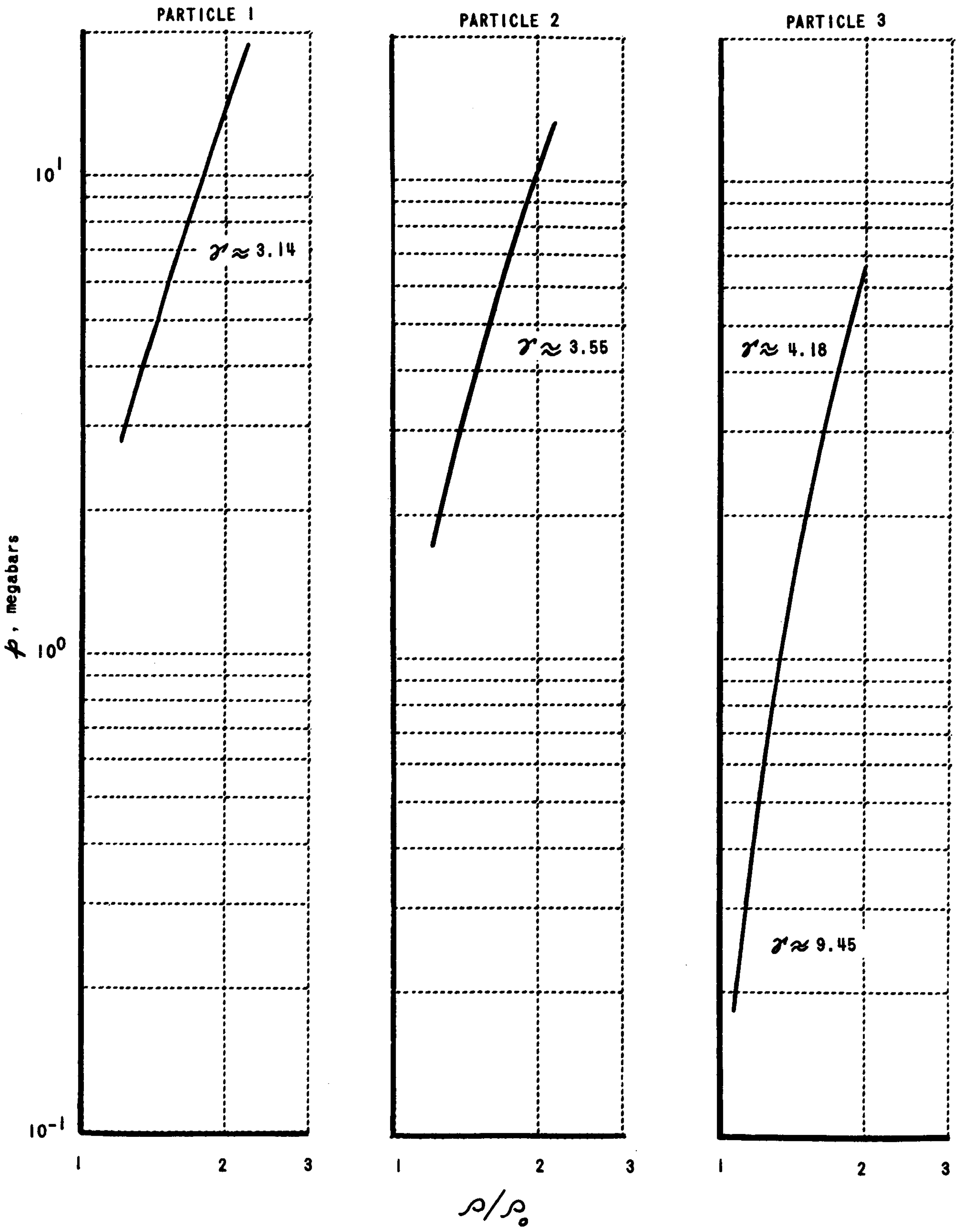

Figure 2 TYPICAL ISENTROPES OF IRON

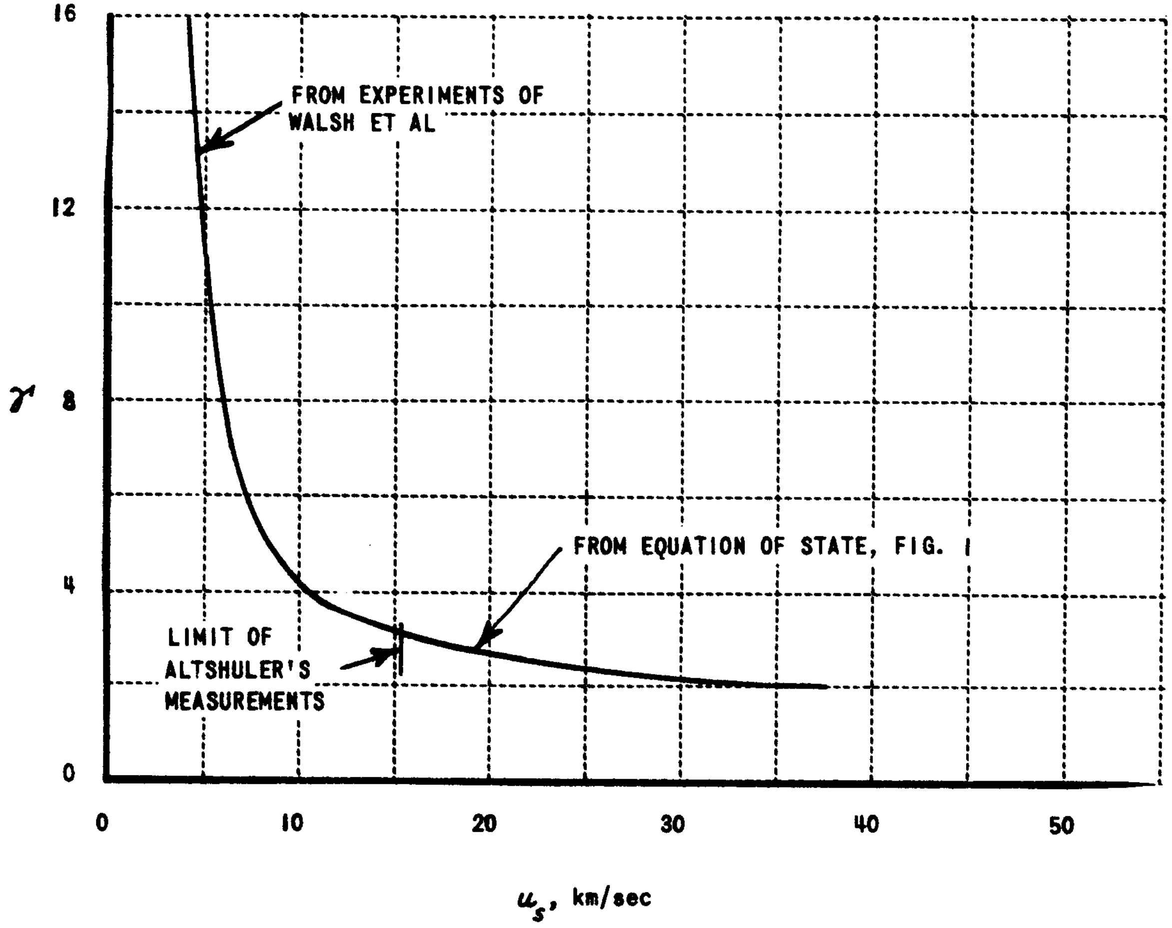

Figure 3 EFFECTIVE γ' FOR NORMAL SHOCK WAVES IN IRON

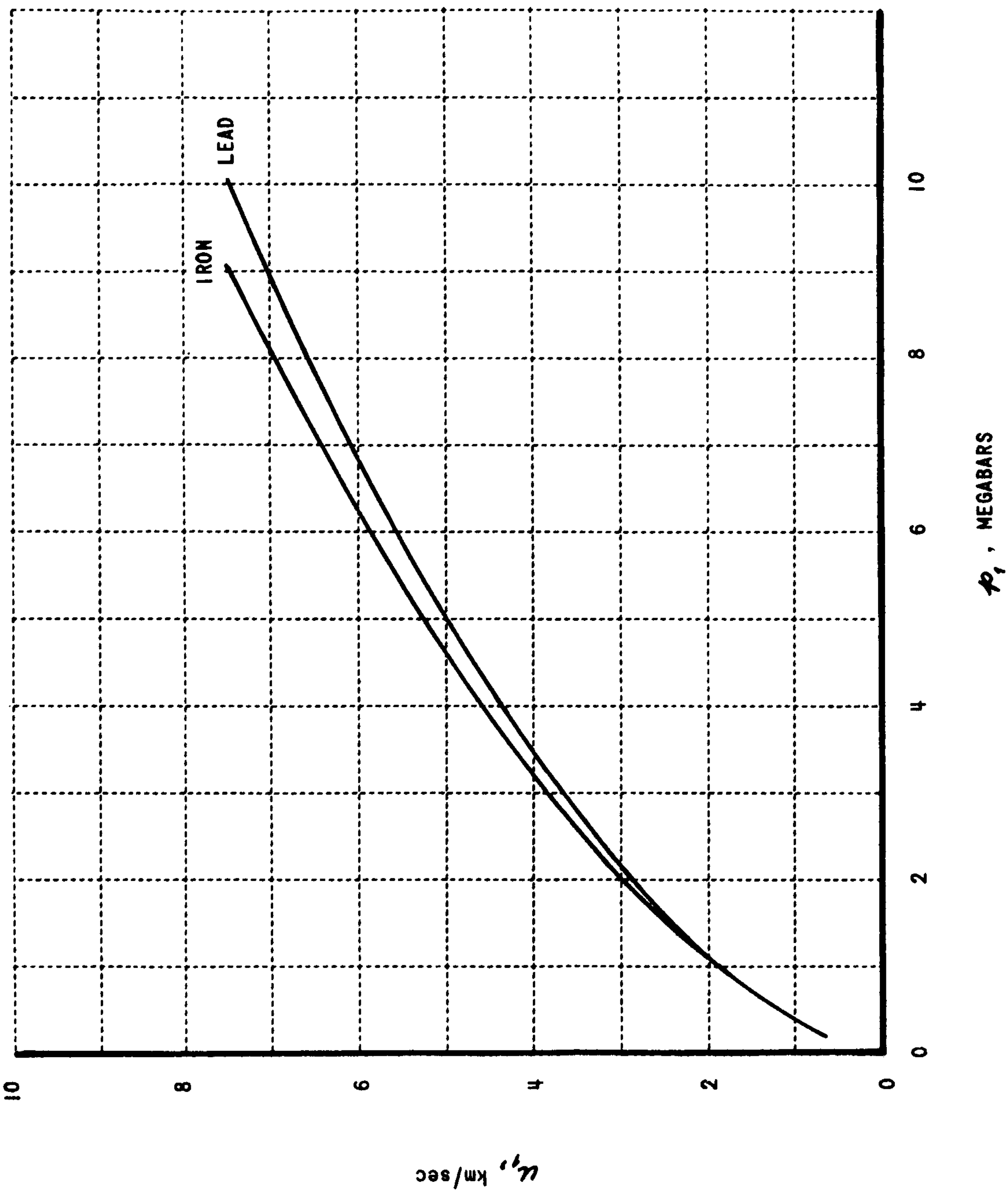

Figure 4 HUGONIOT CURVES FOR IRON AND LEAD, AFTER ALTSHULER ET AL

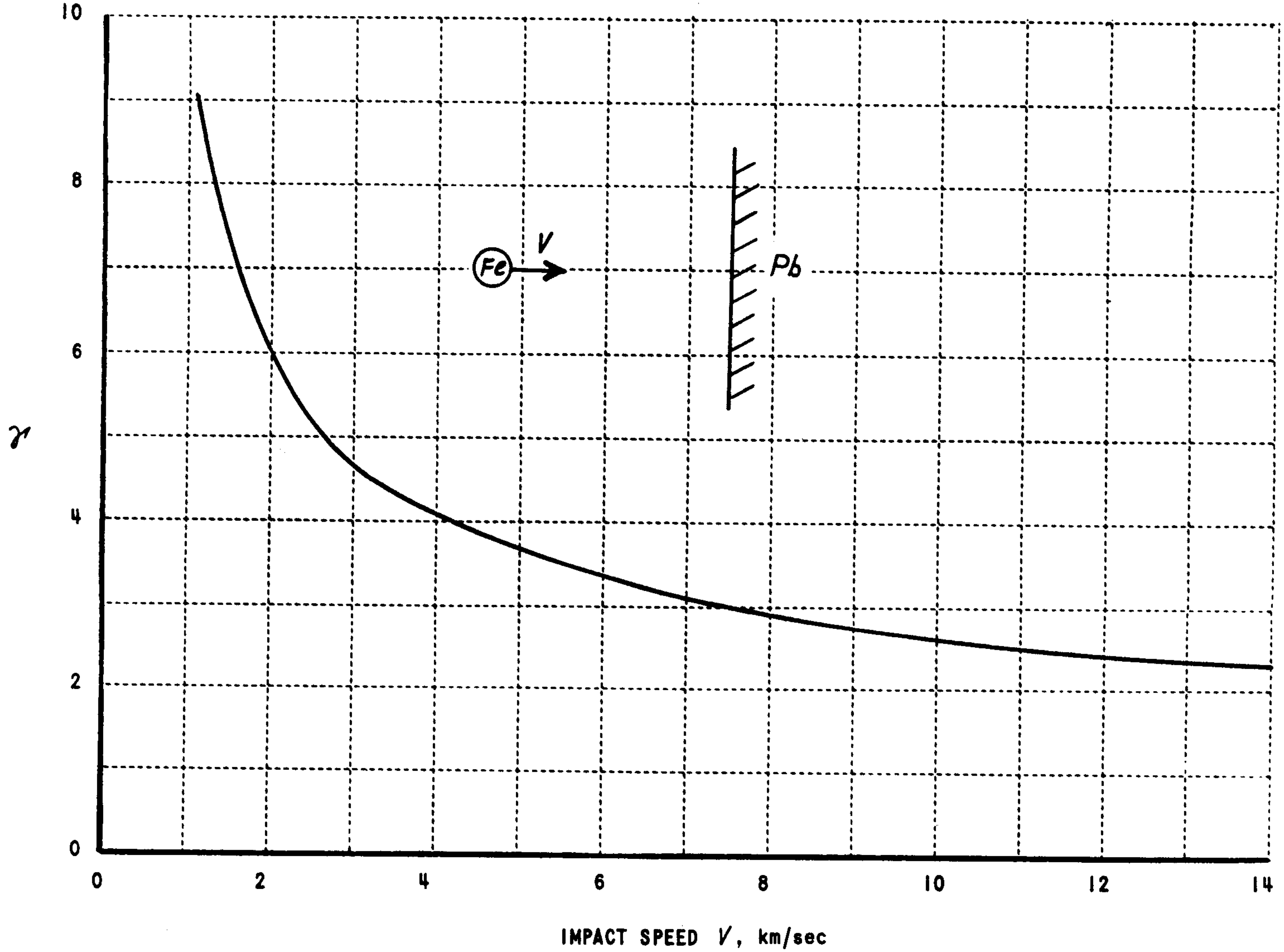

Figure 5 EFFECTIVE γ FOR LEAD TARGETS STRUCK BY IRON

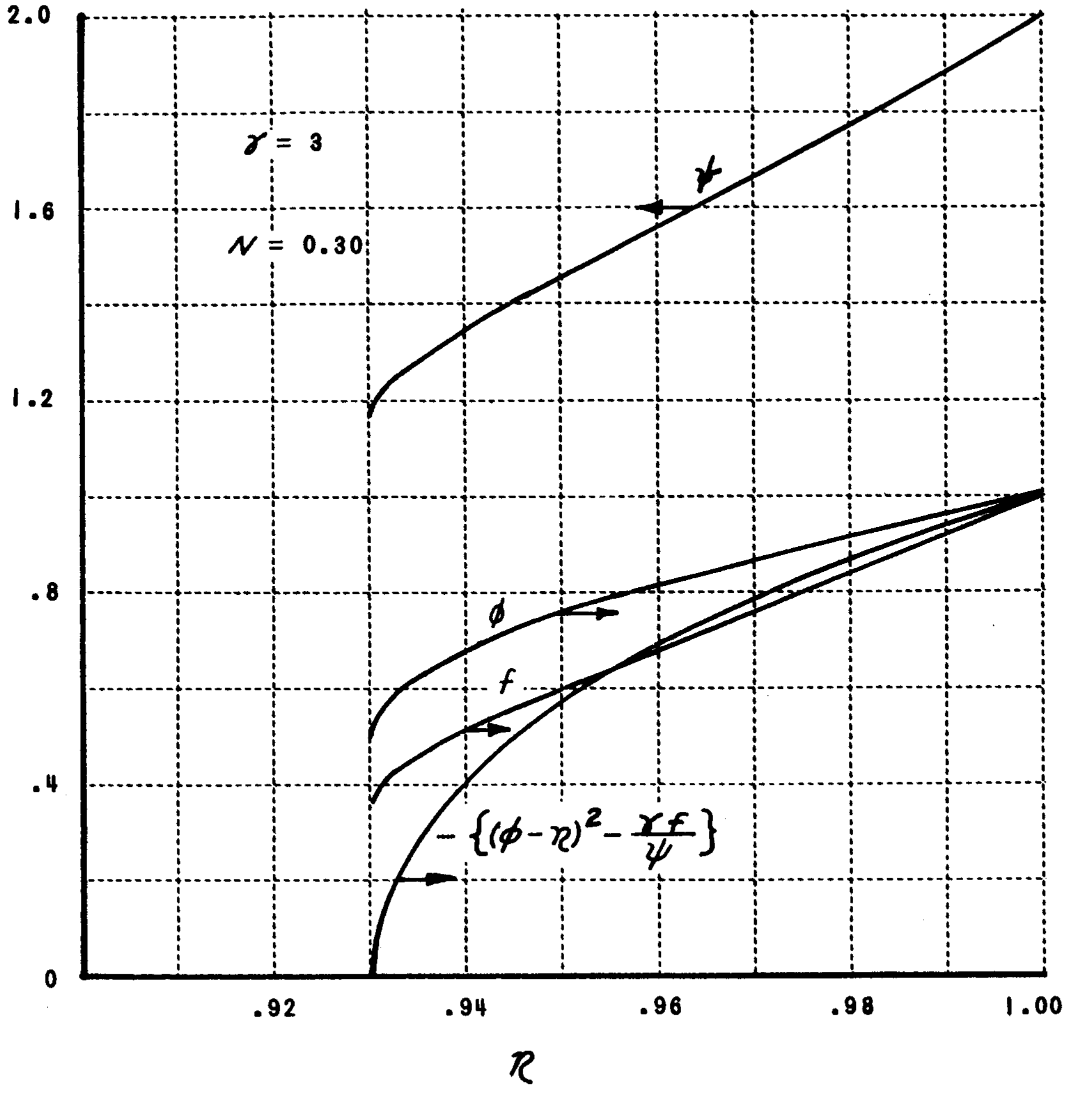

Figure 6 ATTEMPTED SPHERICALLY-SYMMETRIC SOLUTION, N = 0.30

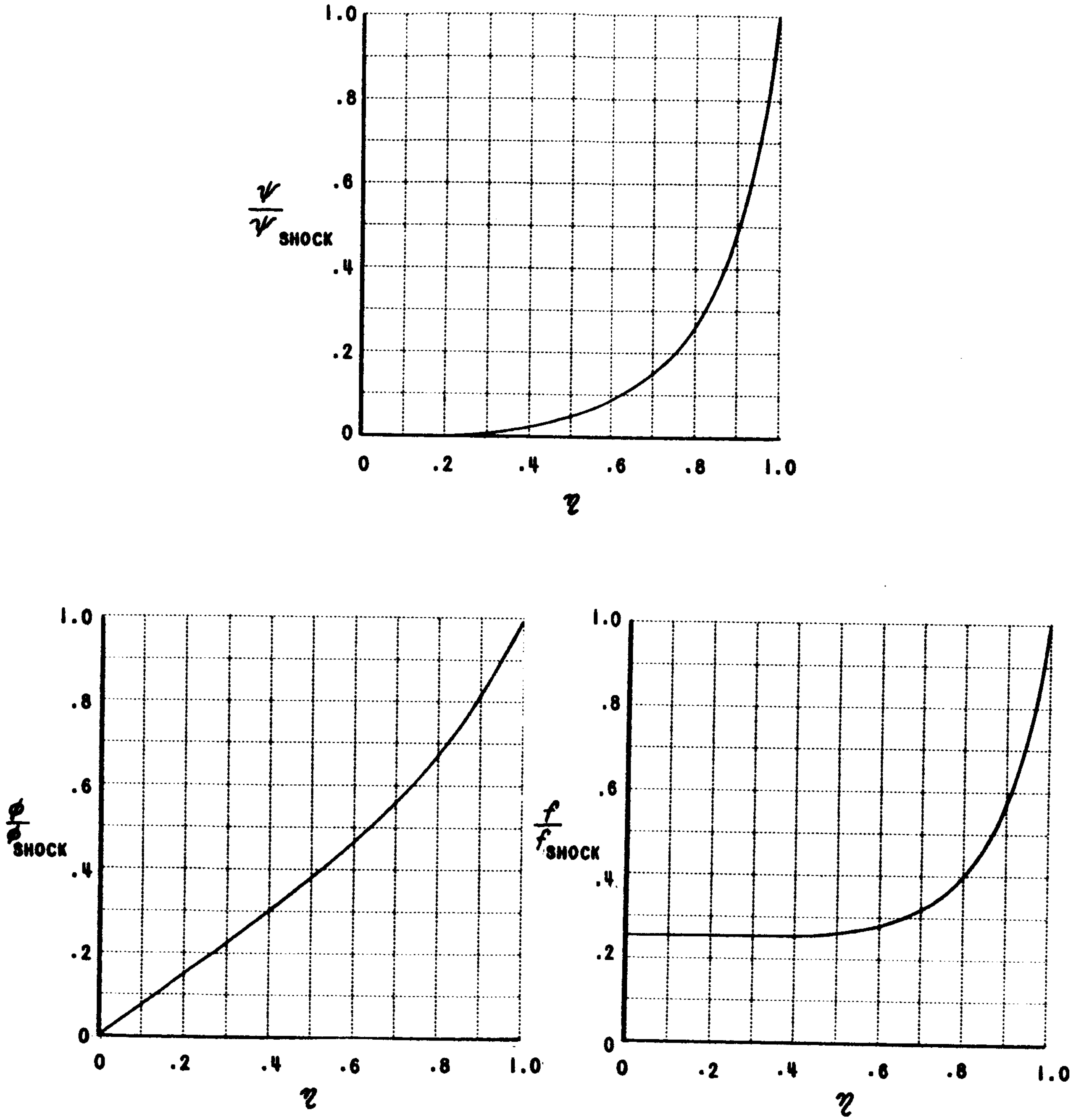

Figure 7a DISTRIBUTION OF DENSITY, PARTICLE VELOCITY, AND PRESSURE CONSTANT-ENERGY, SPHERICALLY-SYMMETRIC BLAST WAVES $\gamma = 2$

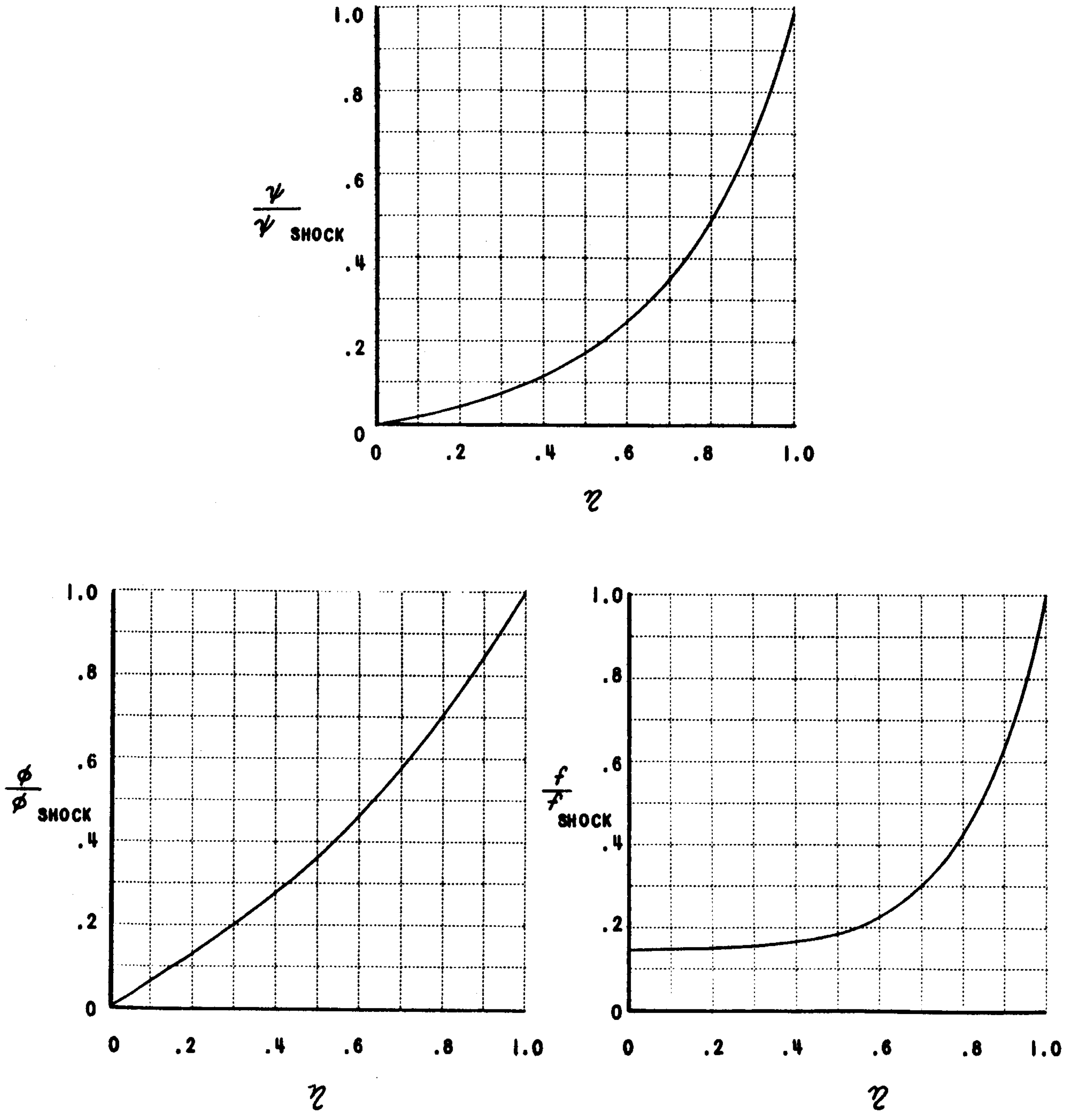

Figure 7b DISTRIBUTION OF DENSITY, PARTICLE VELOCITY, AND PRESSURE
CONSTANT-ENERGY, SPHERICALLY-SYMMETRIC BLAST WAVES
$\gamma' = 3$

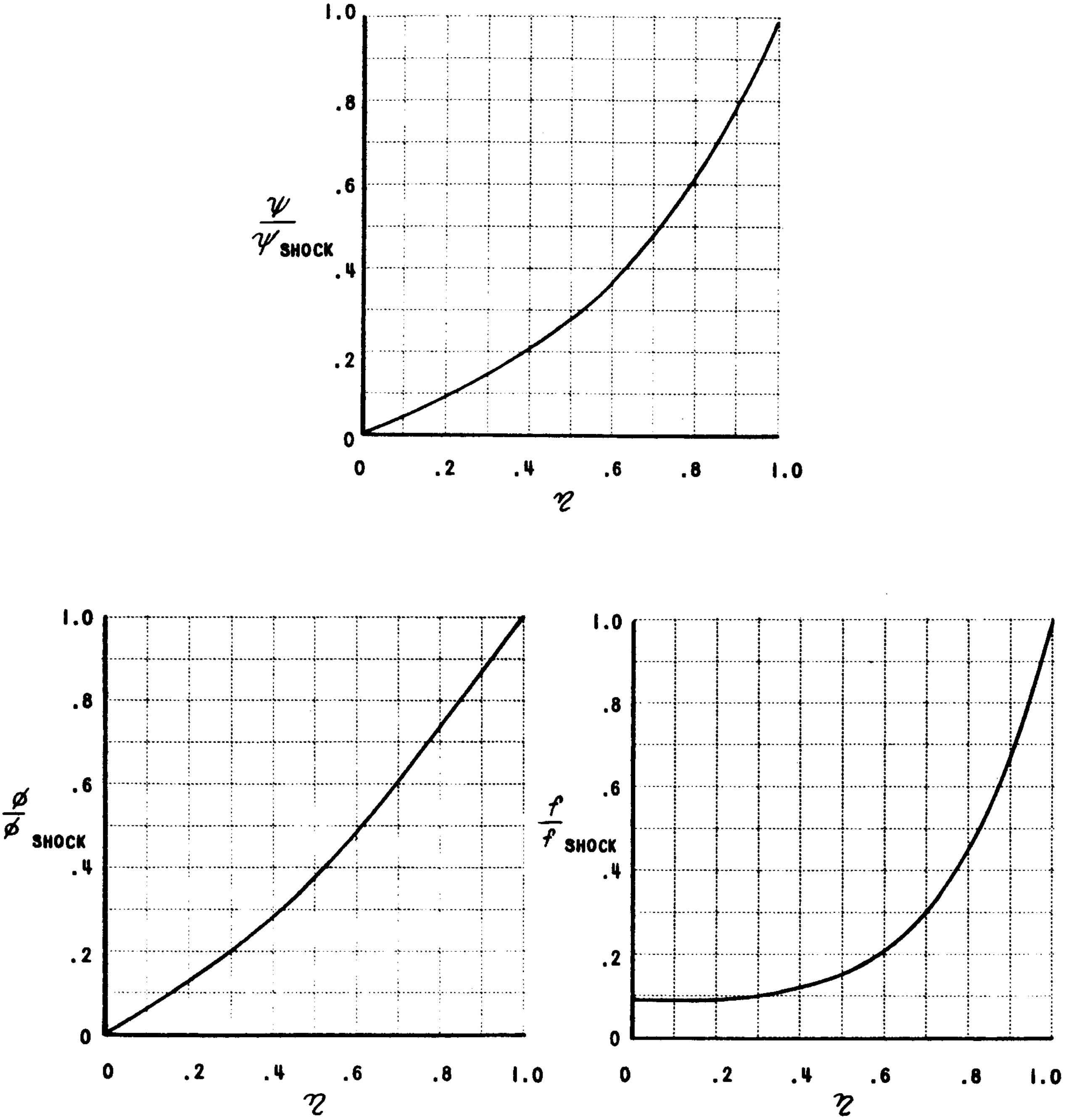

Figure 7c DISTRIBUTION OF DENSITY, PARTICLE VELOCITY, AND PRESSURE CONSTANT-ENERGY, SPHERICALLY-SYMMETRIC BLAST WAVES

$\gamma' = 4$

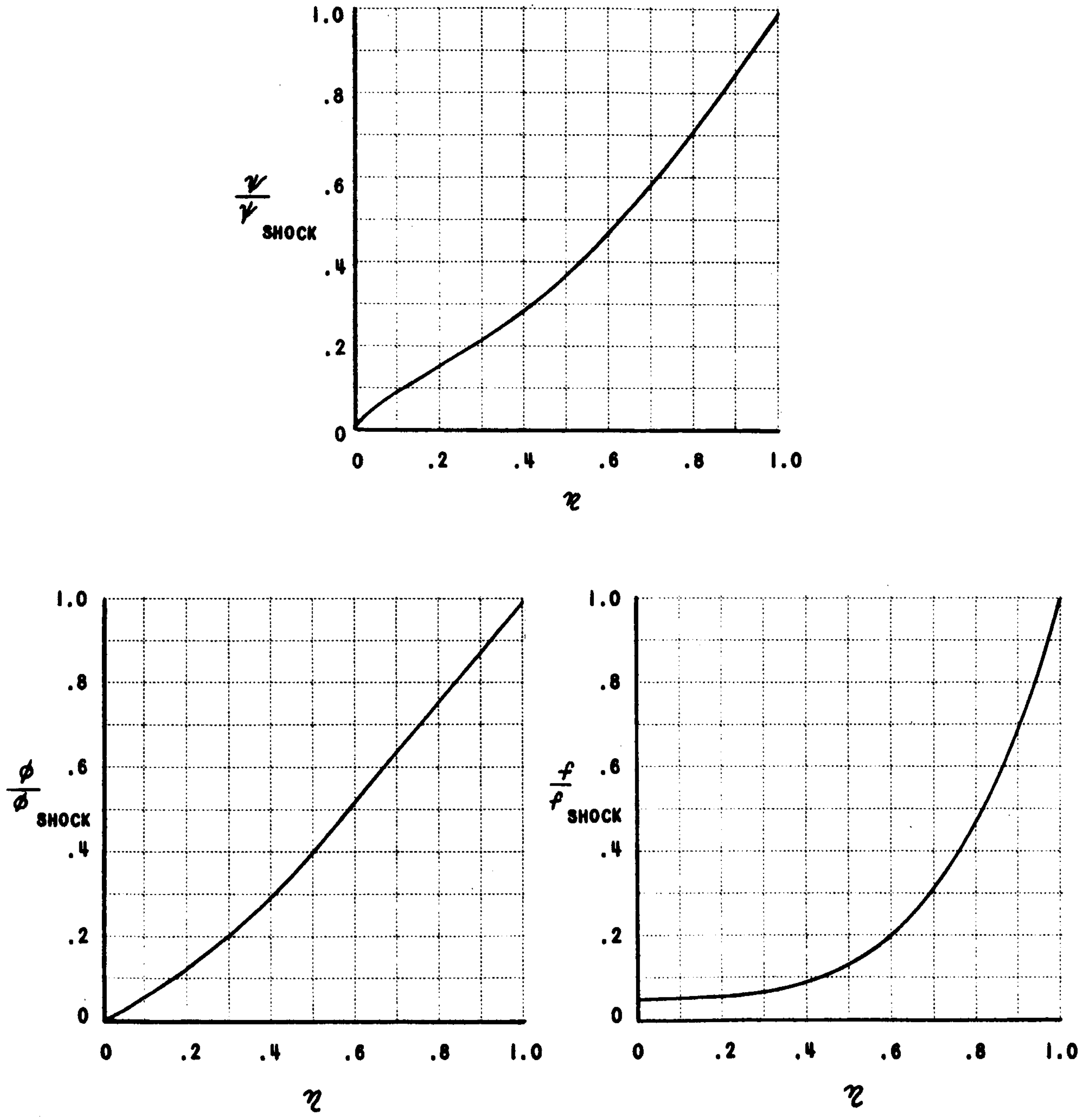

Figure 7d DISTRIBUTION OF DENSITY, PARTICLE VELOCITY, AND PRESSURE CONSTANT-ENERGY, SPHERICALLY-SYMMETRIC BLAST WAVES

$\gamma' = 5$

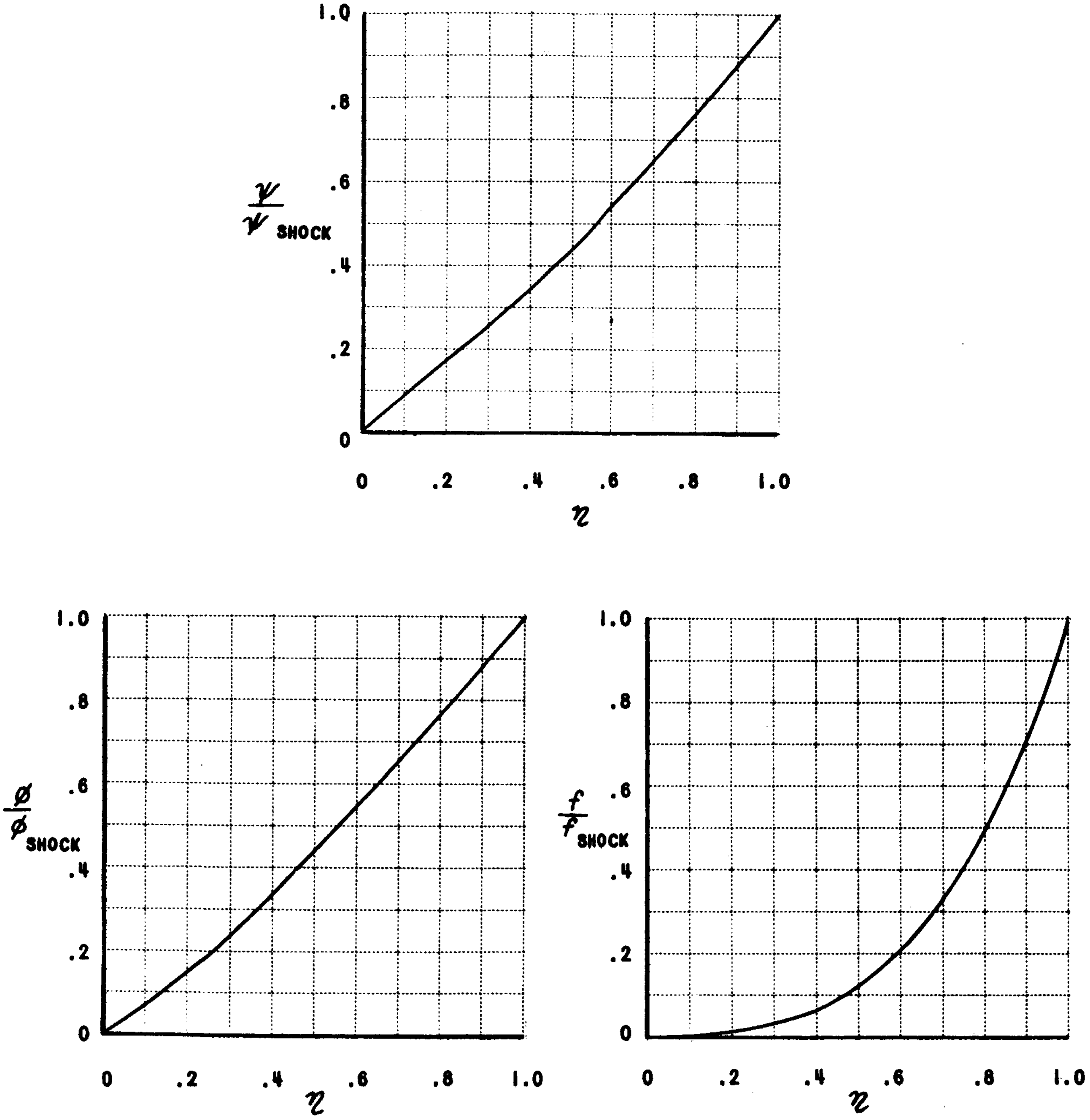

Figure 7e DISTRIBUTION OF DENSITY, PARTICLE VELOCITY, AND PRESSURE CONSTANT-ENERGY, SPHERICALLY-SYMMETRIC BLAST WAVES

$\gamma' = 6.0$

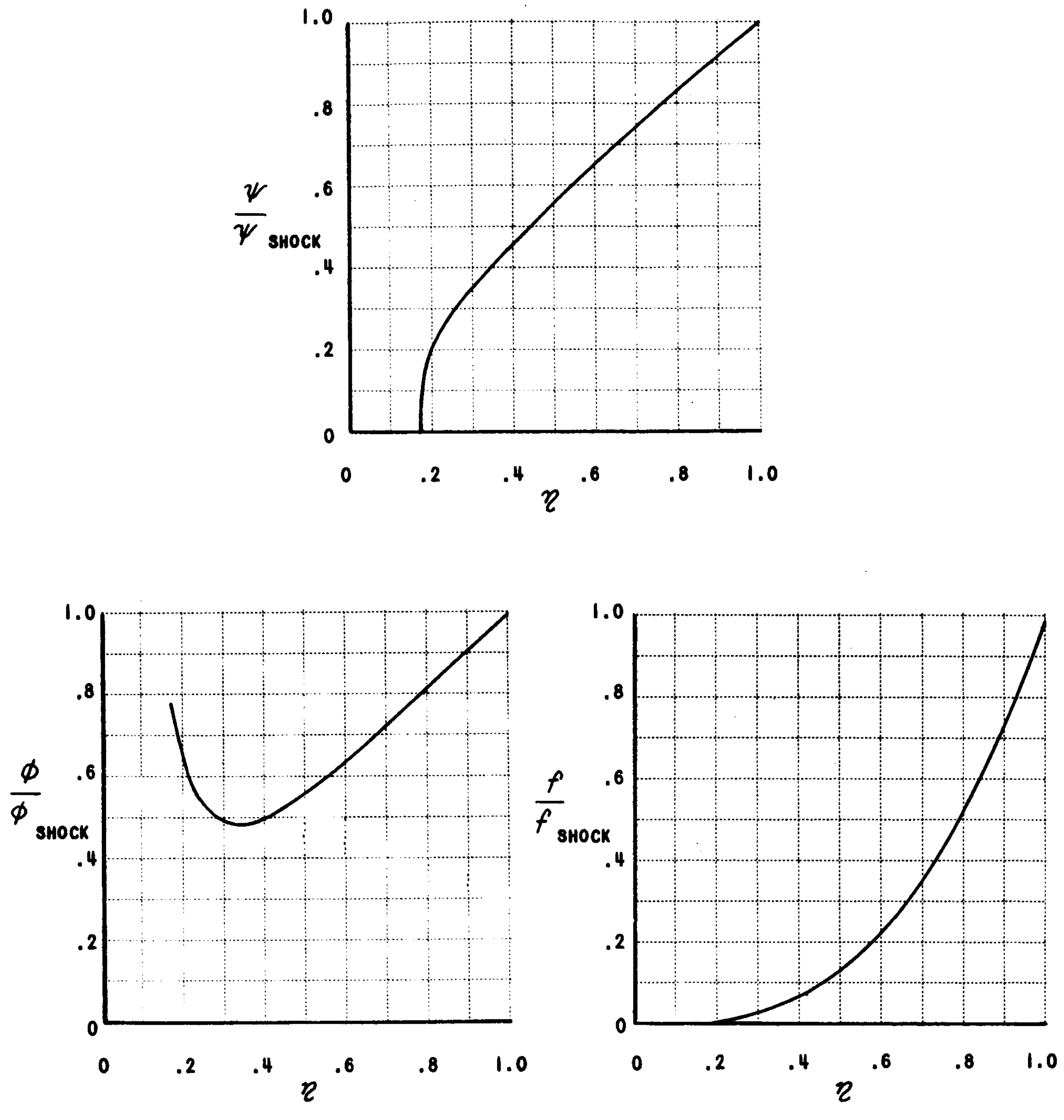

Figure 7f DISTRIBUTION OF DENSITY, PARTICLE VELOCITY, AND PRESSURE CONSTANT-ENERGY, SPHERICALLY-SYMMETRIC BLAST WAVES

$\gamma' = 8.0$

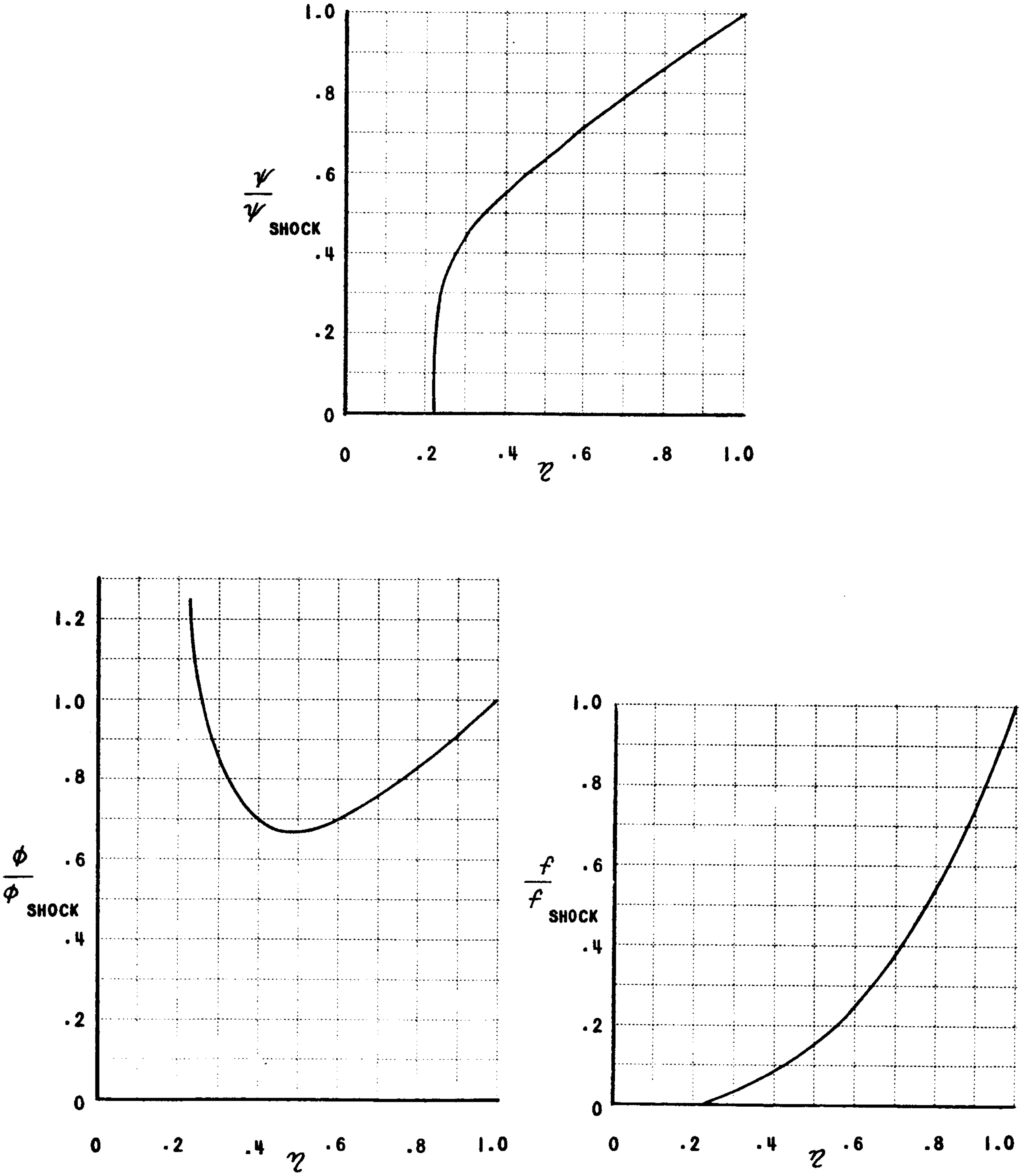

Figure 7g DISTRIBUTION OF DENSITY, PARTICLE VELOCITY, AND PRESSURE CONSTANT-ENERGY, SPHERICALLY-SYMMETRIC BLAST WAVES

$\gamma = 10$

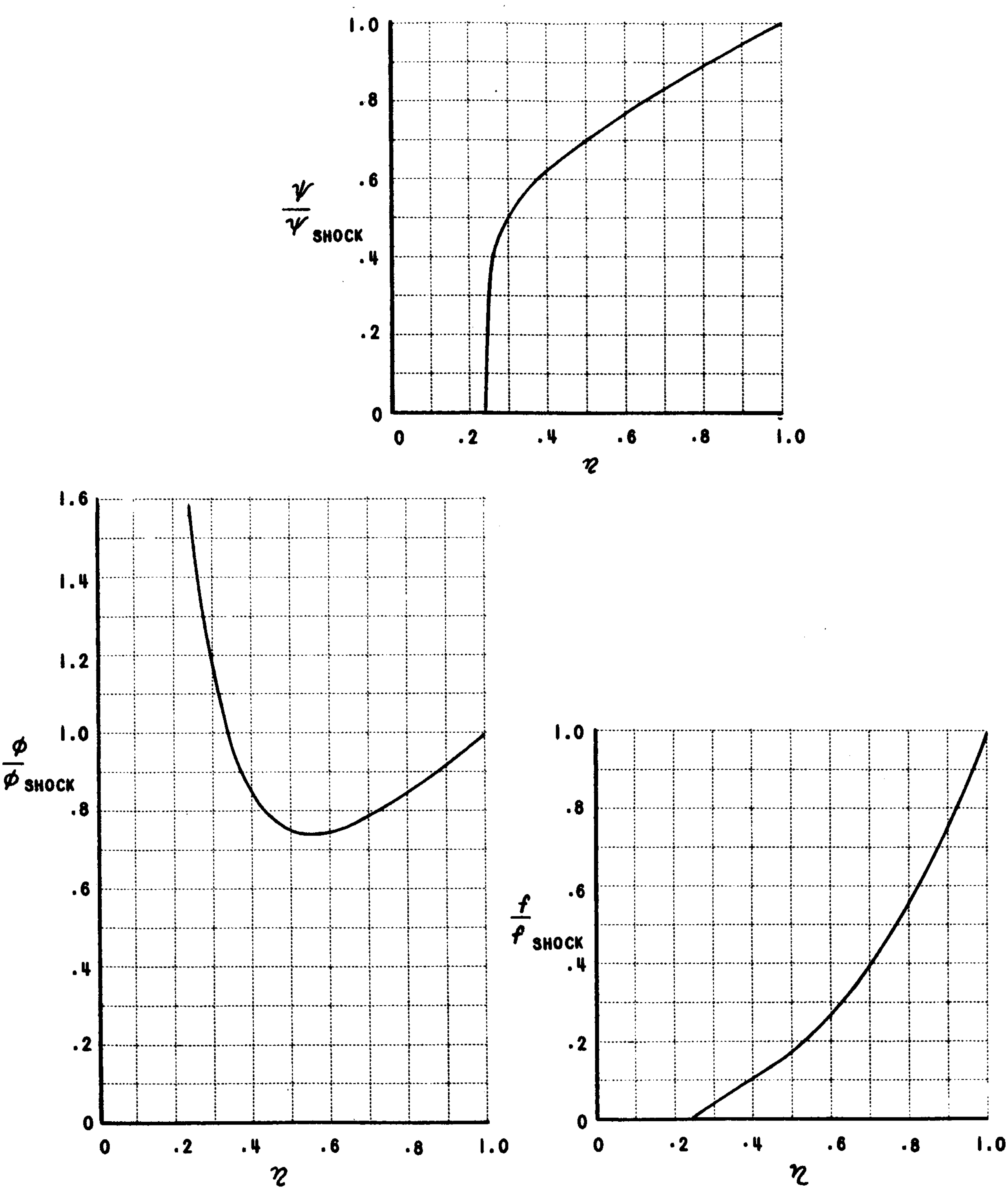

Figure 7h DISTRIBUTION OF DENSITY, PARTICLE VELOCITY, AND PRESSURE CONSTANT-ENERGY, SPHERICALLY-SYMMETRIC BLAST WAVES $\gamma' = 12$

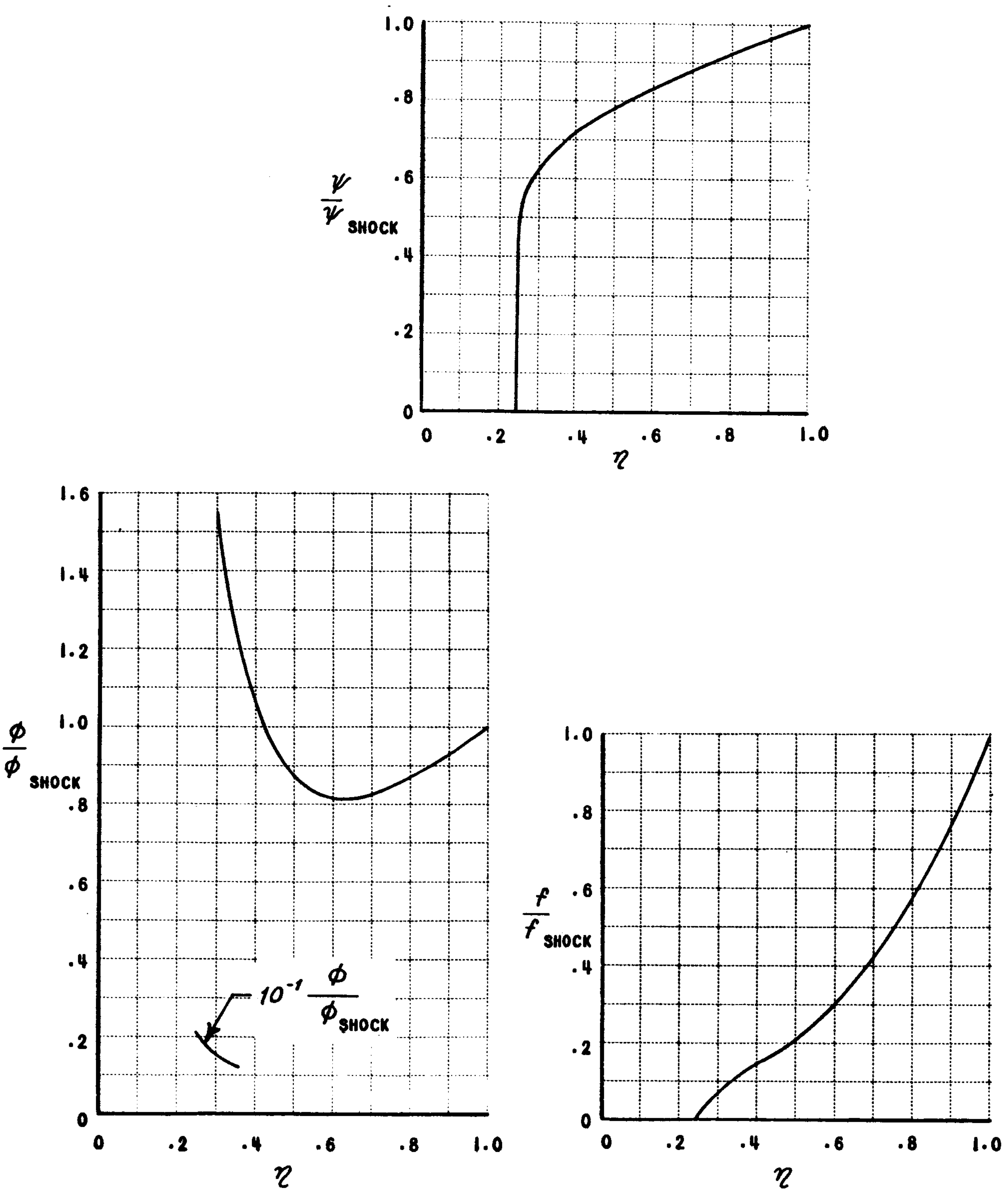

Figure 7i DISTRIBUTION OF DENSITY, PARTICLE VELOCITY, AND PRESSURE CONSTANT-ENERGY, SPHERICALLY-SYMMETRIC BLAST WAVES

$\gamma = 16$

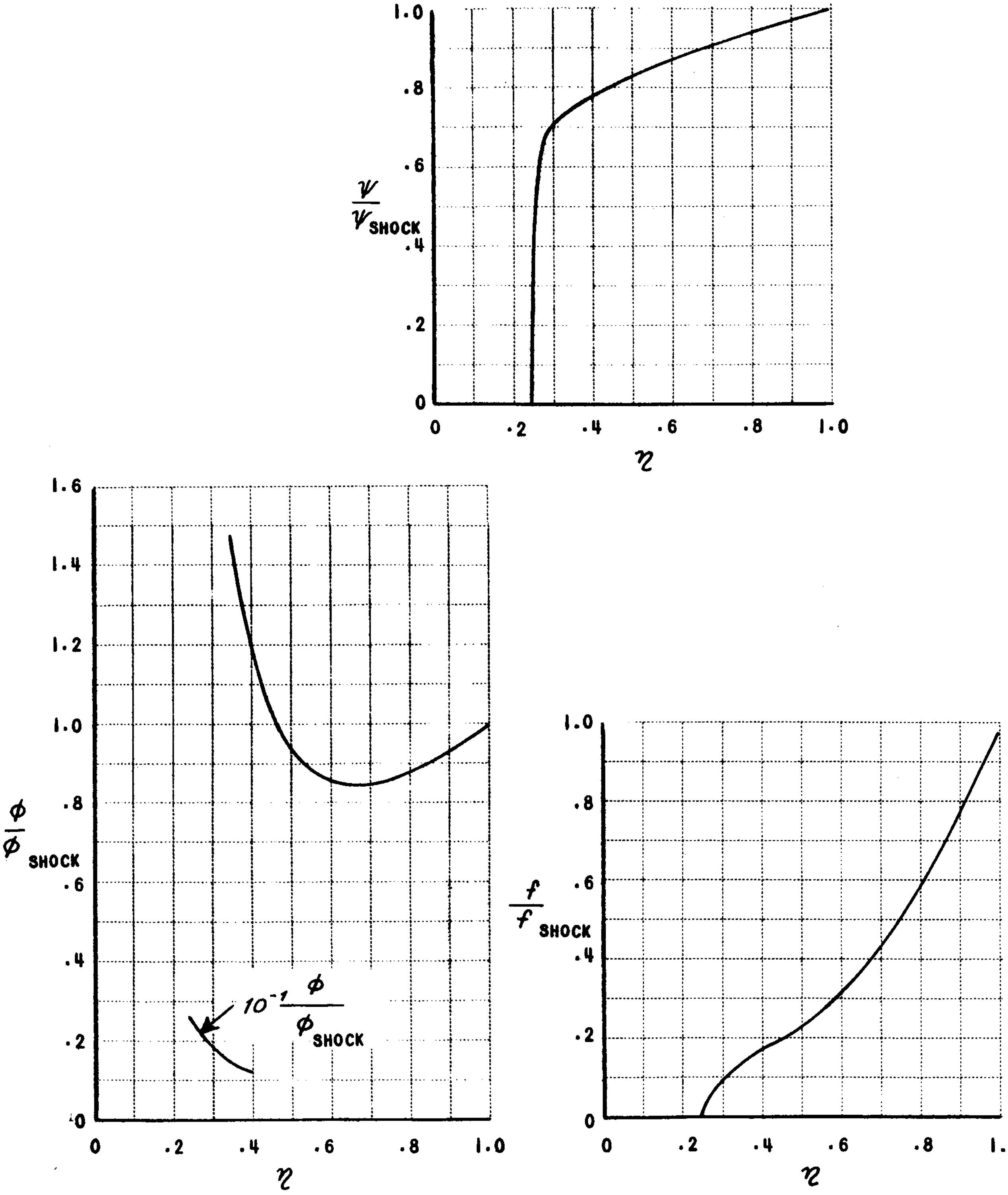

Figure 7j DISTRIBUTION OF DENSITY, PARTICLE VELOCITY, AND PRESSURE CONSTANT-ENERGY, SPHERICALLY-SYMMETRIC BLAST WAVES

$\gamma = 20$

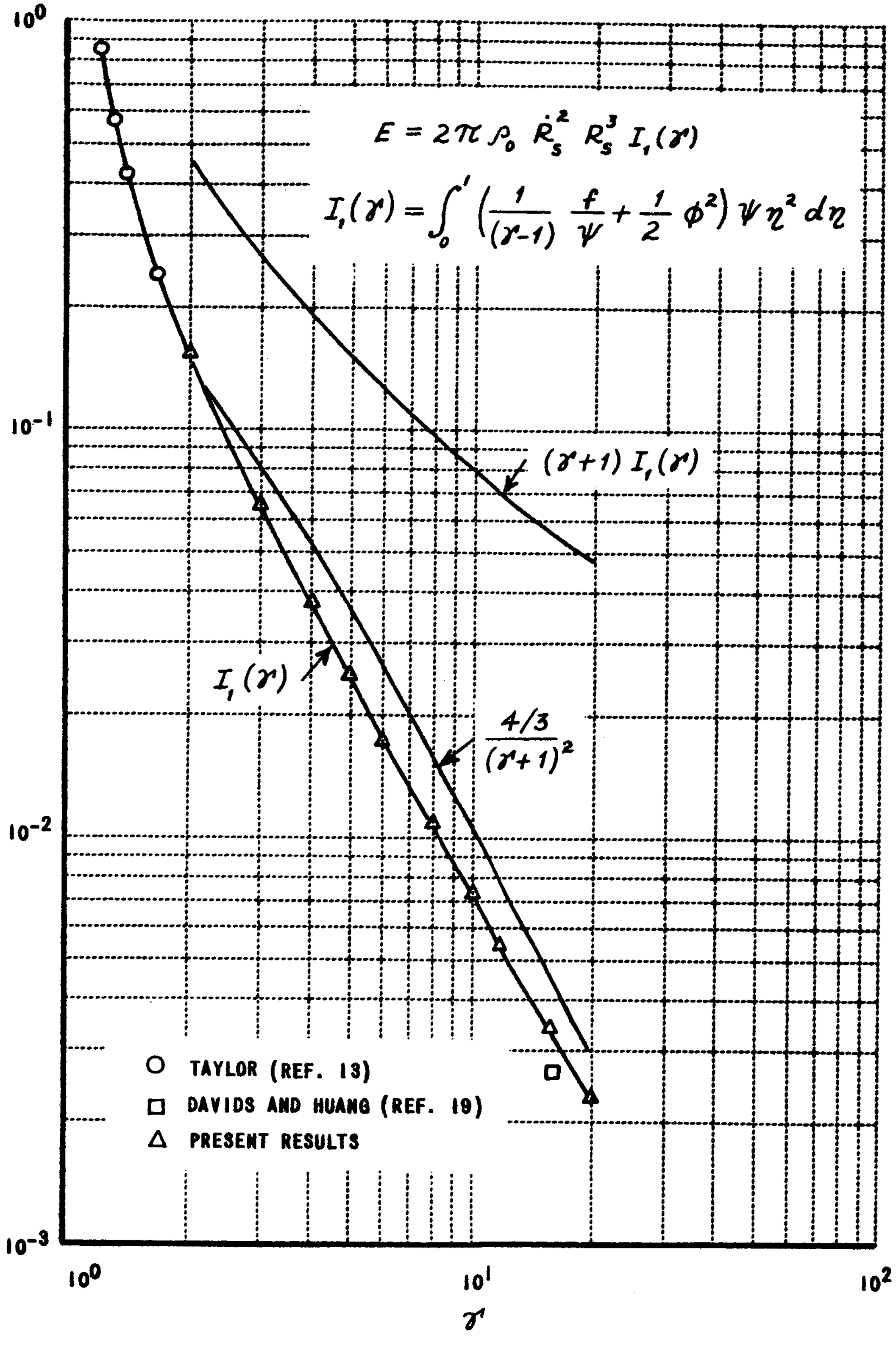

Figure 8 THE FUNCTION $I_1(\gamma)$ FOR SPHERICALLY-SYMMETRIC BLAST WAVES

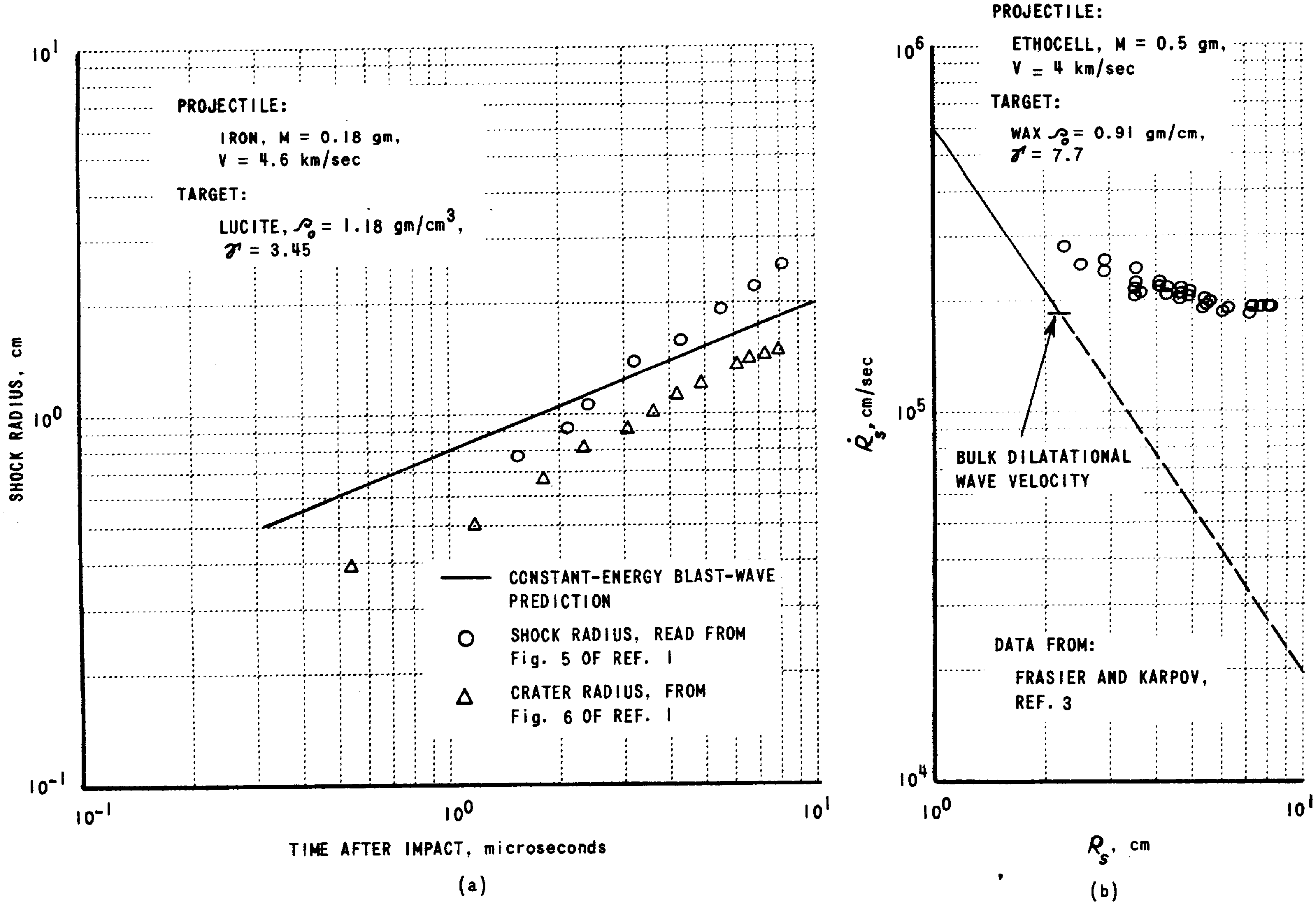

Figure 9 MEASURED SHOCK-WAVE TIME-HISTORY COMPARED WITH BLAST-WAVE PREDICTION

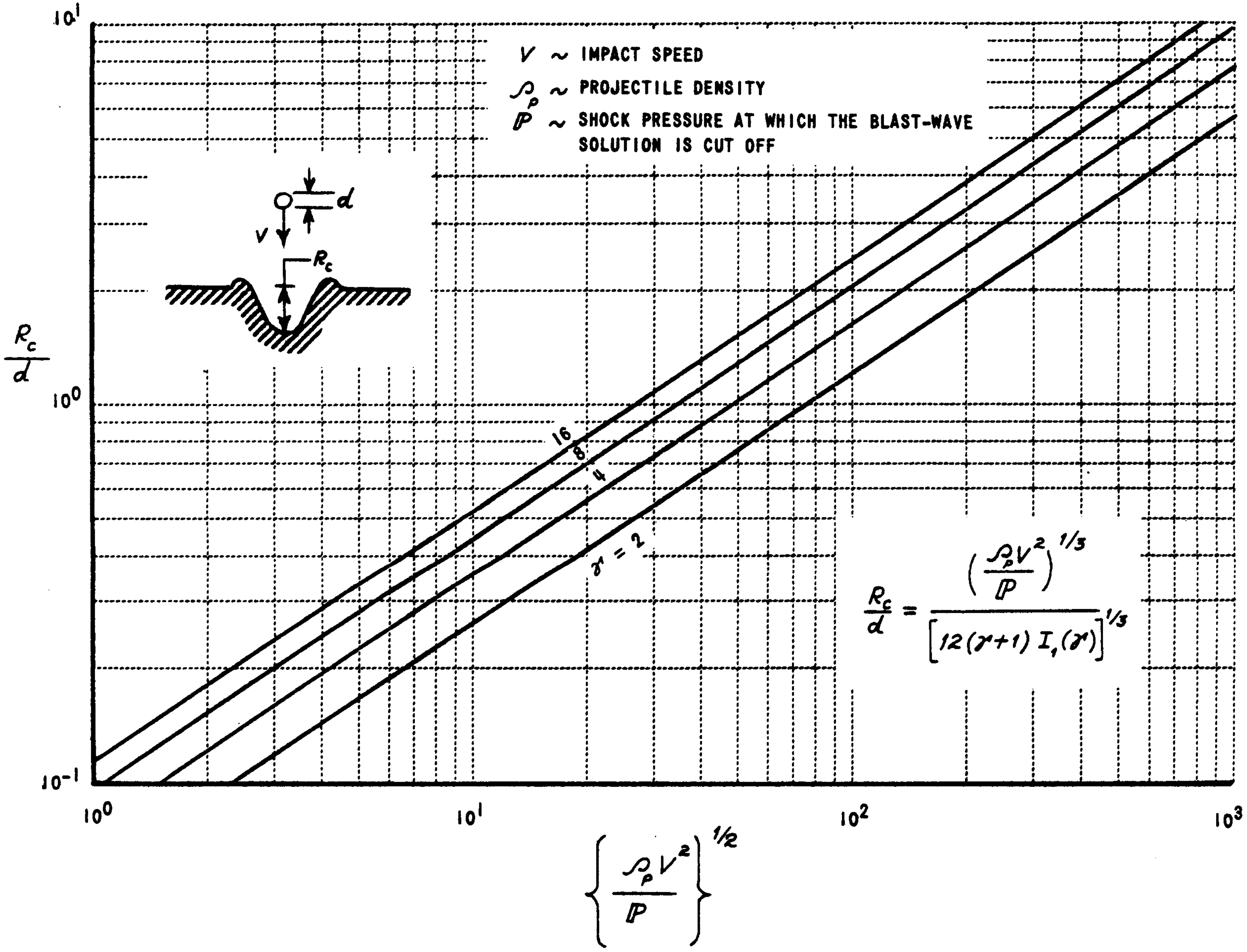

Figure 10 CONSTANT-ENERGY, EFFECTIVE-γ PREDICTION OF CRATER SIZE IN SEMI-INFINITE TARGETS

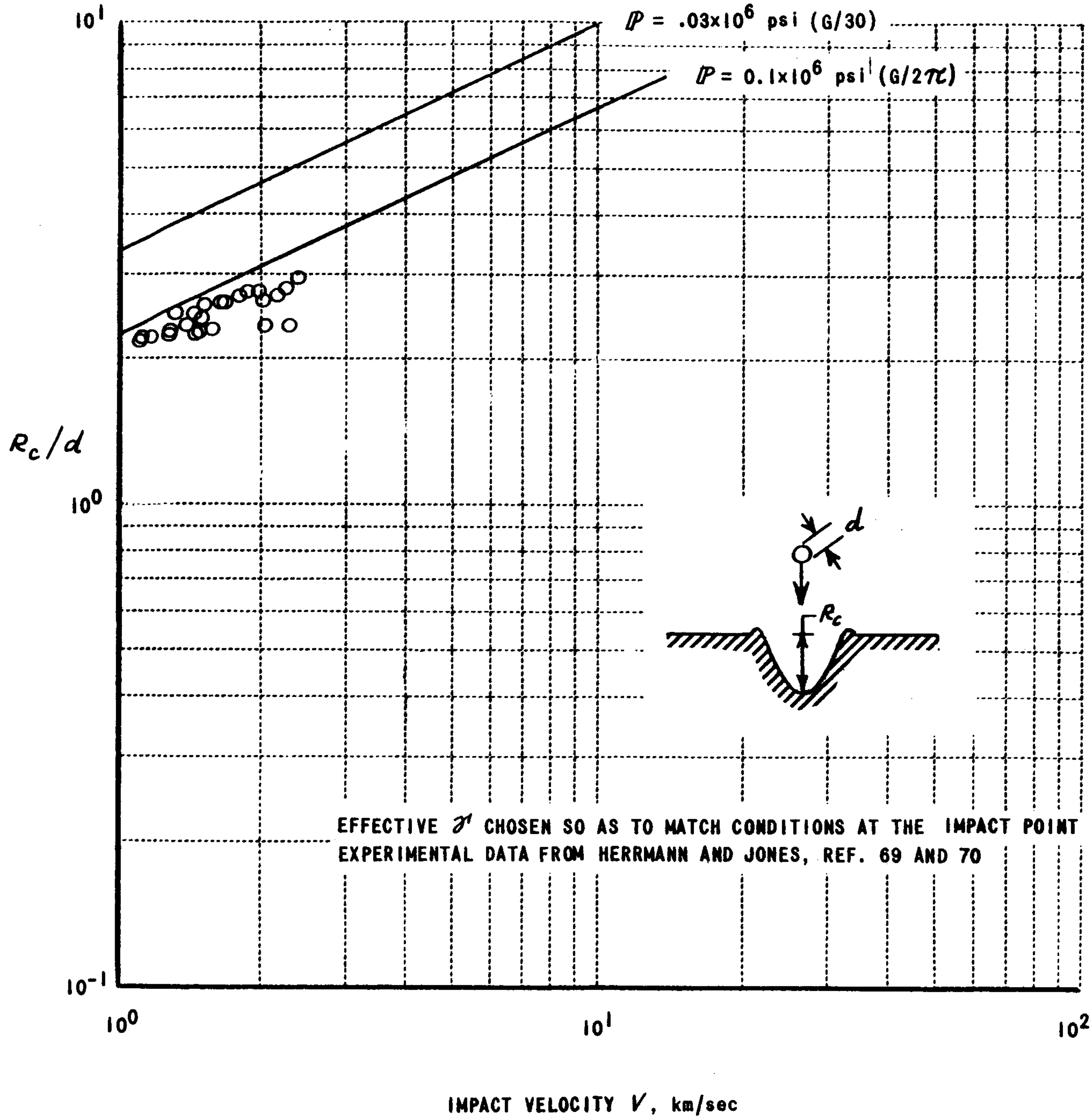

Figure 11 CONSTANT-ENERGY, EFFECTIVE-γ SOLUTION FOR CRATERS FORMED BY STEEL STRIKING LEAD

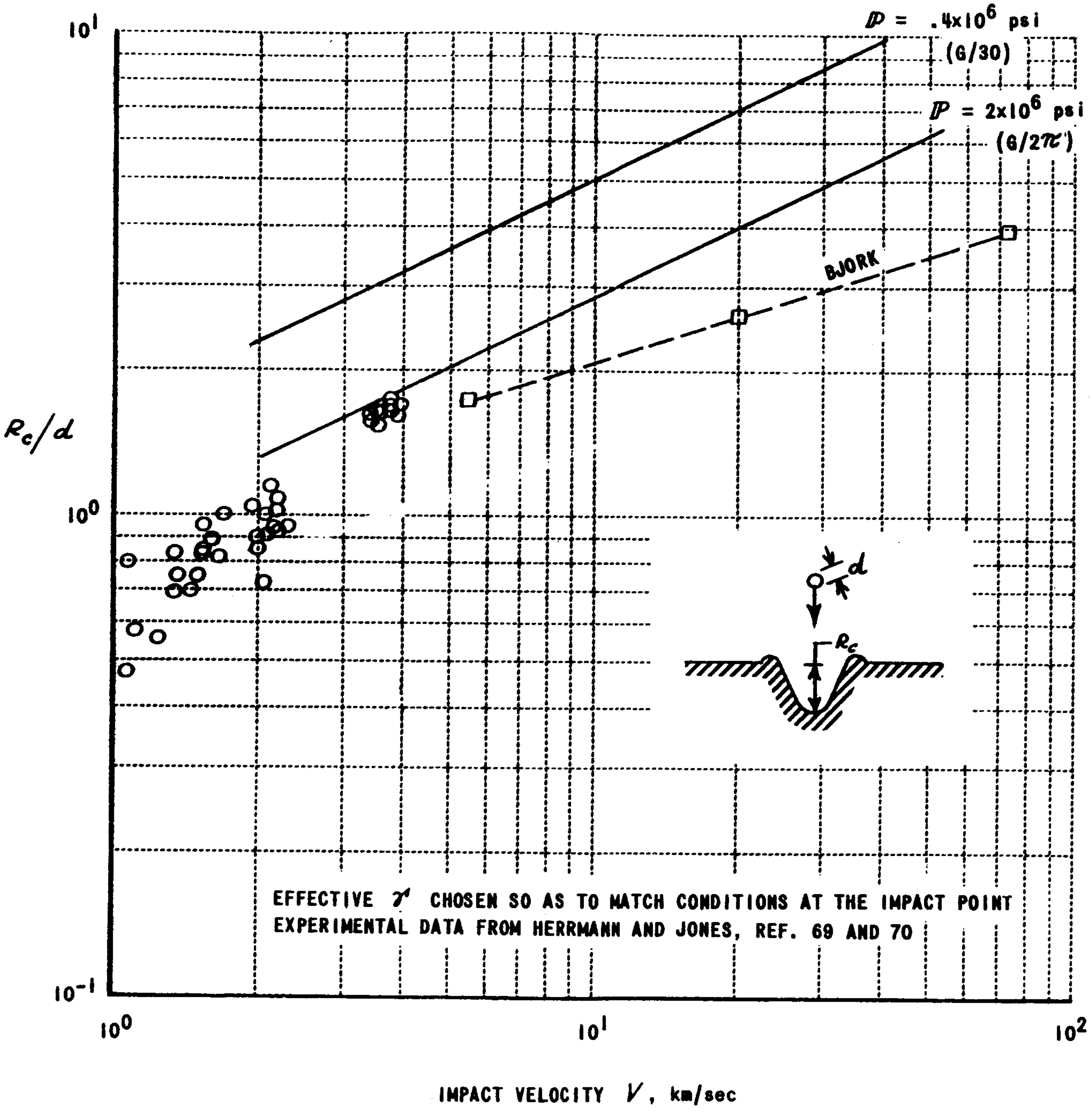

EFFECTIVE γ' CHOSEN SO AS TO MATCH CONDITIONS AT THE IMPACT POINT
EXPERIMENTAL DATA FROM HERRMANN AND JONES, REF. 69 AND 70

Figure 12 CONSTANT-ENERGY, EFFECTIVE-γ' SOLUTION FOR CRATERS FORMED BY IRON STRIKING IRON

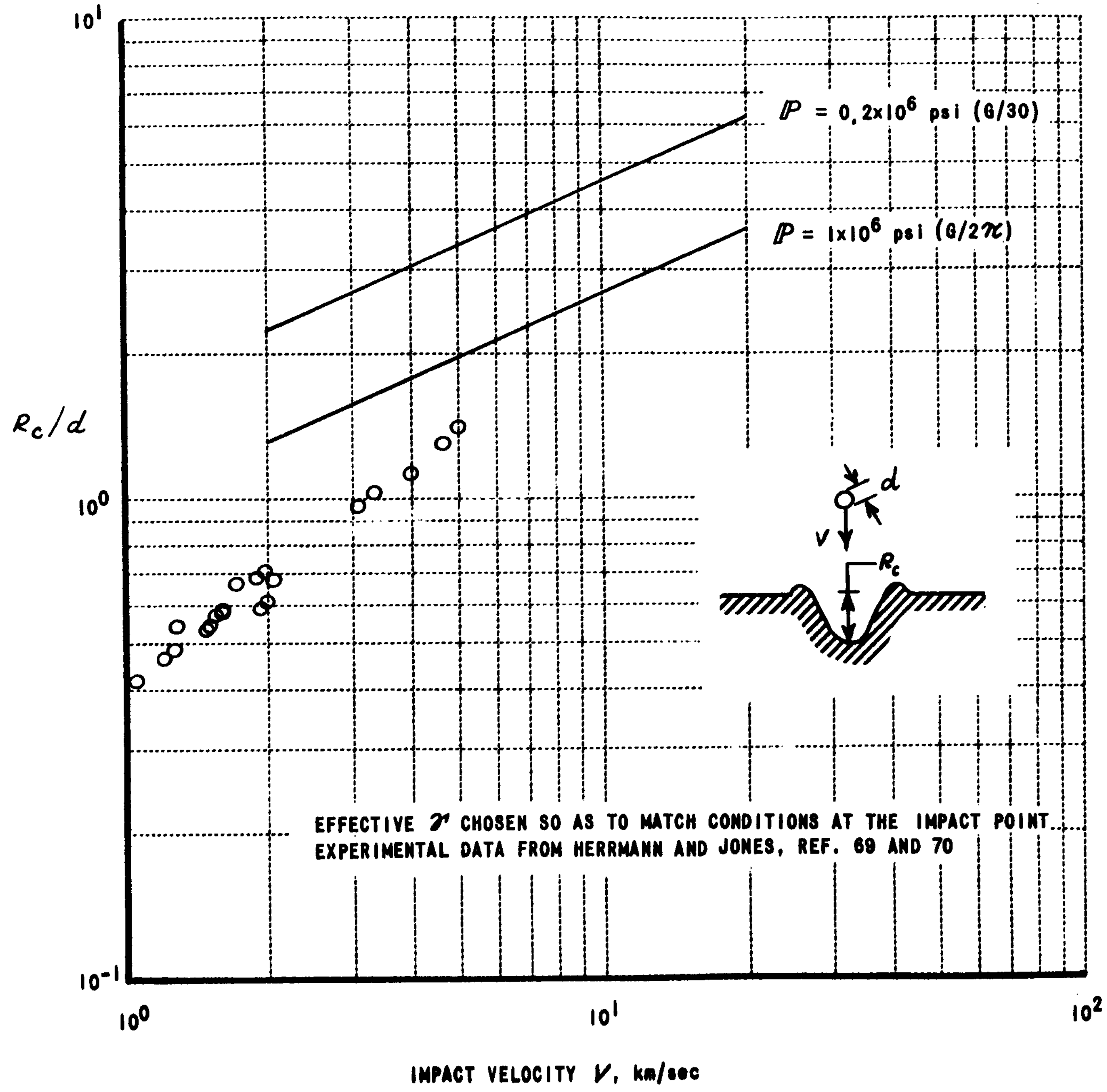

EFFECTIVE γ' CHOSEN SO AS TO MATCH CONDITIONS AT THE IMPACT POINT
EXPERIMENTAL DATA FROM HERRMANN AND JONES, REF. 69 AND 70

Figure 13 CONSTANT-ENERGY, EFFECTIVE-γ' SOLUTION FOR CRATERS FORMED BY ALUMINUM STRIKING COPPER

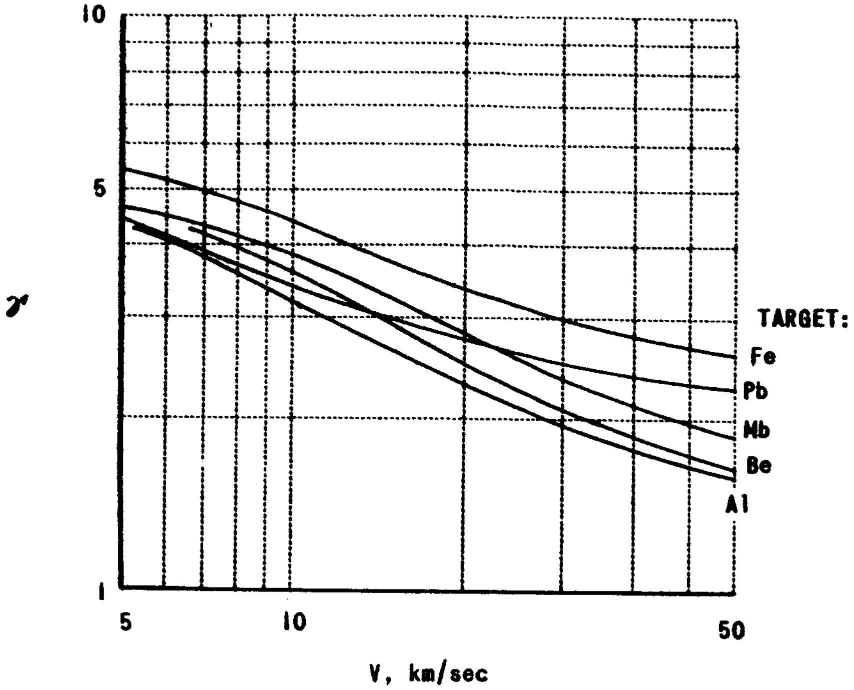

Figure 14a THE FUNCTION γ'(V) FOR FUSED QUARTZ STRIKING VARIOUS TARGETS

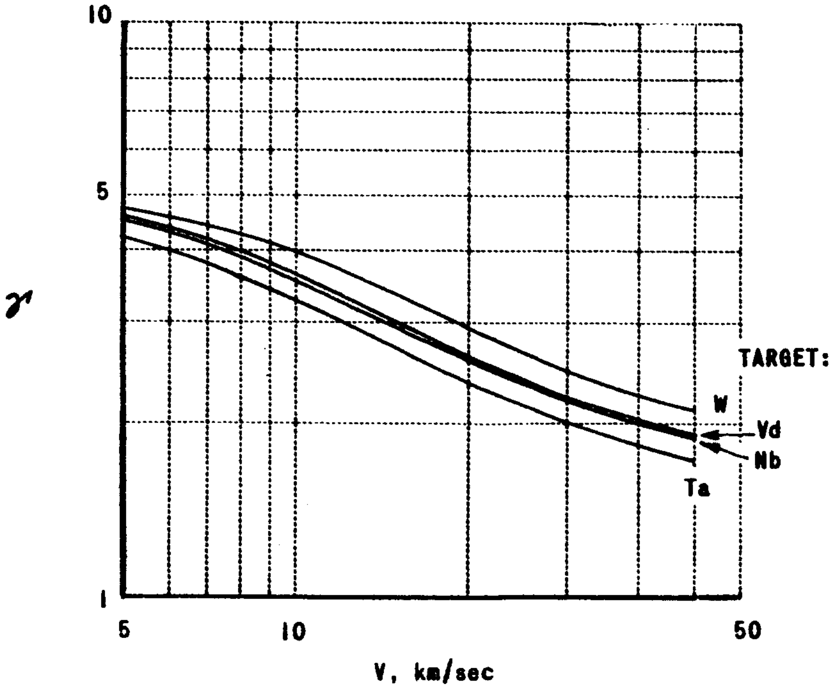

Figure 14b THE FUNCTION γ'(V) FOR FUSED QUARTZ STRIKING VARIOUS TARGETS

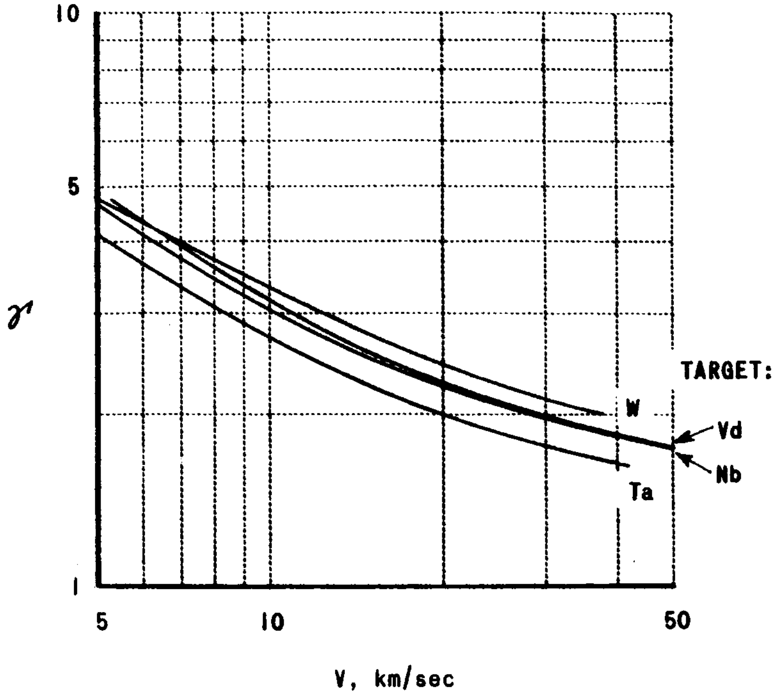

Figure 14c THE FUNCTION $\gamma'(V)$ FOR IRON STRIKING VARIOUS TARGETS

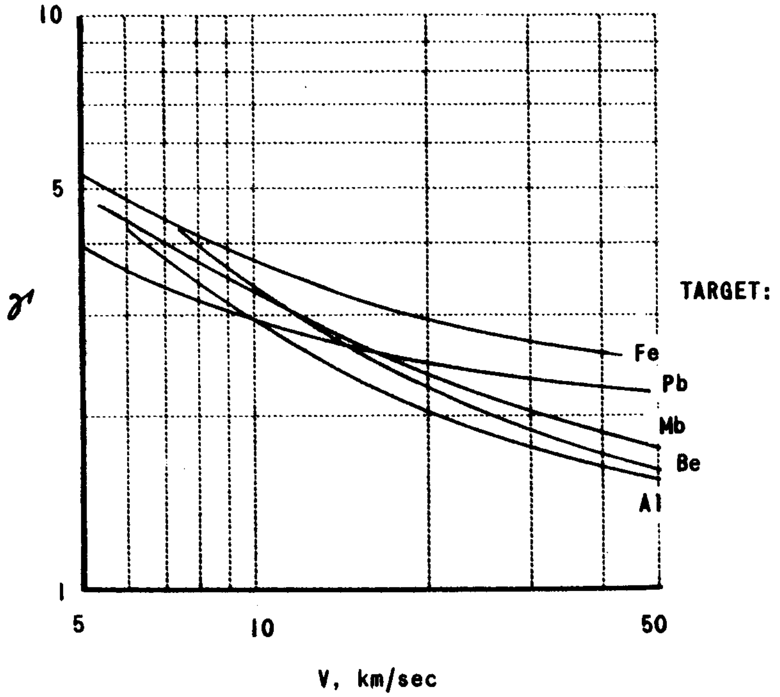

Figure 14d THE FUNCTION $\gamma'(V)$ FOR IRON STRIKING VARIOUS TARGETS

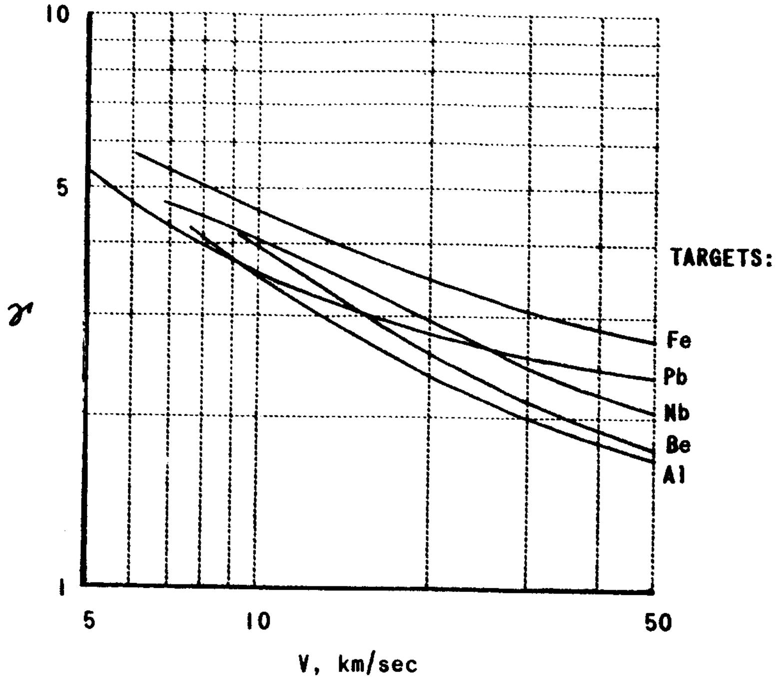

Figure 14e THE FUNCTION γ'(V) FOR ALUMINUM STRIKING VARIOUS TARGETS

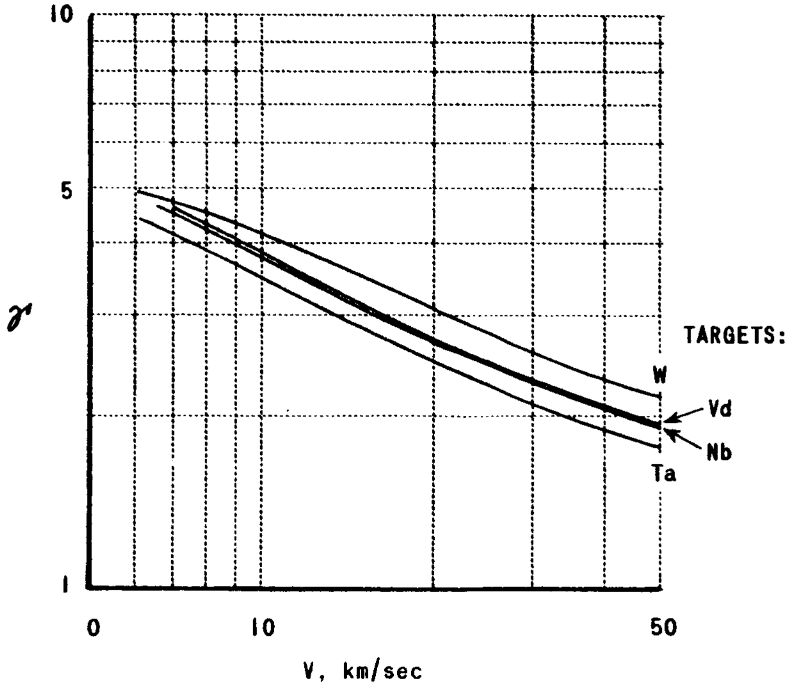

Figure 14f THE FUNCTION γ'(V) FOR ALUMINUM STRIKING VARIOUS TARGETS

$\gamma = 3$ $\quad \tau$ FOUND FROM $\dfrac{\partial^2 f}{\partial \theta^2}(\eta, 0) = -10(1-\eta) f(\eta, 0)$

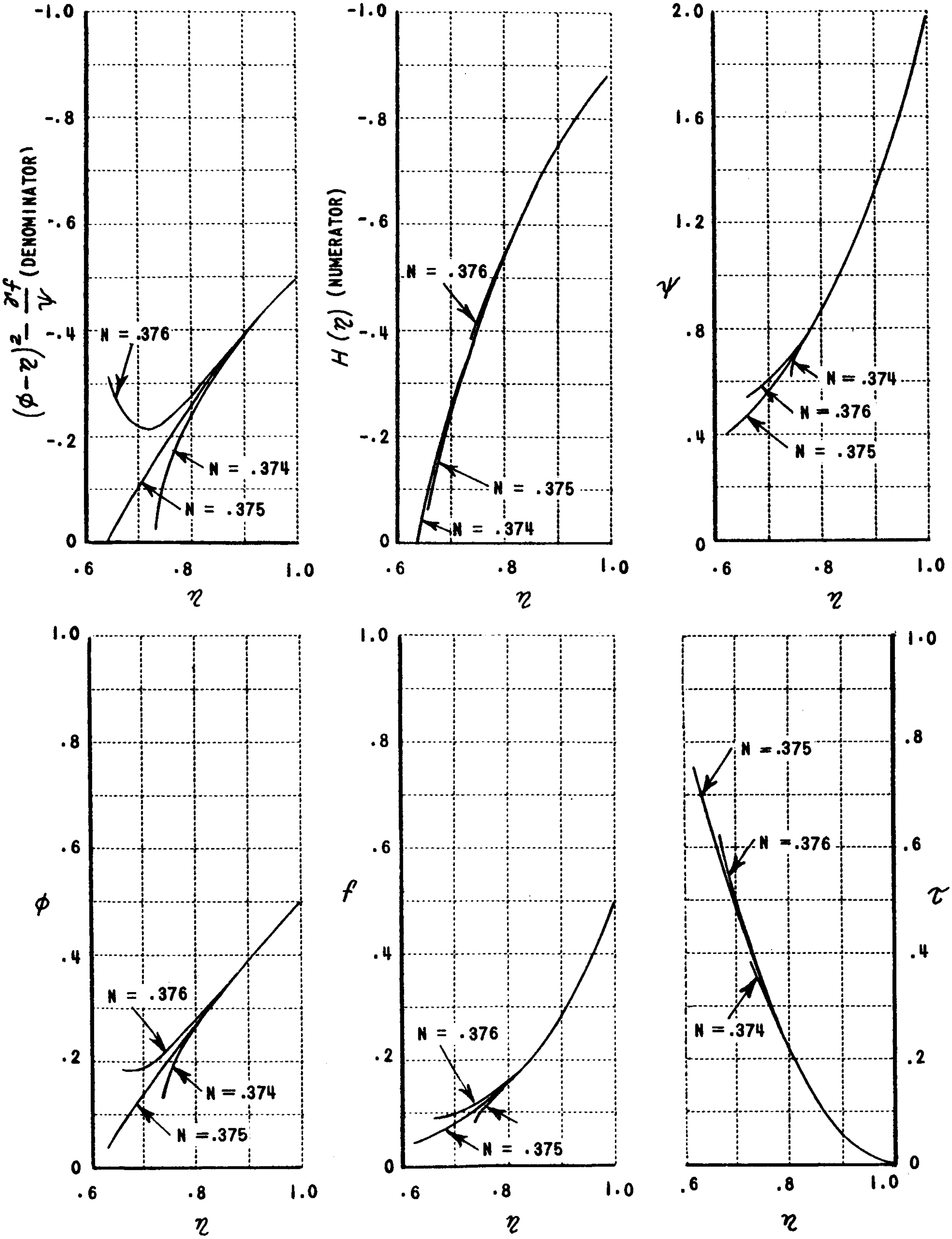

Figure 15a CENTERLINE DISTRIBUTIONS OF DENSITY, PRESSURE, AND VELOCITY

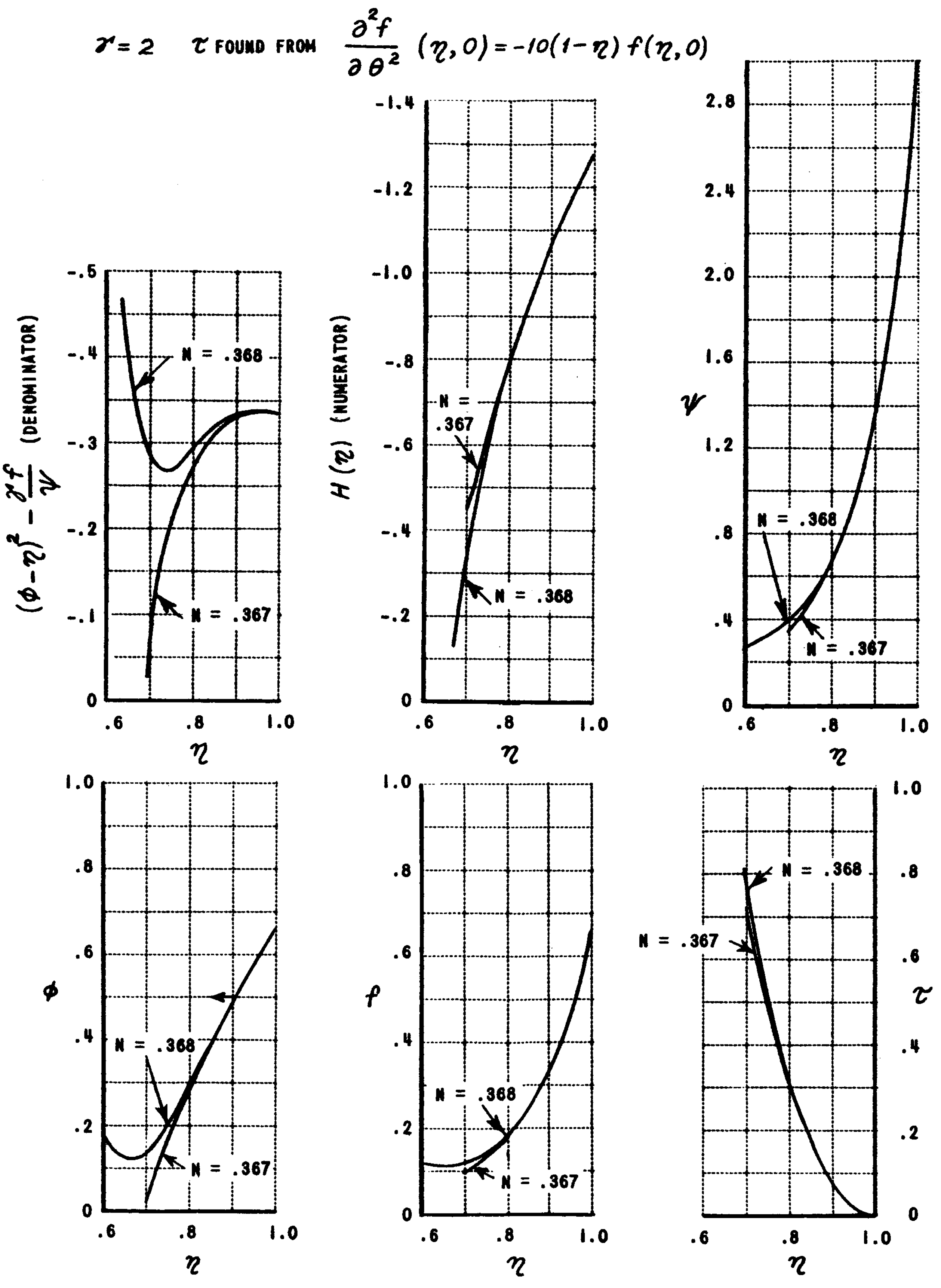

Figure 15b CENTERLINE DISTRIBUTIONS OF DENSITY, PRESSURE, AND VELOCITY

$$\gamma = 2.5 \quad \tau \text{ FOUND FROM } \frac{\partial^2 f}{\partial \theta^2}(\eta, 0) = -10(1-\eta) f(\eta, 0)$$

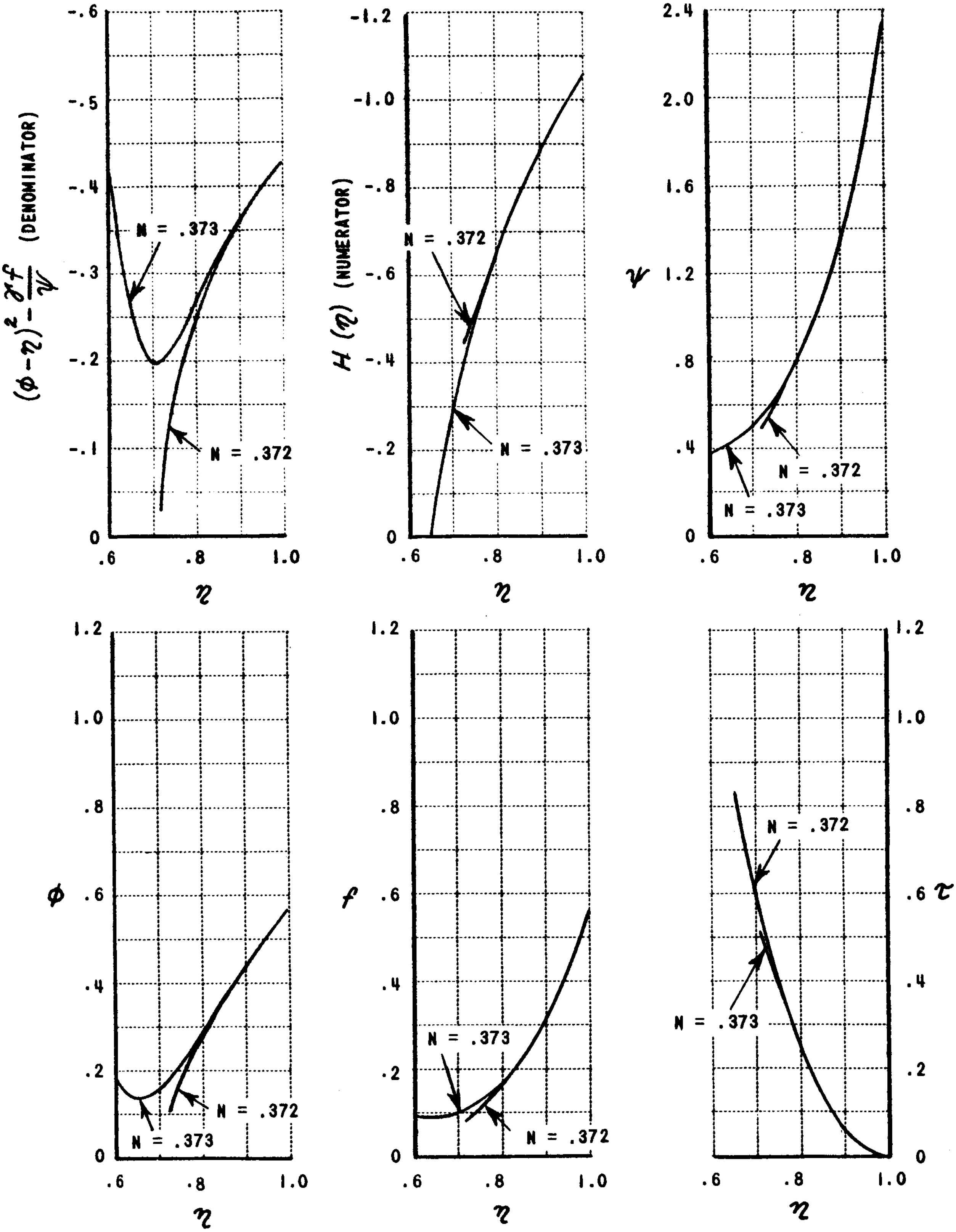

Figure 15c CENTERLINE DISTRIBUTIONS OF DENSITY, PRESSURE, AND VELOCITY

$\gamma = 4 \quad \tau$ FOUND FROM $\frac{\partial^2 f}{\partial \theta^2}(\eta, 0) = -10(1-\eta) f(\eta, 0)$

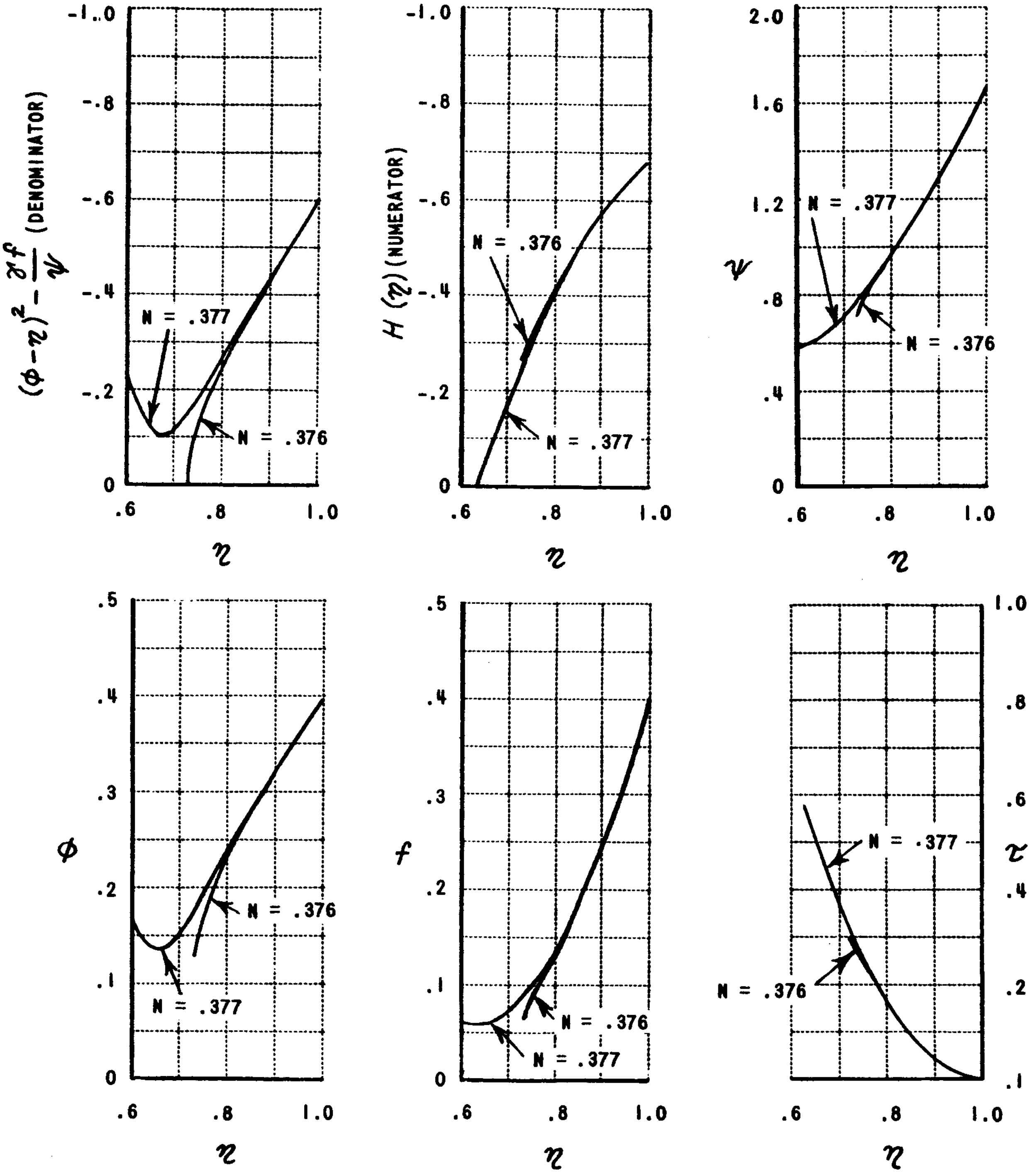

Figure 15d CENTERLINE DISTRIBUTIONS OF DENSITY, PRESSURE, AND VELOCITY

$\gamma = 6 \quad \tau$ FOUND FROM $\dfrac{\partial^2 f}{\partial \theta^2}(\eta, 0) = -10(1-\eta) f(\eta, 0)$

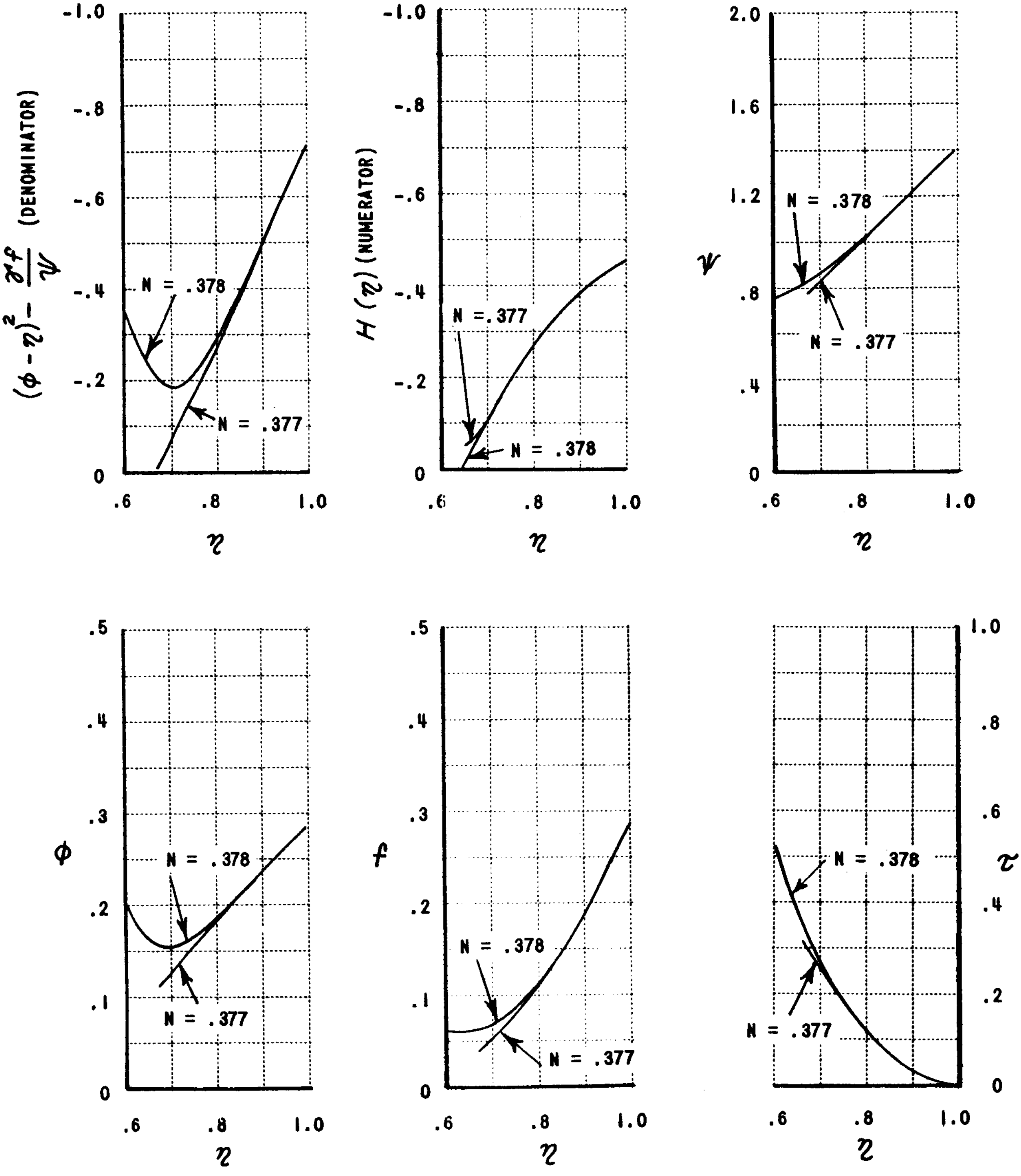

Figure 15e CENTERLINE DISTRIBUTIONS OF DENSITY, PRESSURE, AND VELOCITY

$\gamma = 4$ τ FOUND FROM $\frac{\partial^2 f}{\partial \theta^2}(\eta,0) = -1(1-\eta)f(\eta,0)$

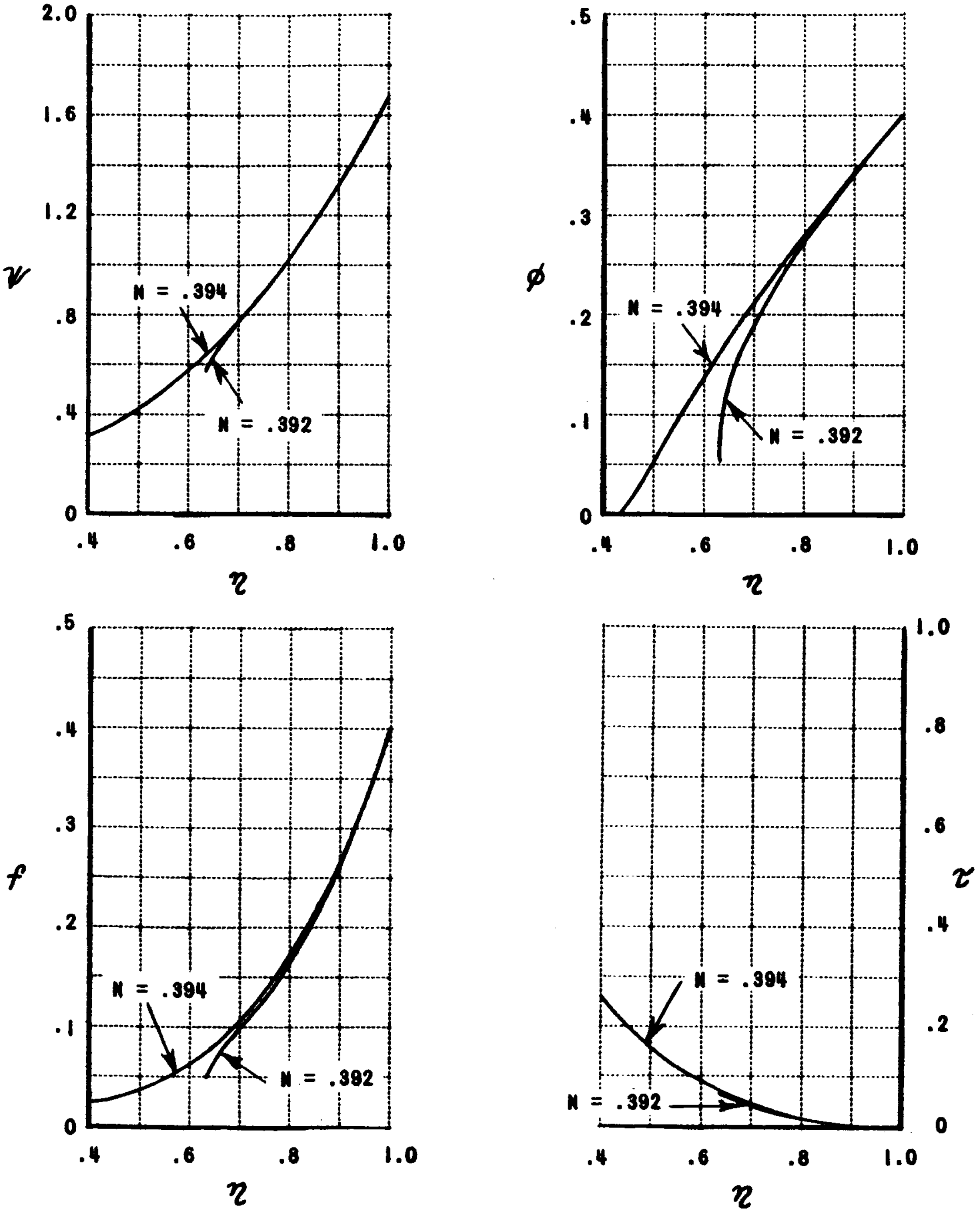

Figure 16 CENTERLINE DISTRIBUTIONS OF DENSITY, PRESSURE, AND VELOCITY

$\gamma = 3$ SOLUTION FOR N = 0.375 BASED ON THE APPROXIMATION

$$\frac{\partial^2 f}{\partial \theta^2}(\eta, o) = -10(1-\eta) f(\eta, o)$$

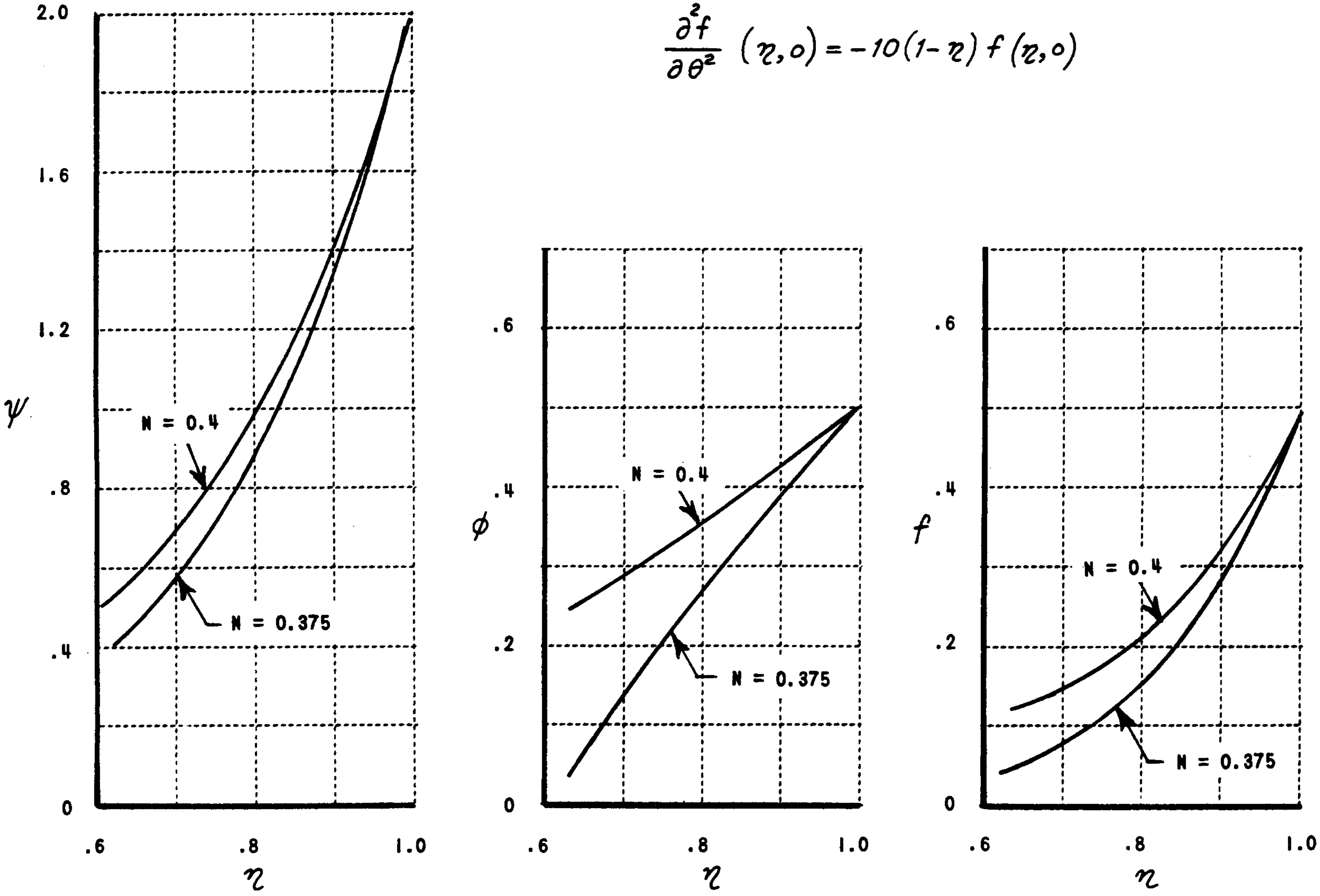

Figure 17 CONSTANT-ENERGY, SPHERICALLY-SYMMETRIC SOLUTION (N = 0.4) COMPARED WITH "CENTERLINE" SOLUTION (N = 0.375)

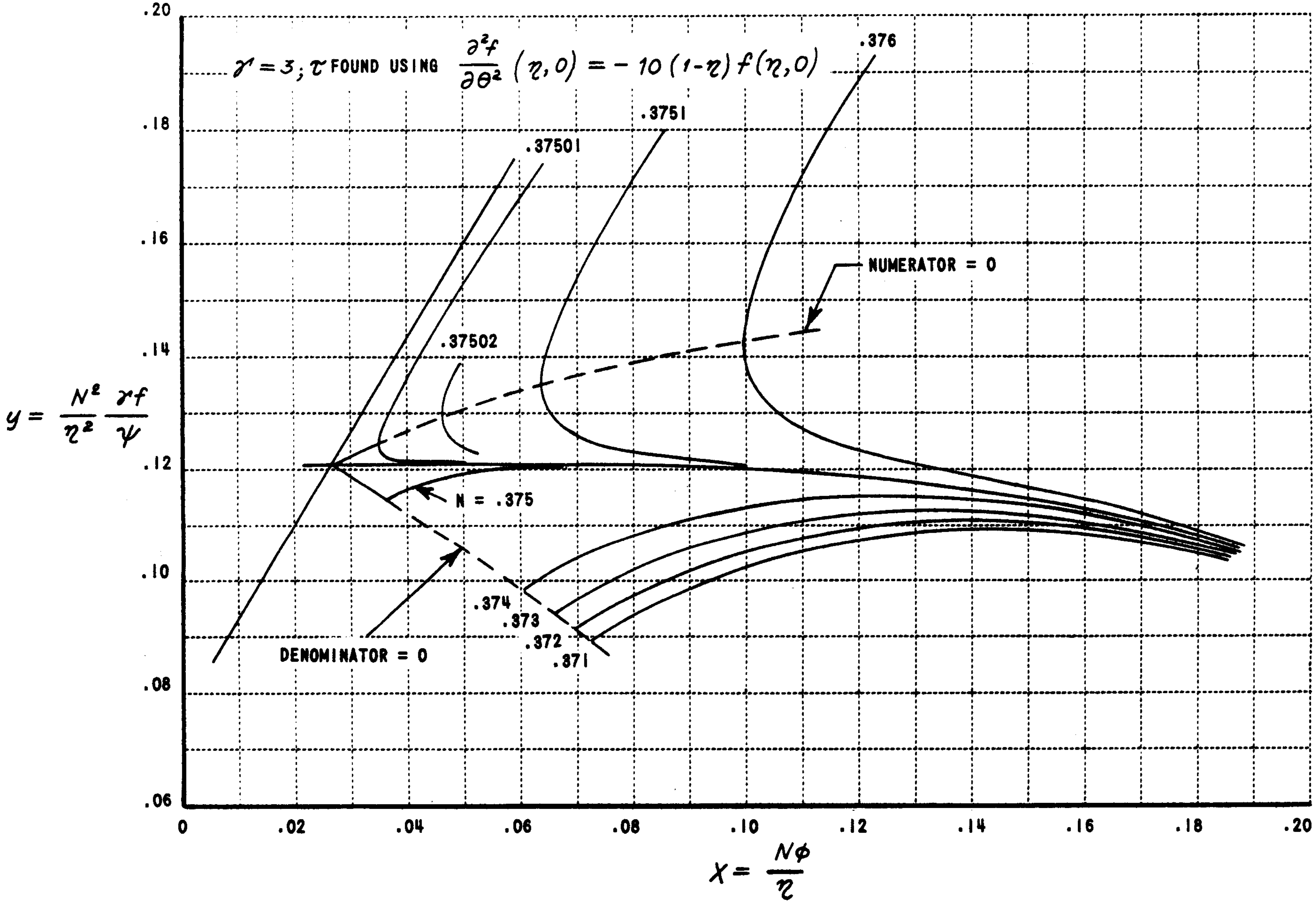

Figure 18 SONIC-LINE CROSSING IN THE x, y PLANE

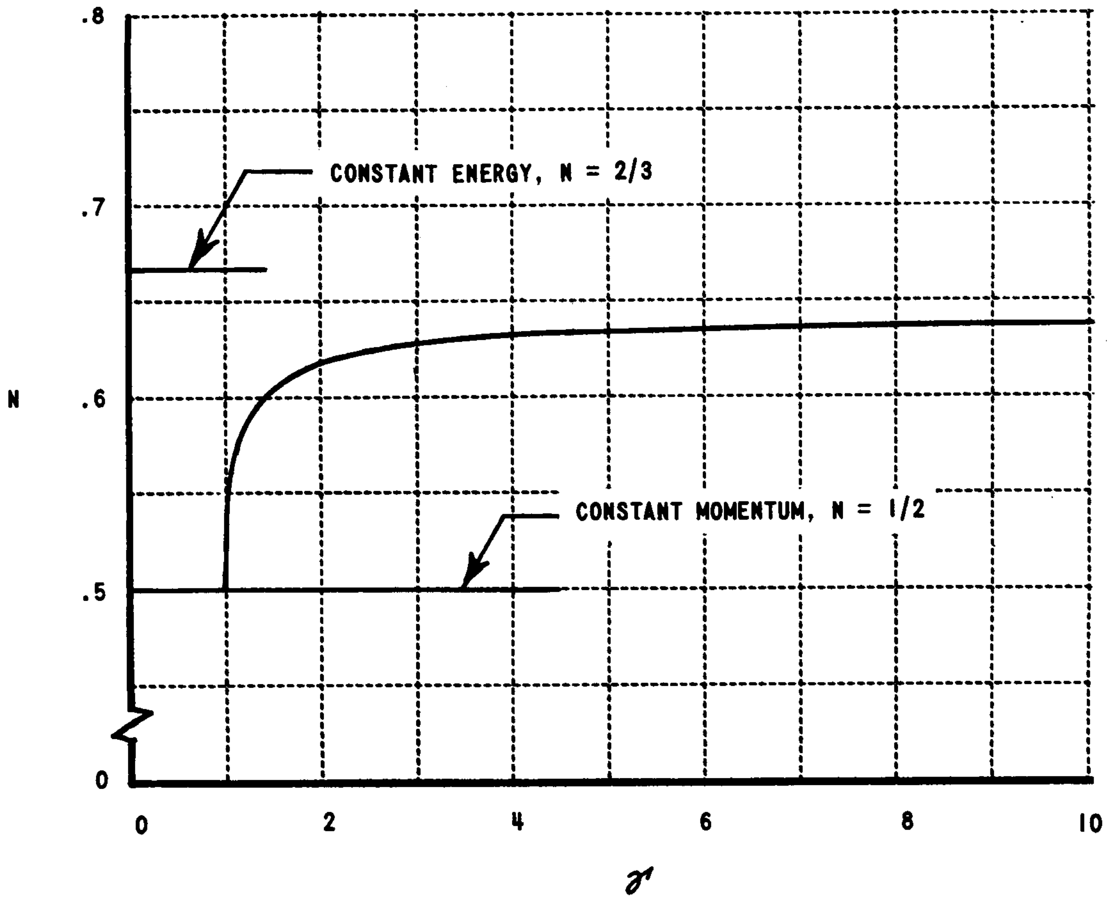

Figure 19 DEPENDENCE OF N ON γ FOR ONE-DIMENSIONAL BLAST WAVES

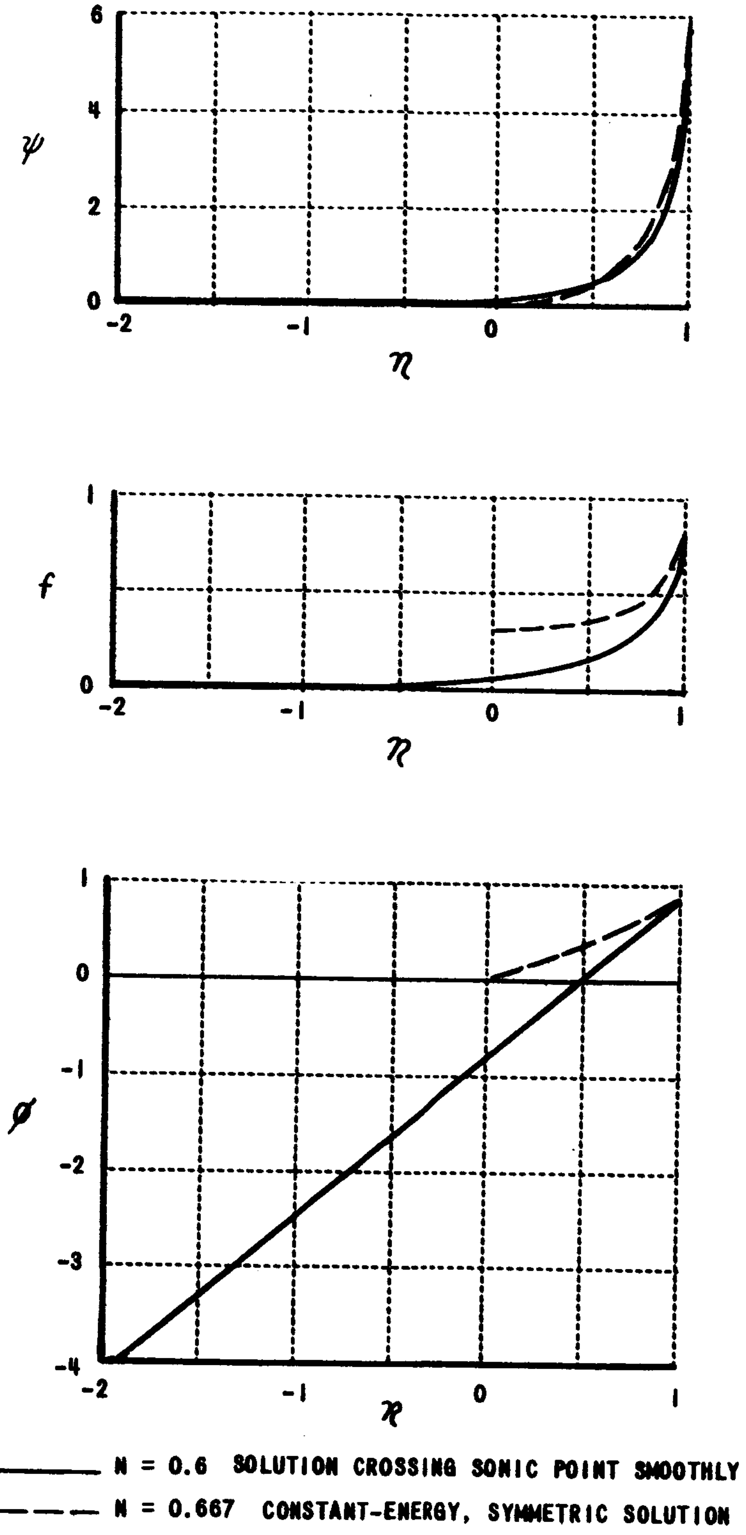

Figure 20 ONE-DIMENSIONAL BLAST-WAVE SOLUTIONS, $\gamma = 1.4$

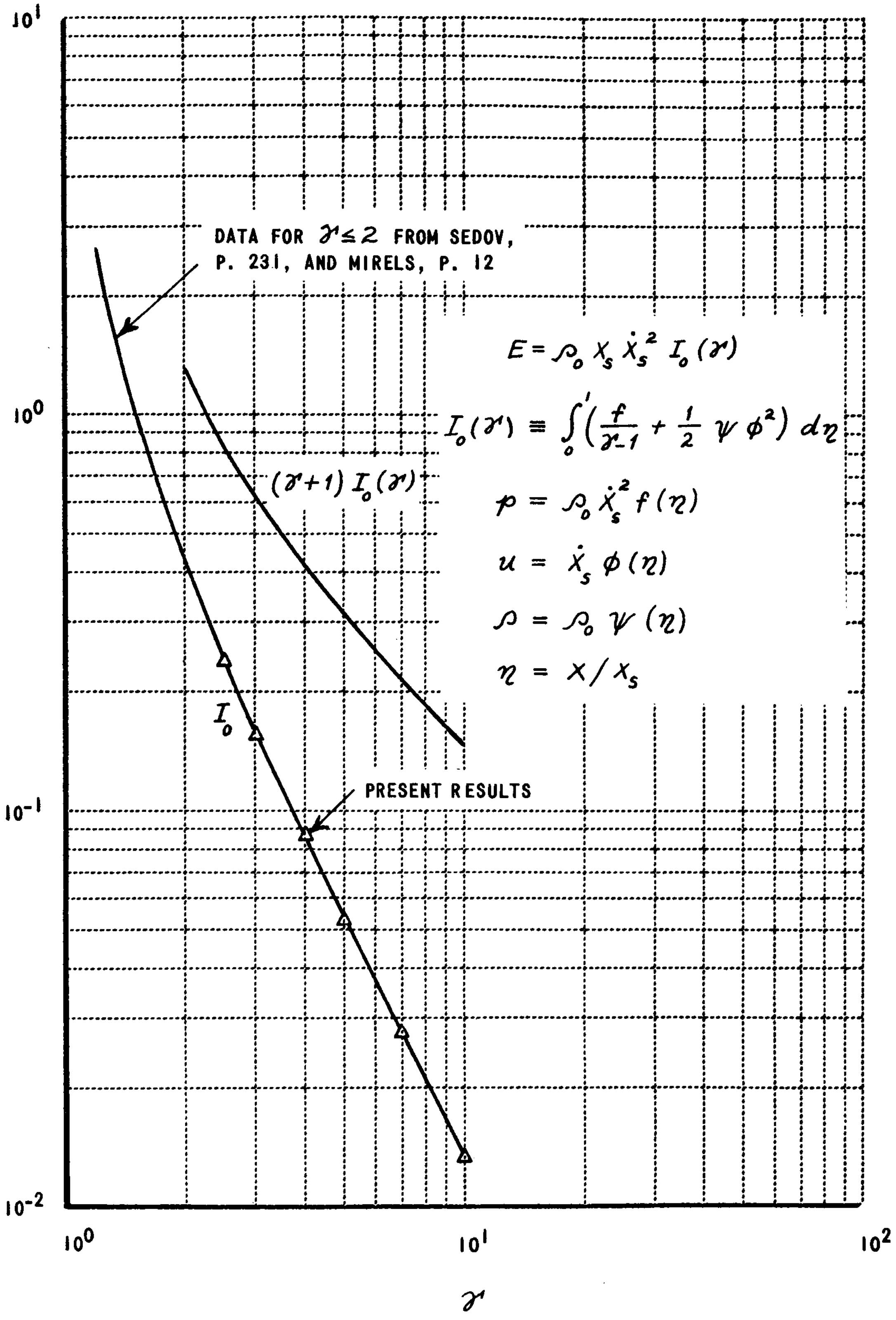

Figure 21 ONE-DIMENSIONAL, SYMMETRIC CONSTANT-ENERGY BLAST WAVES

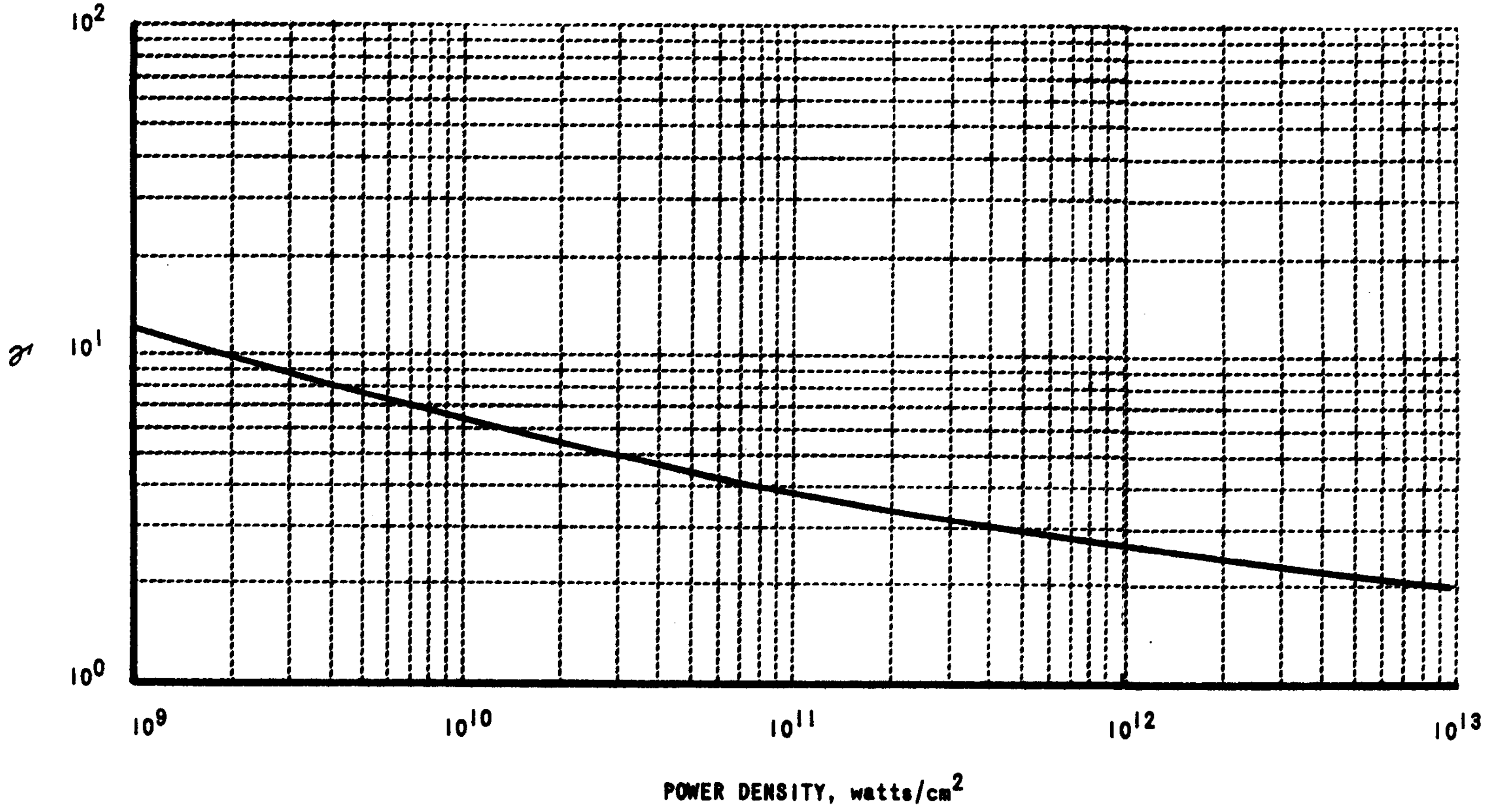

Figure 22 POWER-DENSITY RATING FOR SHOCK WAVES IN IRON

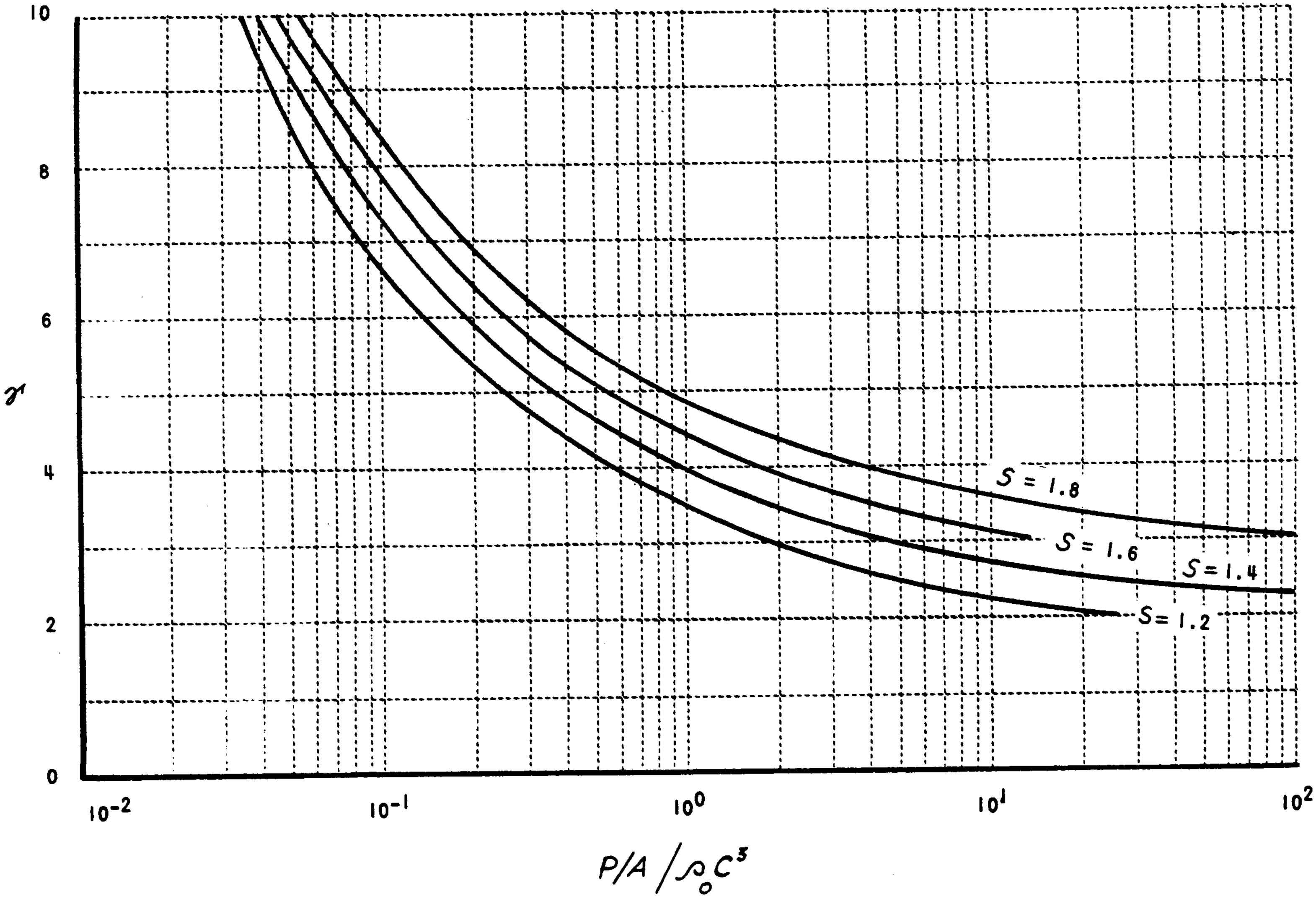

Figure 23 POWER-DENSITY RATING FOR MATERIALS WHOSE HUGONIOT IS DESCRIBED BY $u_s = C + Su_1$

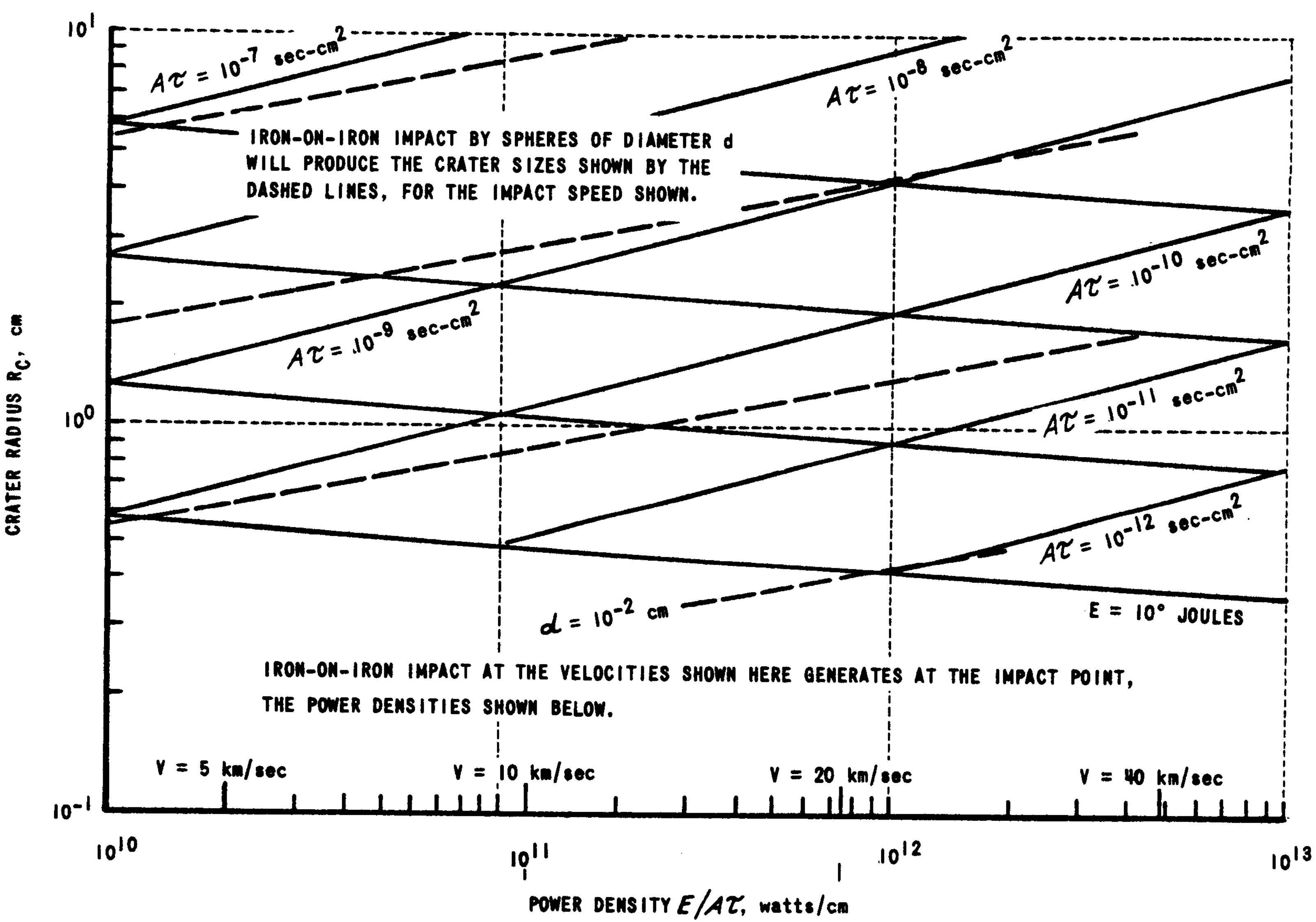

Figure 24 BLAST-WAVE PREDICTION OF CRATERS FORMED IN IRON BY DEPOSITION OF ENERGY E OVER AREA A IN TIME τ

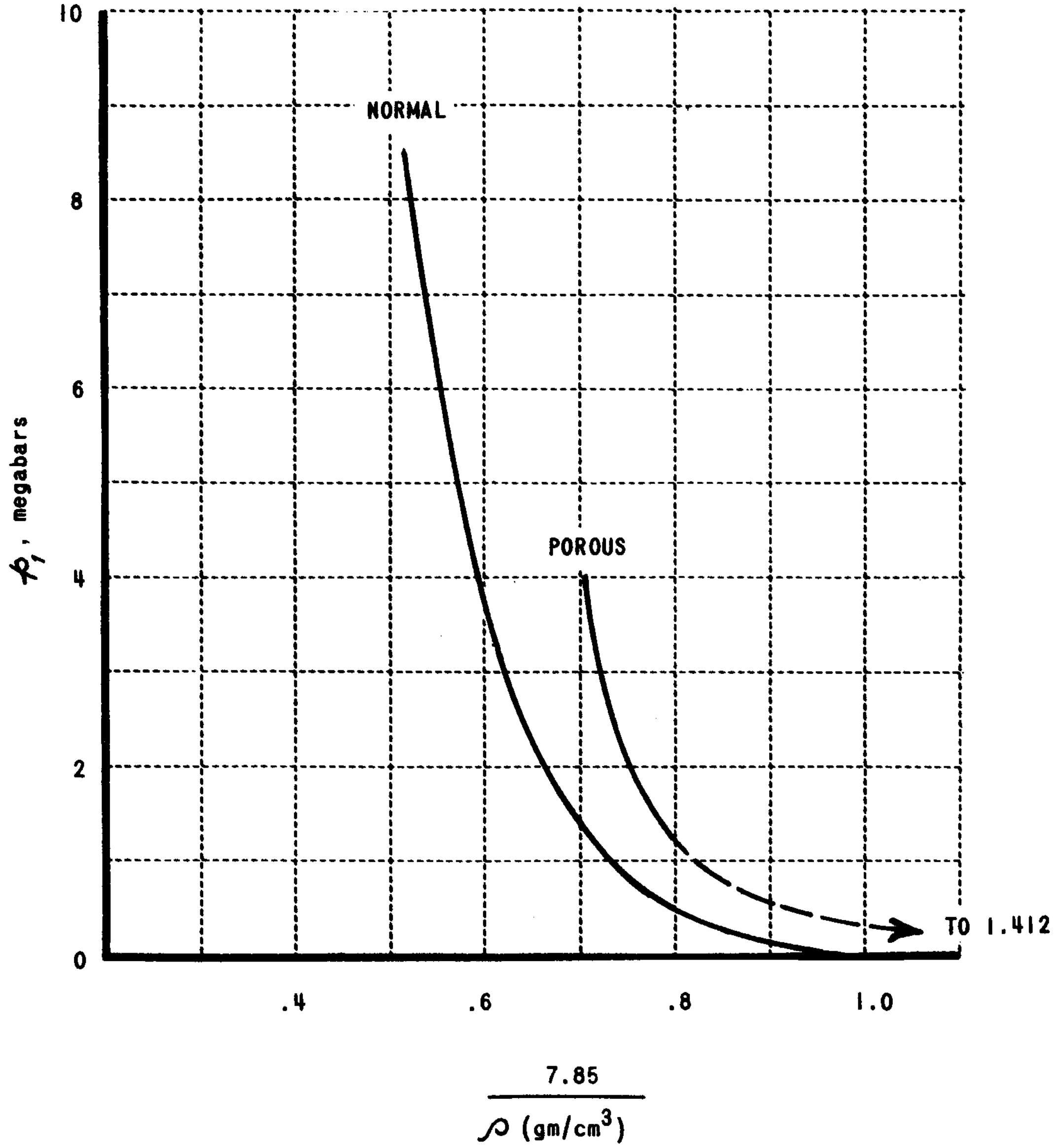

Figure 25 HUGONIOTS FOR NORMAL AND POROUS IRON

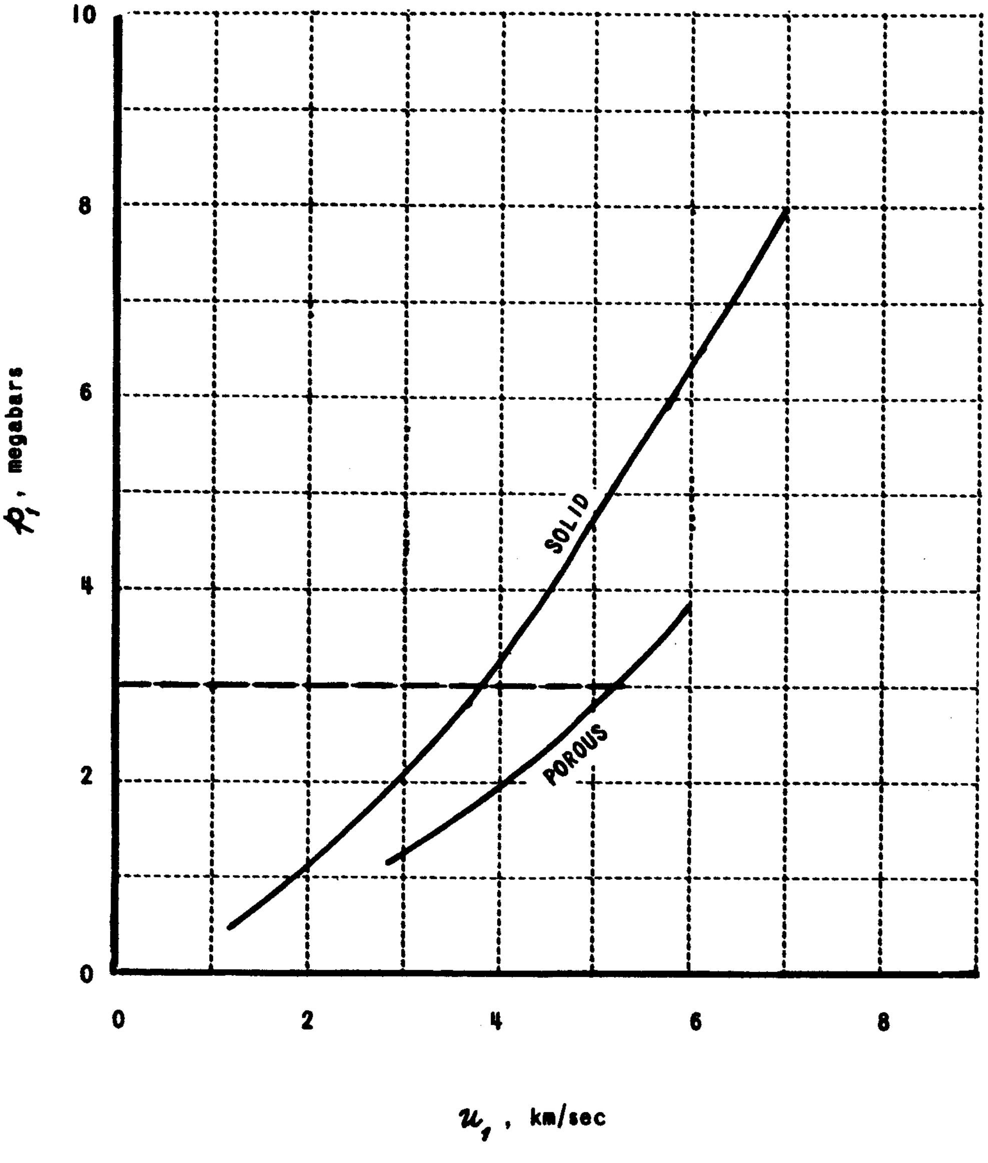

Figure 26 PRESSURE vs PARTICLE VELOCITY FOR NORMAL AND POROUS IRON

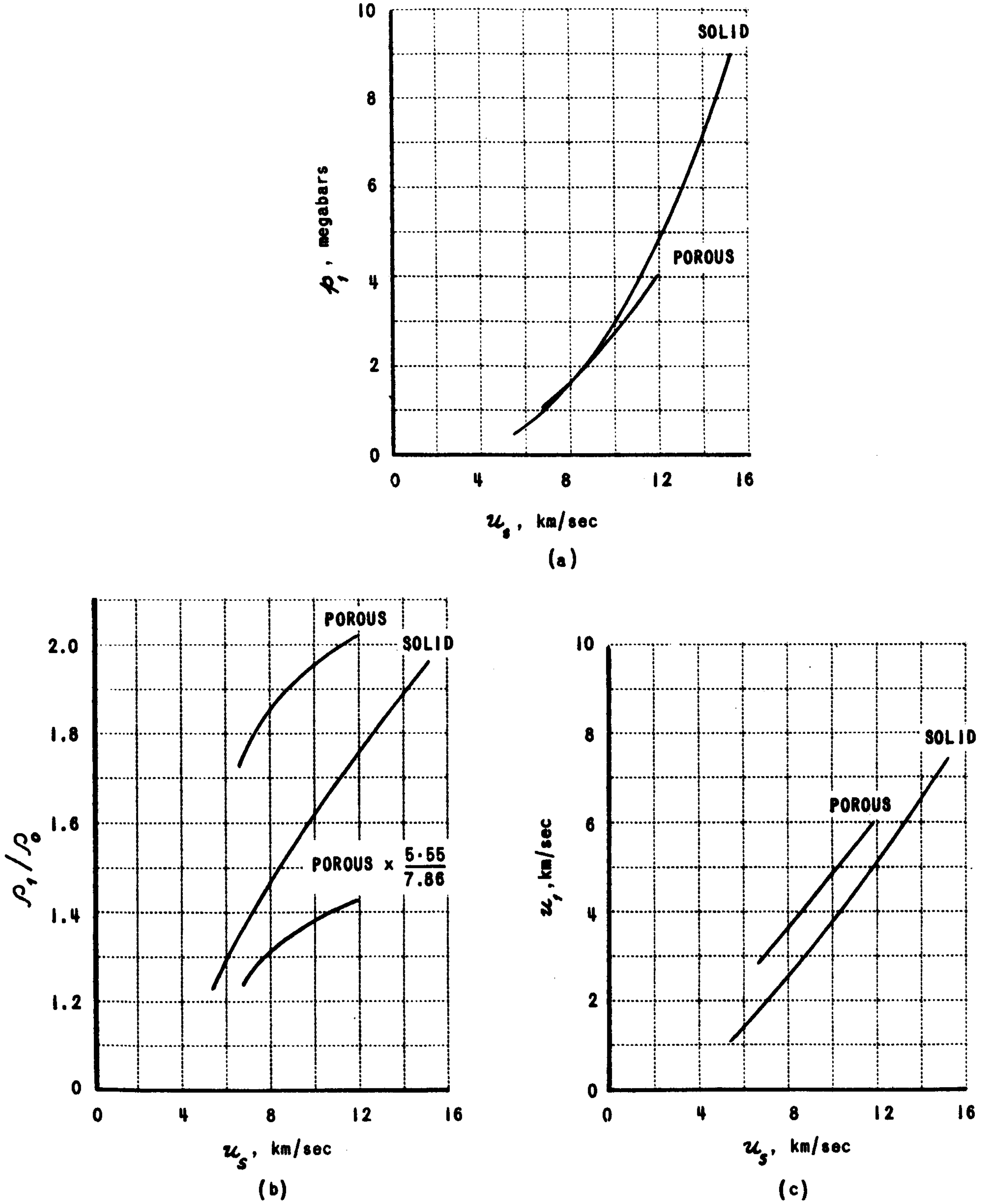

Figure 27 HUGONIOTS FOR "SOLID" AND "POROUS" IRON, AFTER ALTSHULER ET AL.

"SOLID" - ρ_0 = 7.86 gm/cm^3 "POROUS" - ρ_0 = 5.55 gm/cm^3

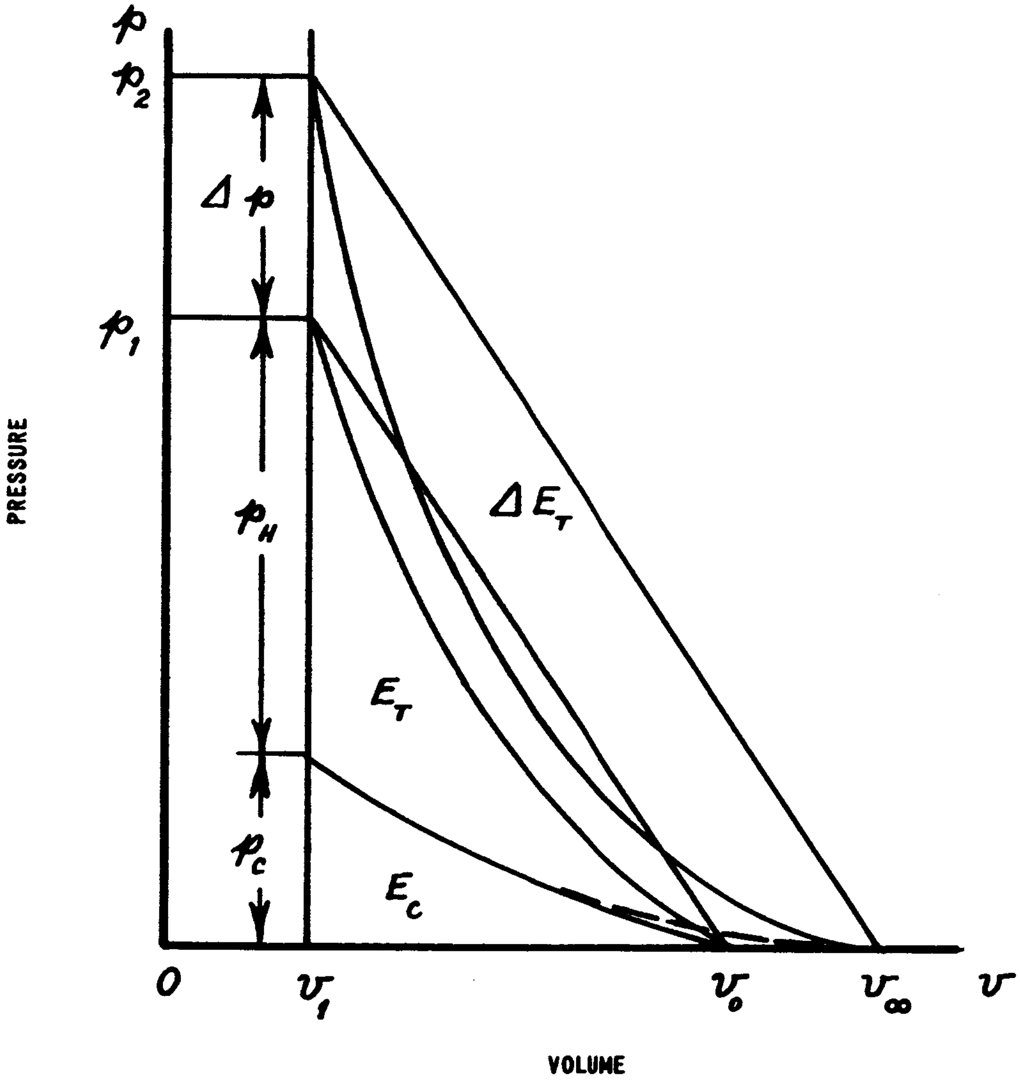

Figure 28 SCHEMATIC SHOCK COMPRESSION DIAGRAM OF POROUS AND NON-POROUS MATERIAL

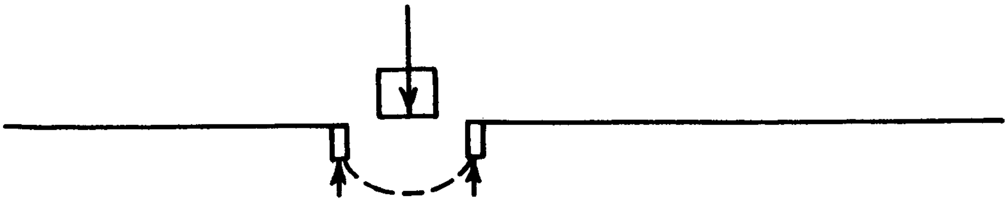

(a) EARLY TIME

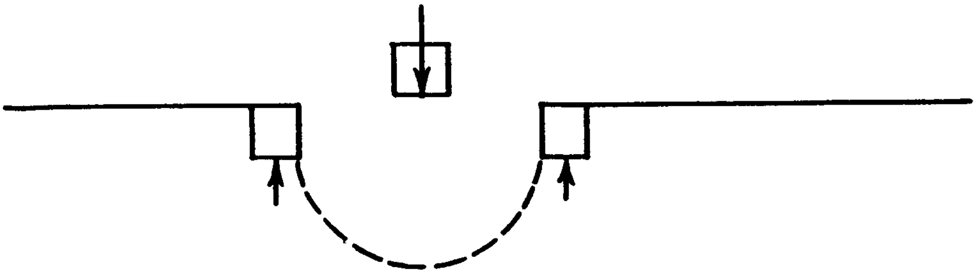

(b) LATER TIME

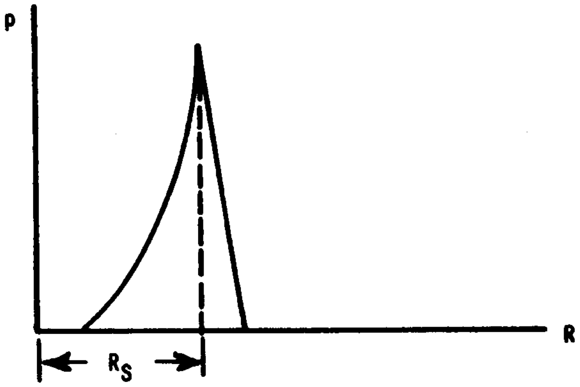

(c) p vs DISTANCE FROM THE IMPACT POINT (AT LATE TIME)

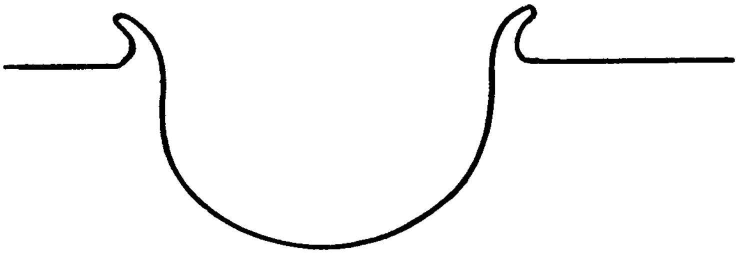

(d) SCHEMATIC CRATER PROFILE

Figure 29 EJECTION OF MATERIAL FROM A CRATER

Table I
HUGONIOT DATA
$$u_s = C + Su_1$$

MATERIAL	ρ_0 gm/cm^3	C, km/sec	S	$\rho_0 C^2$ MEGABARS	$G/2\pi$ MEGABARS	SOURCE
SILVER	10.49	3.22	1.64	1.094		REF. 7. 11, 65
GOLD	19.24	3.06	1.61	1.800		
CADMIUM	8.64	2.41	1.72	.501		
COBALT	8.82	4.65	1.51	1.909		
CHROMIUM	7.10	5.18	1.54	1.902		
COPPER	8.90	3.97	1.48	1.404	0.069	
MOLYBDENUM	10.20	5.17	1.20	2.73		
NICKEL	8.86	4.67	1.41	1.930		
LEAD	11.34	2.07	1.52	.484	0.0069	
TIN	7.28	2.67	1.43	.518		
THORIUM	11.68	2.08	1.38	.505		
TITANIUM	4.51	4.79	1.07	1.033		
THALLIUM	11.84	1.82	1.57	.393		
VANADIUM	6.1	5.11	1.21	1.592		
TUNGSTEN	19.17	4.00	1.27	3.07	0.21	
ZINC	7.14	3.04	1.58	.661		
BISMUTH	9.80	2.0	1.36	.392		
IRON	7.87	4.0	1.59	1.259	0.14	
ANTIMONY	6.62	2.0	1.67	.265		
BERYLLIUM	1.82	7.98	1.09	1.157	0.21	
MAGNESIUM	1.74	4.49	1.27	.351		
INDIUM	7.31	2.37	1.61	.411	0.0062	
NIOBIUM	8.57	4.45	1.21	1.695	0.062	
PALLADIUM	12.0	3.79	1.92	1.726		
PLATINUM	21.45	3.67	1.40	2.89		
RHODIUM	12.44	4.68	1.64	2.72		
TANTALUM	16.6	3.37	1.15	1.890		
ZIRCONIUM	6.5	3.77	0.93	.924		
ALUMINUM	2.7	5.85	1.11	.924	0.041	
LUCITE	1.18	2.59	1.51	.0792	0.0021	REF. 66
FUSED QUARTZ	2.20	1.30	1.56	.0372	0.048	REF. 43

Table 2
N(γ) FOR ONE-DIMENSIONAL BLAST WAVES

γ	$\frac{\gamma+1}{\gamma-1}$	N	SOURCE
1	∞	.5	REF. 28
1.1	21	.56888	"
1.4	6	.6	"
5/3	4	.61073	"
2.8	2.1111	.626704	"
∞	1	.6416	"
1.001	2001	.5106	PRESENT REPORT
1.1	21	.5683	"
1.2	11	.5843	"
1.3	7.6667	.5935	"
1.4	6	.6000	"
1.8	3.5	.6143	"
2.0	3	.6182	"
2.5	2.3333	.6244	"
3.0	2	.6279	"
4.0	1.6667	.6321	"
5.0	1.5	.6341	"
7.0	1.3333	.6365	"
10.0	1.2222	.6385	"
100.0	1.0202	.6412	"
1000.0	1.0020	.6416	"

Table 3
STAGES OF ENERGY TRANSFORMATION DURING IMPACT

STAGE	ENERGY TRANSFORMATION	DURATION OR TERMINATION
1. ELASTIC DEFORMATION	K.E. TO STORED MECHANICAL ENERGY	ENDS WHEN INTERFACE PRESSURE EXCEEDS DYNAMIC YIELD STRENGTH
2. PLASTIC DEFORMATION	K.E. TO ABSORBED MECHANICAL ENERGY	ENDS WHEN INTERNAL ENERGY EXCEEDS LATENT HEAT OF SOLIDIFICATION
3. SOLID STATE PHASE CHANGE	K.E. TO ABSORBED LATTICE ENERGY	OCCURS IN SOME CRYSTALLINE SOLIDS AT ELEVATED TEMP. & PRESSURE
4. HIGH PRESSURE COMPACTION	ABSORBED MECHANICAL ENERGY TO THERMAL ENERGY	CONTINUES UNTIL THERMAL ENERGY EXCEEDS REMAINING KINETIC ENERGY
5. SOLID/LIQUID AND LIQUID/GASEOUS PHASE CHANGES	ABSORBED MECHANICAL ENERGY TO THERMAL ENERGY	OCCURS WHEN LOCAL TEMPERATURE EXCEEDS HIGH PRESSURE MELTING OR BOILING POINT
6. GASEOUS EXPANSION (EXPLOSION)	ABSORBED THERMAL ENERGY TO MECHANICAL ENERGY	OCCURS WHEN LOCAL RATE OF ENERGY ABSORPTION EXCEEDS RATE OF ENERGY RELEASE BY MECHANICAL OR THERMAL RADIATION
7. BLAST WAVE	ABSORBED THERMAL ENERGY TO ABSORBED AND STORED MECHANICAL ENERGY PLUS MECHANICAL ENERGY RADIATED AWAY FROM TARGET	EFFECTIVELY ENDS WHEN RATE OF ENERGY RELEASE FALLS BELOW THE STRONG SHOCK WAVE VELOCITY
8. GASEOUS/LIQUID AND LIQUID/SOLID PHASE CHANGE	ABSORBED THERMAL ENERGY TO MECHANICAL ENERGY	OCCURS AS THE OUTER TEMPERATURES OF THE ENLARGED DAMAGE AREA FALL BELOW THE BOILING AND FREEZING POINTS
9. PLASTIC DEFORMATION	DYNAMIC MECHANICAL ENERGY TO ABSORBED MECHANICAL ENERGY	OCCURS WHEN BLAST WAVE PRESSURE EXCEEDS DYNAMIC YIELD STRENGTH. ENDS WHEN STRAIN RATE BECOMES LESS THAN WEAK SHOCK WAVE VELOCITY
10. SHOCK WAVES AND STRESS WAVES	RADIATION OF MECHANICAL ENERGY	CONTINUES UNTIL ALL DYNAMIC MECHANICAL ENERGY IS ABSORBED
11. FRAGMENTATION	STORED MECHANICAL ENERGY TO ABSORBED MECHANICAL ENERGY	OCCURS AFTER RAPIDLY DEVELOPED HIGH COMPRESSIVE STRESSES

Table 4

PHYSICAL PROPERTIES OF SELECTED SOLIDS (AT ROOM TEMPERATURE)

MATERIAL	DENSITY ρ gm / cm^3	MELTING OR SOFTENING POINT °C	YOUNG'S MODULUS Y 10^6psi	BULK DILATATIONAL WAVE VELOCITY C_l km / sec	DYNAMIC SHEAR MODULUS G 10^6psi	SHEAR WAVE VELOCITY C_S km / sec	INTRINSIC SHEAR STRENGTH $\frac{G}{30}$ TO $\frac{G}{2\pi}$ 10^6psi
<u>PLASTICS</u>							
POLYETHYLENE	0.90	100°(S.P.)	0.11	2.0	0.055	0.5	0.002-.009
POLYSTYRENE	1.06	85°(S.P.)	0.76	2.4	0.19	1.1	0.006-.03
LUCITE*	1.18	85°(S.P.)	0.58	2.7	0.21	1.1	0.007-.03
<u>SOFT METALS</u>							
INDIUM	7.28	156°	1.57	2.4	0.54	0.7	0.02 -.09
LEAD	11.3	327°	2.3	2.0	0.78	0.7	0.03 -.1
SOLDER(60Sn-40Pb)	8.52	188°	4.5	3.1	1.58	1.1	0.05 -.3
<u>METALS</u>							
ALUMINUM	2.71	660°	10.5	6.4	3.6	3.0	0.1 - .6
DURAL (17ST)	2.67	540°	10.4	6.3	3.9	3.1	0.1 - .6
COPPER	8.9	1083°	18	5.0	6.7	2.3	0.2 -1
STAINLESS STEEL (34T)	7.9		28.4	5.8	11.0	3.1	0.4 -2
IRON	7.7	1535°	29.9	5.9	11.9	3.2	0.4 -2
TUNGSTEN	19.3	3410°	52.5	5.4	19.4	2.6	0.6 -3
BERYLLIUM	1.84	1278°	44.6	12.9	21.3	8.9	0.7 -3
<u>GLASS</u>							
PYREX	2.23	820°(S.P.)	9.0	5.6	3.6	3.3	0.1 - .6
FUSED SILICA (SiO_2)	2.20	1670°(S.P.)	10.5	5.9	4.5	3.7	0.2 - .7
<u>CERAMICS</u>							
HEMATITE (Fe_2O_3)	5.20	1565°	34	6.8	15	4.6	0.5 -2
MAGNETITE (Fe_3O_4)	5.18	1538°	33	7.3	13	4.2	0.4 -2
CORUNDUM (Al_2O_3)	3.98	2020°	59	11.0	23.5	6.4	0.8 -4
SILICON CARBIDE	3.1	2600°	58	12.0	24	7.3	0.8 -4
POROUS SOLIDS							
IRON (P = 99.3%)	0.05	1535°	-	-	< 0.01	-	<0.001
IRON (P = 93.5%)	0.5	1535°	< 0.3	< 2	< 0.1	< 1	<0.01
IRON OXIDE (P=99.1%)	0.05	~ 1550°	-	-	< 0.01	-	<0.001
(P=90.4%)	0.5	~ 1550°	< 0.3	< 2	< 0.15	< 1	<0.02

* LUCITE IS A TRADE NAME FOR POLYMETHYL-METHACRYLATE

Table 5
VARIATION OF ELASTIC CONSTANTS WITH PRESSURE

MATERIAL	ELASTIC MODULUS M	PRESSURE COEFFICIENT OF ELASTIC MODULUS $\frac{1}{M}\frac{dM}{dp}$	PRESSURE RANGE STUDIED	REFERENCE
α-QUARTZ	C_{14}	-9.0×0^{-6} cm^2/kg	1000 ATMOS.	67
(SiO_2)	C_{44}	4.9×0^{-6} cm^2/kg		
	C_{66}	-6.8×10^{-6} cm^2/kg		
FUSED SILICA	C_{11}	-1.3×10^{-8} $cm^2/dyne$	3.5×10^6 $dynes/cm^2$	68
(SiO_2)	C_{44}	-1.0×10^{-8} $cm^2/dyne$		
ALUMINUM	$K = \frac{1}{3}(C_{11} + 2C_{12})$	0.51×10^5 $\frac{\partial \ln M}{\partial P}$ $\left(\frac{1}{bar}\right)$		46 (p.324)
	C_{44}	0.75×10^5 $\frac{\partial \ln M}{\partial P}$ $\left(\frac{1}{bar}\right)$		
COPPER	$K = \frac{1}{3}(C_{11} + 2C_{12})$	0.41×10^5 $\frac{\partial \ln M}{\partial P}$ $\left(\frac{1}{bar}\right)$		46 (p.324)
	C_{44}	0.31×10^5 $\frac{\partial \ln M}{\partial P}$ $\left(\frac{1}{bar}\right)$		

Table 6
ENERGY DISTRIBUTION IN POROUS AND NON-POROUS BODIES

	IMPACT VELOCITY u_i km/sec	INITIAL INTERFACE PRESSURE MEGABARS	PARTICLE VELOCITY u_1 - km/sec		SHOCK VELOCITY u_s - km/sec		SHOCK DENSITY RATIO ρ_1/ρ_0		INT. ENERGY PER UNIT MASS e - ergs/gm		INT. ENERGY DIFFERENCE COL 9 - COL 10 ergs/gm
			METEOROID	VEHICLE	METEOROID	VEHICLE	METEOROID	VEHICLE	METEOROID	VEHICLE	
CASE I POROUS "METEOROID" AND NON-POROUS VEHICLE SKIN	9	3.1	5.2	3.8	10.6	10.1	1.97	1.63	1.4×10^{11}	0.76×10^{11}	$+0.64 \times 10^{11}$
CASE II NON-POROUS "METEOROID" AND POROUS VEHICLE SKIN	9	3.1	3.8	5.2	10.1	10.6	1.63	1.97	0.76×10^{11}	1.4×10^{11}	-0.64×10^{11}
CASE III NON-POROUS "METEOROID" AND NON-POROUS VEHICLE SKIN	9	4.0	4.5	4.5	11.1	11.1	1.69	1.69	1.0×10^{11}	1.0×10^{11}	----
CASE IV POROUS "METEOROID" AND POROUS VEHICLE SKIN $u_i = 9$	9	2.4	4.5	4.5	9.4	9.4	1.92	1.92	1.0×10^{11}	1.0×10^{11}	----
CASE V POROUS "METEOROID" AND POROUS VEHICLE SKIN $u_i = 12.2$	12.2	4.0	6.1	6.1	12.0	12.0	2.2	2.2	2.0×10^{11}	2.0×10^{11}	----

Table 7
COMPRESSIVE STRENGTH OF MATERIALS UNDER HYDROSTATIC PRESSURE (AFTER BRIDGEMAN)[52]

MATERIAL	HYDROSTATIC PRESSURE (psi)	APPARENT COMPRESSIVE STRENGTH (psi)
DIAMOND	330,000	1,830,000
QUARTZ	360,000	570,000
	230,000	470,000
	15	340,000
TOURMALINE	360,000	1,260,000
SYNTHETIC SAPPHIRE	360,000	1,000,000
SPINEL	360,000	580,000
TETON STEEL	360,000	680,000
.97 TaC-.02 VaC-.01 Mo_2C	325,000	510,000
CARBOLOY-999		2,100,000 (SHORT TERM)
PYREX	400,000	670,000
	15	25,000

Table 8

INTRINSIC STRENGTH BASED UPON SHOCK WAVE DATA (BASED UPON McQUEEN AND MARSH [54])

MATERIAL	C CRITICAL PRESSURE ($P_H = \sigma_t$) AT dP/dV = 0		SHEAR STRESS $\sigma_{s\ max}$	DYNAMIC SHEAR MODULUS G	$\frac{\sigma_{s\ max}}{G}$
Ag	-174 kbar	2.52×10^6 psi	1.26×10^6 psi		
Au	292 "	4.23 " "	2.12 " "		
Be	273 "	3.96 " "	1.98 " "	8.9	1/4.5
Cd	75 "	1.09 " "	0.55 " "		
Co	374 "	5.43 " "	2.72 " "		
Cr	330 "	4.79 " "	2.40 " "		
Cu	233 "	3.38 " "	1.69 " "	6.7	1/4
Hg	32 "	0.46 " "	0.23 " "		
Mg	70 "	1.01 " "	0.51 " "		
Mo	548 "	7.95 " "	3.98 " "		
Ni	331 "	4.80 " "	2.40 " "	11.6	1/4.8
Pb	77 "	1.12 " "	0.56 " "	0.78	1/1.4
Sn	86 "	1.25 " "	0.63 " "		
Ti	237 "	3.44 " "	1.72 " "		
T	68 "	0.99 " "	0.50 " "		
V	329 "	4.77 " "	2.39 " "		
W	606 "	8.80 " "	4.40 " "	19.4	1/4.4
Zn	107 "	1.55 " "	0.78 " "		